Università
Ca'Foscari
Venezia

Scuola Dottorale di Ateneo
Graduate School

Dottorato di ricerca
in Scienze Ambientali
Ciclo XXVI
Anno di discussione 2013

Advanced physico-chemical characterization of engineered nanomaterials in nanotoxicology

SETTORE SCIENTIFICO DISCIPLINARE DI AFFERENZA: CHIM/12
Tesi di Dottorato di Andrea Brunelli, matricola 955869

Coordinatore del Dottorato	**Tutore del Dottorando**
Prof. Gabriele Capodaglio	**Prof. Antonio Marcomini**

Abstract

The extensive use of engineered nanomaterials (ENM) in both industrial and consumer products is triggering a growing attention on the potential risk of ENM posed to human health and the environment. Despite the intensive toxicological investigations, both *in vitro* and *in vivo*, only few of them have embedded a solid characterization approach, including the study of ENM before, during and after toxicological testing.

Within EU-FP7 (ENPRA) and national (Toxicological and environmental behaviour of nano-sized titanium dioxide) projects activities, a comprehensive characterization of both inorganic (n-TiO_2, n-ZnO, n-Ag) and organic (multiwalled carbon nanotubes, MWCNT) ENM was carried out, updating and adding primary characterization data, investigating particle size, shape, crystallite size, crystalline phases, specific surface area, pore volume as well as inorganic impurities of concern. Electron microscopy, X-ray diffraction, BET method and Inductively coupled plasma-mass spectrometry or optical spectroscopy were the employed techniques. With regard to the secondary characterization of ENM, the study was divided in: (a) assessing the engineered nanoparticles (ENP) behavior in biological (0.256 mg ENP/ml) as well as in real and synthetic waters (environmentally realistic concentrations: 0.01, 0.1, 1 and 10 mg n-TiO_2 P25/l) over different time interval (24 h in biological media instead of 50 h in water media) to mimic duration of toxicological tests, by means of Dynamic Light Scattering (DLS), analytical centrifugation and nephelometry; (b) evaluating the ENM biodistribution in a secondary target organ (i.e. mice brain) after intratracheally instillation of ENM (0, 1, 4, 8, 16, 32, 64 and 128 ug ENM/animal tested), achieved by a microwave-assisted digestion method, followed by ICP-MS analysis, after selecting inorganic elements (i.e. Ti, Zn, Ag, Al and Co) as tracers of ENM presence in biological tissues. To investigate the ENP behavior in biological media and ENM biodistribution in mice, both dispersion protocols of the selected ENP and analytical protocols for ENM detection after toxicological testing were provided.

The study of ENP stability in biological media highlighted that the fetal bovine serum (FBS) is the main parameter affected the ENP behavior. Among biological media tested, the largest size distributions, immediately after sample preparation, were

recorded for n-TiO_2 NRCWE-003 dispersions. n-ZnO NM-111 dispersions were the most stable (12% average demixing, simulating 24 h of real sedimentation), except for Ag NM-300, originally received as dispersion (<1% average demixing). As expected, the ENP sedimentation rates investigated in the biological medium without any stabilizer (i.e. RPMI), were the highest for the whole set of ENP tested. In general, the highest sedimentation rates were recorded for n-TiO2 NM-101 and n-Ag 47MN-03 dispersions (51% average demixing, simulating 24 h of real sedimentation).

The study of the n-TiO_2 P25 stability in waters showed that agglomeration and sedimentation of n-TiO_2 were mainly affected by the initial concentration. Sedimentation data fitted satisfactorily (R^2 average: 0.90; $0.74<R^2>0.98$) with a first-order kinetic equation. The settling rate constant, k, increased by approx. one order of magnitude by moving from the lowest to the highest concentration, resulting very similar especially for all dispersions at 1 ($k = 8 \bullet 10^{-6}$ s^{-1}) and 10 mg/l ($k = 2 \bullet 10^{-5}$ s^{-1}) n-TiO_2, regardless the ionic strength and composition of dispersions.

The results from ENM biodistribution underlined that the chemical composition and the particle size were the main parameters that influenced the ENM partitioning into organs. Ti from n-TiO_2 samples with the smallest particle size distribution tested (80-400 nm and 4-100 nm) and Al from MWCNT samples were the only inorganic tracers detected in mice brain.

The whole characterization approach and the implication of these results are discussed.

List of Papers

Brunelli A, Pojana G, Callegaro S. Marcomini A. Agglomeration and sedimentation of titanium dioxide nanoparticles (n-TiO_2) in synthetic and real waters. J Nanopart Res 2013,15:1684.

Gaiser BK, Hirn S, Kermanizadeh A, Kanase N, Fytianos K, Wenk A, Haberl N, **Brunelli A**, Kreyling WG, Stone V. Effects of silver nanoparticles on the liver and hepatocytes in vitro, Toxicol Sci 2013, 131:537–547.

Hougaard KS, Jackson P, Kyjovska ZO, Birkedal RK, De TemmermanP-J RH, **Brunelli A**, Verleysen E, Mette Madsen A, Saber AT, Pojana G, Mast J, Marcomini A, Jensen KA, Wallin H, Szarek J, Mortensen A, Vogel U. Effects of exposure to carbon nanotubes on female fertility and fetal development. A study in mice. Repr Toxicol 2013, http://dx.doi.org/10.1016/j.reprotox.2013.05.006.

Squizzato S, Masiol M, **Brunelli A**, Pistollato S, Tarabotti E, Rampazzo G, Pavoni B. Factors determining the formation of secondary inorganic aerosol: a case study in the Po Valley (Italy), Atmos Chem Phys 2013, 13:1927–1939.

Zuin S, Scanferla P, **Brunelli A**, Marcomini A, Wong JE, Wennekes W, Genné I. Layer-by-layer deposition of titanium dioxide nanoparticles on polymeric membranes: a Life Cycle Assessment study. Ind Eng Chem Res 2013, dx.doi.org/10.1021/ie302979d.

List of abbreviations

AFM	Atomic Force Microscopy
BET	Brunauer-Emmett-Teller
CNT	Carbon Nanotubes
DLS	Dynamic Light Scattering
EDS	Energy Dispersive Spectroscopy
EELS	Electron Energy Loss Spectroscopy
ENM	Engineered Nanomaterials
ENP	Engineered Nanoparticles
ES-MS	Electron Spray Mass Spectrometry
FFF	Field Flow Fractionation
FTIR	Fourier Transform Infrared
HDC	Hydrodynamic Chromatography
ICP-MS	Inductively Coupled Plasma Mass Spectrometry
ICP-OES	Inductively Coupled Plasma Emission Spectroscopy
IF	Infrared
LCA	Life Cycle Assessment
LIBD	Laser-induced Breakdown Detection
LOD	Limit of Detection
MWCNT	Multi Walled Carbon Nanotubes
NM	Nanomaterials
NT	Nanotechnology
RA	Risk Assessment
REACH	Registration Evaluation Authorization and Restriction of Chemicals
SAED	Selected Area Electron Diffraction
SEC	Size-exclusion Chromatography
SEM	Scanning Electron Microscopy
SLS	Size-exclusion chromatography
SWCNT	Single Walled Carbon Nanotubes
TEM	Transmission Electron Microscopy
XRD	X-ray Diffraction

Acknowledgements

First, I would like to thank my main supervisor Professor Antonio Marcomini, to fund the PhD and to give me the opportunity to get in touch and collaborate with talented scientist from different research groups. I also want to give the same thanks to Professor Giulio Pojana, which was the reference person in the laboratory, giving me valuable advicea dn support.

I have also been lucky enough to work with Ing. Dagmar Bilanicova during the first year, teaching me closely the nano-world, always smiling. During the PhD I have also known Susanna, which has become a very good friend, so thank you for all the time spent together during this experience.

A special thank to every person working in Santa Marta, helping me over the years.

Obviously, I would like to thank my parents, because of their love, suggestions and support.

Finally, Elena, my beloved girlfriend.

Table of contents

Index of Figures and Tables

Chapter 1

Chapter 2

Chapter 3

Chapter 4

Chapter 5

Annex 1

Chapter 1

1. Introduction

1.1 Background and objectives

One of the research areas undergoing an exponential growth during the second half of the XX century, and predicted to be one of the key driver for economic development in the XXI century, is Nanotechnology (NT). The latter can be defined as a broad and interdisciplinary area of reserch and development. According to the definition provided by the Royal Society & The Royal Academy of Engineering (RA&RAE, 2004), NT includes the set of techniques and methods that can produce objects and devices in the nano-scale size range (10^{-9} - 10^{-7} m). NT encompasses the set of nanomaterials (NM) comprising nanoparticles (NP), nanofibers, thin films, nanoporous materials and nanocomposites. The study and development of these new materials are based on phenomena and manipulation of materials at atomic, molecular and macromolecular scale (EU, 2005-243).

It is believed that the American physicist Richard Feynman's 1959 talk, entitled *"There's Plenty of Room at the Bottom"* (Feynman, 1959), inspired the conceptual foundations of NT. However, only during the early '80s NT were actually developed with the advent of a new type of microscope (atomic force), which allowed the observation of both units atom and molecule (Brar et al., 2010).

Because of their nanosize dimensions (Figure 1.1), NT exhibit novel physical and chemical properties (e.g. surface effects and quantum mechanical effects) or enhance those that already have (e.g greater biological reactivity), due to their large surface-to-volume ratio, leading to novel applications compared with the bulk systems (Dowling, 2004; Wiesner et al., 2009).

To date, many nano-based consumer products have found a wide range of applications, such as electron devices, medicine, cosmetics, food industry, energy production and conservation as well as environmental remediation. Despite benefits,

these products have raised concerns about potential health risks and environmental impacts. As a matter of fact, recent literature has highlighted that structural properties of NM, i.e size, shape, surface area and charge, rate of aggregation/agglomeration, as well as the type of the functionalization of the molecules or coatings on their surfaces, are expected to affect the toxicity to humans and the environment (Krug and Wick, 2011; Murdock et al., 2008; Mwilu et al., 2013; Nishanth et al., 2011; Petosa et al., 2012). In order to better relate physico-chemical properties of NM to their biological interactions, effects and outcomes from the toxicity assays, it is therefore essential to develop a comprehensive approach, including also the Life Cycle Assessment (LCA) methodology, applied to NM during their whole life cycle (Auffan et al., 2012; Bauer et al., 2008; Keller et al., 2013; Som et al., 2010; Wallin et al., 2012; Zuin et al., 2013).

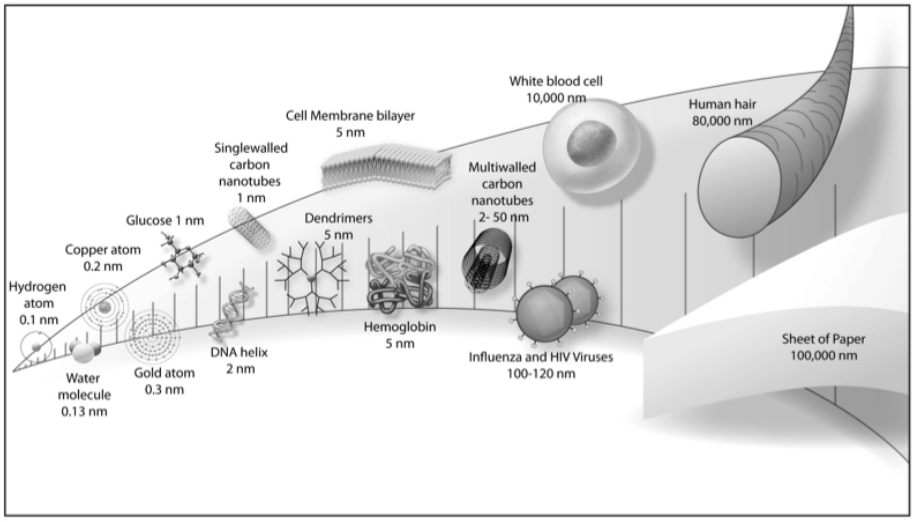

Figure 1.1 – Typical size diameter of single (1 nm) and multiwalled (2-50 nm) carbon nanotubes (CNT) compared to other chemical and biological materials (Yokel and MacPhail, 2011).

At international level, in order to fulfill these issues, several countries, research institutes and regulatory bodies (e.g. *US Environmental Protection Agency* (EPA), *Organization for Economic Co-operation Development* (OECD), *Scientific Committee on Emerging and Newly Identified Health Risks* (SCENIHR), *European Commission Joint Research Centre* (JRC), *British Health and Safety Executive* (HSE)), recently focused their attention on potential impacts of NM for humans and the environment. Narrowing the field at European level, research and innovation efforts have focused to the Seventh Framework Programme (FP7), running from 2007 to 2013, building a

bridge to the next EU Framework Programme Horizon 2020. FP7 has allocated a total budget of EUR 55 billion for the calls of proposals covering the field of NT and Nanosciences (NS).

From a regulatory point of view, the European Community Regulation on chemicals and their safe use (*Registration, Evaluation, Authorization and Restriction of Chemicals* (REACH)) regulates also NM, being included in the definition of a *chemical substance* (i.e. in whatevere size, shape or physical state) within REACH. The general obligations in REACH therefore apply to NM as for any other chemical, even if there are no provisions referring explicitly to NM. Unfortunately, because of their physico-chemical properties, that drive their behaviour into several systems, NM can not be considered solely a chemical, thus emphasizing that REACH can not be applied under its original form, reveling the absence of specific provisions and many uncertainties in the interpretation of legal concepts and obligations within REACH. However, according to the Second Regulatory Review on Nanomaterials COM (2012) 572 accompanied by Staff Working Document SWD(2012) 288 (COM(2012)527, 2012), "*the Commission remains convinced that REACH sets the best possible framework for the risk management of NM when they occur as substances or mixtures but more specific requirements for NM within the framework have proven necessary. The Commission envisages modifications in some of the REACH Annexes and encourages ECHA (European Chemicals Agency) to further develop guidance for registrations after 2013"*. Falling within REACH, the information requirements about NM, to be delivered to EU Commission, are related to the total tonnage/year production on the global market, as any other chemical substance. Registering a NM implies an obligation to specify physico-chemical properties, uses, effects and exposure related information, classification, labelling and safety assessment. Furtermore, in addition to the Horizontal legislation, covered by REACH, as well as by general product safety and product liability, workers' protection and environmental legislation, the more nano-specific Vertical legislation on products, has to be taken into account. Among all, the (Regulation(EC)1223/2009) on cosmetic products included notification (from January 2013) and labelling (from 11 July 2013) obligation of nanoproducts to EU Commission; the (Regulation(EC)1169/2011) on the provisions of food information to consumers highlighted labelling obligation of nano-ingredients (from December 2014); according to the Biocidal Products Regulation (Regulation(EC)528/2012), the approval of the

active substance in the biocidal product does not cover the NM form of the active substance except where explicitly mentioned. A separate dossier with all data requirements must usually be prepared for nanoforms of active substances. Moreover, a dedicated Risk Assessment (RA) is needed when the NM form of the active and non-active substances are used in a biocidal product. The label of the biocidal product must indicate the name of each NM followed by the word "nano" in brackets. Products containing NM are excluded from the simplified authorisation procedure. Finally, Member States must report on the implementation of the Biocidal Products Regulation every five years. The reporting must include information on the use of NM in biocidal products and the potential risks identified (http://echa.europa.eu/web/guest/regulations/biocidal-products-regulation/nanomaterials, 2012).

In this context becomes extremely important to carry out an extensive characterization of NM, investigating both ordinary physico-chemical features, so called “basic” characterization, to address both “primary” (i.e. applied to pristine NM, i.e. as provided, before any testing) and “secondary” (i.e. applied to NM under test conditions) characterization.

The main objective of this PhD thesis, which is part of both the EU-FP7 project “Risk Assessment of Engineered Nanoparticles” (ENPRA) and the national PRIN project “Toxicological and environmental behavior of nano-sized titanium dioxide”, was to investigate both primary and secondary characterization of engineered NM (i.e. manufactured nanomaterials, called ENM) and to develop standardize protocols for engineered NP (ENP) dispersion and ENM detection in biological samples.

The activity was performed through different steps as follows:

- a literature review on the state of the art of the physico-chemical characterization of the most common ENM from a toxicological point of view;
- an extensive characterization of several ENM, including the integration of primary characterization data performed by project partners, the investigation of ENM behaviour into liquids, as well as the evaluation of ENM biodistribution after toxicological testing, in order to support hazard and risk assessment of ENM, as well as LCA of nano-based products;

- the development of dispersion protocols of ENP in biological media employed for cell growth, as well as analytical protocols for the ENM detection and quantification in a secondary target organ after toxicological testing, due to the lack of appropriate standardized methodologies already highlighted in the literature.

1.2 Structure of the thesis

The definition of ENM and some terms usually employed into this field of research, as well as their classification, their physico-chemical properties and the potential human and environmental impacts relating to ENM are discussed in Chapter 2.

Chapter 3 deals with the state of the art about the characterization of the most widespread ENM, listing different techniques employed according to the level of characterization considered and the aim of research. The difference between imaging and analytical techniques are presented, pointed out those employed within project activites.

In chapter 4, the experimental desing about characterization of the selected ENM is fully described, highlighting the materials and methods employed to carry out both primary and secondary characterization.

The results from the characterization approach is presented in chapter 5, separating the physico-chemical properties measured by data collected regarding the behavior of ENM in different environmental media, as well as the presence of ENM in biological tissues studied. Moreover, both dispersion protocols for ENP in biological media and analytical protocols for study the ENM biodistribution are provided.

Finally, Chapter 6 is dedicated to the discussion of the obtained results while the conclusions of the advanced characterization of ENM performed and how this approach could support nanotoxicology are reported in chapter 7.

Chapter 2

2. Engineered Nanomaterials

2.1. Definition

Despite the intensive manufactured, commercialised and used for nearly a decade, a global definition of NM, but legally not binding, has been agreed only recently, on October 18, 2011. According to the "*Reccomendation on the definition of a nanomaterial" (EU, 2011, October 18)*, a "Nanomaterial" means:

"A natural, incidental or manufactured material containing particles, in an unbound state or as an aggregate or as an agglomerate and where, for 50 % or more of the particles in the number size distribution, one or more external dimensions is in the size range 1 nm - 100 nm.
In specific cases and where warranted by concerns for the environment, health, safety or competitiveness the number size distribution threshold of 50 % may be replaced by a threshold between 1 and 50 %.
By derogation from the above, fullerenes, graphene flakes and single wall carbon nanotubes with one or more external dimensions below 1 nm should be considered as nanomaterials".

Furthermore, as reported by this Reccomendation, "particle" means a minute piece of matter with defined physical boundaries. As NM, also the definition of NP has been developed over years, meaning nowadays *particles with all the three external dimensions in the range 1 nm – 100 nm* (BSI, 2007; SCENIHR, 2007).

2.2 Classifications

In general, a categorisation of NM has been already suggested by Hansen (Hansen et al., 2007), as a function of the location of the nanoscale structure in the system, as follows: I) materials that are nanostructured in the bulk; II) materials that own nanostructure on the surface; III) materials that contain nanostructured particles. Among these, category III could also be further divided into four subcategories, depending on the environment around the NP: a) subcategory IIIa has NP bound to the surface of another solid structure; b) subcategory IIIb includes NP suspended in a liquid; c) subcategory IIIc consists of NP suspended in solids; d) subcategory IIId refers to airborn NP.

NM can be classified either into unintentionally produced, as Ultrafine particles (UFP) existing in the particulate matter from both natural or anthropogenic source, or artificially manufactured for several applications such as paints and coatings, cosmetics and personal care products, textiles, sports equipment, food ingredients and packaging, consumer electronics, medicine and healthcare products (Biswas and Wu, 2005; Lövestam et al., 2010) (Table 2.1).

NM can be further distinguished based on their physico-chemical properties, among which the most relevant in a toxicological perspective are size, shape, specific surface area, chemical composition, lattice structure, surface chemistry, surface charge, aggregation state, surface reactivity and surface coating.

Table 2.1 – Different classifications of NM depending on the sorce and the physico-chemical properties (adapted from (Borm et al., 2006; Nowack and Bucheli, 2007; Stone et al., 2010).

Discriminating factor	Alternatives	
source	(a) Unintentionally produced (UFP*)	(I) natural (e.g. volcanoes; sea spray; erosion; biomass burning)
		(II) anthropogenic (e.g. traffic; industry)
	(b) Intentional production	engineered NM for several applications
physico-chemical properties	size distribution	
	shape	spheres; needles; tubes
	specific surface area	
	chemical composition	(a) inorganic metal or metal oxides (e.g. Ag, TiO_2, SiO_2, Fe_3O_4)
		(b) organic (e.g. CNT; fullerenes)
	lattice structure	
	surface charge	
	aggregation state	individual; aggregates; agglomerates
	surface reactivity	
	Functionalization/surface coating	(a) chemical bonds; weak interactions (e.g. micelle)
		(b) adsorption by several forces (e.g. protein corona)
		(a) organic compounds (e.g. tri-ethoxy caprylsylane 130; carboxylic acid; proteins; amino acids
		(b) inorganic (e.g. Ag or Au rings)

* UFP: Ultrafine particles, whose diameters are < 0.1 μm, also called $PM_{0.1}$.

Intentionally produced NM deliberately designed with very specific properties (i.e. size, shape, surface charge, surface area, functionalizations/coatings) as a function of the effective application, that from here on will be refereed to as ENM, are the only subject of the current research. ENM include completely inorganic NM, such as metals (e.g. iron, silver, gold, zinc, titanium), and metal oxides (titanium dioxide,

silica, zinc oxide, cerium dioxide, etc.), interely organic (CNT, nanopolymers, fullerenes, etc.), or “hybrid”, usually chalcogenides (selenides or sulfides) of metals like cadmium or zinc (i.e. “core-shell” structure as the quantum dots, QD). Moreover, ENM are commercialy available as dry powders or dispersed in liquids, usually with organic stabilizers (Sahana et al., 2008). They can be found as aggregates and/or individual materials, showing several sizes and morphologies (e.g. spheres, fibres, needles, flakes). ENM can be embedded in commercial products, such as nano titanium dioxide (n-TiO_2) and nano zinc oxide (n-ZnO) used in sunscreens for UVB (290-320 nm) and UVA (320-400 nm) attenuation, respectively (Monteiro-Riviere et al., 2011; Newman et al., 2009), or added to other cosmetics and personal care products (Lorenz et al., 2011; Weir et al., 2012), bonded or encapsulated within a matrix, as surface-modified nano silver (n-Ag) added to a polystyrene matrix for its antimicrobial activity (Betancourt-Galindo et al., 2012), or as nano zero valent iron (nZVI) employed in soil and groundwater remediation (Grieger et al., 2010). In general ENM, especially ENP powders, exhibit an high tendency to agglomerate during the dispersion process due to van der Waals forces (Werth et al., 2003). Especially in the biomedical field, the agglomeration process of ENM is deliberately avoid, e.g. by stabilizing (i.e. reaching a balance between attractive and repulsive forces) them with proper coating layers of chemically and thermally stable materials, both inorganic and organic (Dutta and Hofmann, 2004; Iijima et al., 2005), so as to provide a better NM dispersibility and stability over time. Table 2.2 summarizes the most common ENM employed in many research fields because of their unique physico-chemical properties, showing also the production/utilization quantities of these materials both in the world and in Europe. According to a survey (46 feedbacks received) sent to industrial companies manufacturing and working with ENM and published by (Piccinno et al., 2012), inorganic ENP, in particular metal oxides such n-TiO_2, n-CeO_2, n-FeO_x, n-AlO_x, n-ZnO and the most widespread ENM, i.e. CNT, were in the first positions in terms of the estimation of global production/utilization. n-TiO_2 held the highest values up to 10000 t/year of worldwide production, while the others mentioned ranged between 100 and 1000 t/year. n-SiO_2 covered a very wide range of values, from less then 10 to more than 100000 t/year. This high variance of the distribution underlines, as suggested by the authors, the problems related to the definition of this material and which type of silica (e.g. pyrogenic silica) could be considered as ENP. Fullerenes, n-Ag and

quantum dots (QD) were produced in Europe in relative small quantities (less than 10 t/year), excepting the global production of n-Ag, which reached approx. 1000 t/year.

Table 2.2 - The most widespread ENM because of their applications and benefits and the estimate of their production/utilization both on the global and european market, according to a survey by Piccinno et al., 2012.

NM	Applications	Benefits (both alone and functionalized)	References (examples)	Worldwide (t/year)*	Europe (t/year)*
n-Ag	paints, toothpaste, clothing textiles, plastics, water treatment, medical devices, food packaging, household cleaners, bed linen; antimicrobial coatings	anti-microbial activity; sensing and imaging applications	(Benn and Westerhoff, 2008; Bhattacharya and Mukherjee, 2008; Blaser et al., 2008; Gottschalk et al., 2010; Khaydarov et al., 2011); (Farkas et al., 2011; Gottschalk and Nowack, 2011; Piccinno et al., 2012); www.nanotechproject.org/inventories/silver/	55 (5.5-550)	5.5 (0.5-55)
n-TiO_2	Cosmetics (incl. sunscreens), clothing, cleaning and self-cleaning products, electronic devices, air filtration, food; water treatment; air purification	transparent to visible light; highly UV absorbent; iridescence; high photoactivity; self-cleaning	(Auffan et al., 2010; Chen and Mao, 2007; Guan et al., 2012; Hua et al., 2012; Kaegi et al., 2008; Labille et al., 2010; Lorenz et al., 2011; Newman et al., 2009; Pelaez et al., 2012; Piccinno et al., 2012; Robichaud et al., 2009; USEPA, 2010)	3000 (550-5500)	550 (55-3000)
n-ZnO	Cosmetics; paints; optoelectronic and electronic devices; textiles; sunscreens; suspensions; food packaging; gas sensors; solar cells; biosensing; water treatment	transparent to visible light; UVA attenuation	(Becheri et al., 2008; Espitia et al., 2012; Gomez and Tigli, 2013; Gomez and Tigli, 2011; Hames et al., 2010; Hua et al., 2012; Jones et al., 2008; Piccinno et al., 2012)	550 (55-550)	55 (5.5-28000)
n-SiO_2	Paints; coatings; concrete; theranostic application; biomedicine and cancer treating; catalytical applications	hardener and strengthener material; dye adsorbent	(Barik et al., 2008; Musee, 2010; Napierska et al., 2010; Singh et al., 2013; Tang et al., 2012; Wu et al., 2012)	5500 (55-55000)	5500 (55-55000)
n-CeO_x	fuel additives; coatings; paints; environmental remediation; biomedicine	UV absorbent; antioxidant; polishing agent; great catalyst; antibacterial activity	(Chen et al., 2006(Gottschalk, 2011 #274; Hua et al., 2012; Piccinno et al., 2012; Recillas et al., 2011; Shah et al., 2012)	55 (5.5-550)	55 (0.55-2800)
n-Au	biomedicine; photothermal therapy; separation methods; gas sensors; coatings	great photostability; high scattering cross section; strong two-photon and multi-photon luminescence	(Cobley et al., 2011; Ghosh et al., 2008; Huang and El-Sayed, 2010; Krystek, 2012; Rosi and Mirkin, 2005; Sýkora et al., 2010; Tiwari et al., 2011; Yeh et al., 2012)	n.e.	n.e.
n-Fe_xO_x	cellular therapy; drug delivery; magnetic resonance imaging; water treatment	superparamagnetic phenomena; quantum tunneling of magnetization	(Amstad et al., 2011; Gupta and Gupta, 2005; Hua et al., 2012; Huber, 2005; Teja and Koh, 2009)	55 (5.5-5500)[a]	550 (30-5500)[a]
n-AlO_x	biomedicine; coatings; electronics; structural ceramics for reinforcements; wastewater treatment	adjuvants in human vaccines; scratch and wear resistance; catalyst; good thermal conductivity, resists strong acid and alkalai containing materials; easily shaped;	(Bertsch et al., 2004; Caitlin et al., 2012; Hua et al., 2012; Jodin et al., 2006; Maquieira et al., 2012; Pacheco et al., 2006)	550 (55-5500)	550 (0.55-500)
CNT	Composites, polymer additives; electronic devices; neurobiology; energy conversion and storage; environmental monitoring and water treatment; sporting goods	one hundred times the tensile strength of steel; high thermal conductivity; high electron transfer rate over the sidewall; strong chemical reactivity; strong adsorption properties	(Boczkowski and Lanone, 2012; Donaldson et al., 2006; Landi et al., 2009; Malarkey and Parpura, 2007; Piccinno et al., 2012; Saeed, 2010; Tan et al., 2012; Zhang et al., 2010)	300 (55-550)	550 (180-550)
Fullerenes	Medicine, drug delivery; photoacustic imaging; photothermal ablation therapy; electronics	Hydrophobicity; quickly agglomeration; intra electron transfer; generate ROS	(Ahmed et al., 2012; Bakry et al., 2007; Chawla et al., 2010; Chen et al., 2012; Krishna et al., 2010; Maeyoshi et al., 2012; Tagmatarchis and Shinohara, 2001)	0.6 (0.6-5-5)	0.6 (0.6-5.5)

n.e. = not estimated.

[a] Data only referred to n-FeO_x.

2.3 Nano and bulk materials

Particle size and shape are considered the main physico-chemical properties that lead to the largest difference between nano- and bulk materials of the same chemical composition, in terms of catalytic activity, melting point, optical characteristics, magnetic behavior, chemical reactivity etc. (Alivisatos, 1996; El-Sayed, 2004; Lee et al., 2009). As the crystal size decrease to the nanometre scale, the luminescence of n-Au changes from the classical yellow (bulk) to blue (crystal size: 30-500 nm), red (crystal size: 3-30 nm), orange (crystal size < 1nm) and colorless (crystal size: 1Å). Moreover, the melting point of a solid, i.e. the temperature at which it changes state from solid to liquid and depends on its crystal lattice, type of atoms packing and its coordination number, dramatically decreases from 1600°C for CdS bulk material to 400°C when the CdS crystal size reaches to approx. 3 nm.

In general two major size-related effects can be distinguished, which are responsible for the unique ENM properties and consequently behavior: firstly, an extremely high surface area-to-volume ratio than the bulk material, involving a relative strong increase in the percentage of surface atoms; secondly the quantum size effect (Roduner, 2006).

Considering one carbon microparticle with a diameter of 60 μm, it has a mass of 0.3 μg and a surface area of 0.01 mm^2. Taking into account the same material with the same mass but in NP form (diameter: 60 nm), the surface area rises to 11.3 mm^2 and consists of 1 billion NP. This underlines that the surface area is inversely proportional to the particle size: the surface area-to-volume ratio for a particle with a diameter of 60 nm is 1000 times larger than a particle with a diameter of 60 μm (Figure 2.1). As the ratio above increases, also the number of surface atoms rises with respect to the bulk material, dramatically enhancing the reactivity of NP since the lower coordination number of surface atoms than the inner atoms. This extra energy owned by NP may be described by the surface energy, γ, which is the energy per unit area involved in forming a new surface or the excess energy at the surface of a material compared to the bulk. The surface energy γ could be defined as (de Gennes et al., 2004):

$$\gamma = \left(\frac{\partial G}{\partial A} \right)_{p,T} \qquad \text{(Eq. 1)}$$

where A is the surface area and G is the Gibbs free energy as a function of temperature *T* and pressure *p*. Eq. 1 means that the surface energy *γ* is equal to the variation of the Gibbs free energy for an infinitesimal variation of the surface area A, with *p* and *T* constants. The unit measurement of surface energy is J/m^2 and it is always higher for free NP than the bulk material (e.g. 7.2 J/m^2 for n-Ag while 1-1.5 J/m^2 for Ag bulk material) (Schaefer, 2010). This suggests that specific surface area and, thus, the total surface energy become significant for nanometer size particles.

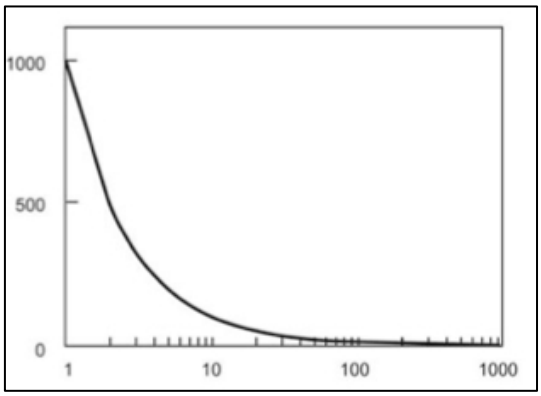

Figure 2.1 – Surface area normalized to mass, in the y-axis, vs particle diameter (nm), in the x-axis (Buzea et al., 2007).

The second size-related effect of ENM is the quantum size effect. This phenomenon, observed only for metals and semiconductors, can only occur due to the size of NP, which is comparable to the de Broglie wavelength (order of nanometers) of its charge carriers. As the particle size decrease up to the nanometer scale (nanocrystal), the physico-chemical properties of NP are different both from the metallic bulk and from the single molecule. The “semi-continuous” density of electronic states belonging to the conduction and valence band of the bulk metal decreases up to quantizied electronic levels, with discrete energy levels (Schmid, 1992): thus the electronic structure of a nanocrystal is intermediate between the discrete levels of molecules and the band structure of the bulk crystal (Figure 2.2), because the charge carriers are confined to a narrow region along all the three directions in space.

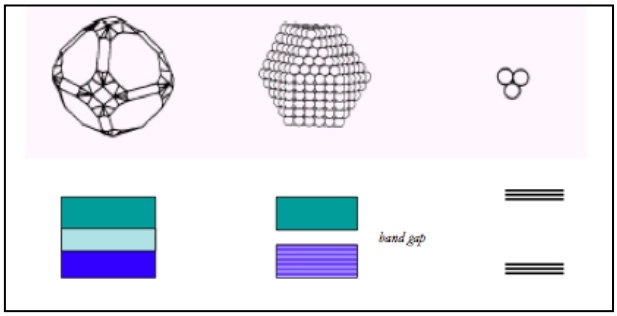

Figure 2.2 – Electronic energy levels of the metal (left), nanocrystal (middle) and a single molecule (Schmid, 1992).

At the nanometre scale, quantum effect are therefore more important in determining the properties and characteristics of the material. This finding has led to develop new materials, such as the quantum dots (QD), semiconductors crystals with diameters in the range of 10-50 nm. Figure 2.3 shows the most notorious size-related property belonging to QD, i.e. the variation of their photoluminiscence as a function of the size.

Figure 2.3 – Photoluminiscence of CdSe QD dispersions, varying the size from 2 to 8 nm.

As a result given by unique characteristics of ENM, the next paragraph deals with the main physico-chemical properties of ENM that might affect the potential toxicological effects observed.

2.4 Nanotoxicology

The huge increase of nano-based products on the global market because of their unique physico-chemical properties mentioned above, involves the unintentional release of ENM in the environment, detected and quantified only by few studies (Farkas et al., 2011; Kaegi et al., 2010; Kaegi et al., 2008; Kiser et al., 2009). When these materials reach the ecosystem, they may come in contact with biological organisms through the predominat exposure routes, i.e. inhalation, ingestion and dermal pathway, and thereby entering the biological fluids to reach tissues, cells, and organelles (Geiser and Kreyling, 2010; Oberdorster et al., 2005), since the actual size of ENM is similar (i.e. order of nanometers, see Figure 1.1) to that of many biological molecules and structures (e.g. proteins and viruses, respectively). Major entry routes (by inhalation, dermal contact, ingestion) and potential targets (lungs, gut, liver, spleen, heart and brain) of the most widespread ENM have been investigated by numerous studies over the past two decades (Dailey et al., 2006; Heinrich et al., 1995; Kelly, 2008; Kreilgaard, 2002; Oberdörster et al., 2007) but further investigations are needed, especially to investigate the ENM amount in secondary organs and tissues (i.e. indirectly involved). The ENM-organism interaction can result not only in biologically desirable effects, as summarized in Table 2.2, but may also lead to concerns about possible adverse health effects to exposured organisms (Muller et al., 2008; Shvedova et al., 2010; Xu et al., 2010). Indeed a growing literature is exploring the potential risks and toxicity of their use (Clement et al., 2013; Gangwai et al., 2011; Kermanizadeh et al., 2013; Oberdoerster, 2012; Panas et al., 2013), but much more effort is needed due to contraditory toxicological results obtained (Laurent et al., 2012).

Since inhalation is one of the most important pathway of human exposure to external bodies, a lot of data referring to the toxicity of ENM derived from prior experience, such as inhaled ultrafine particles (Donaldson et al., 2004; Kreyling et al., 2006; Oberdorster et al., 2000; Oberdorster et al., 2005) and asbestos (Kane and Hurt, 2008). ENM were found to deposit throughout the entire respiratory tract, going from nose up to the lungs, which are the primary entry portal for inhaled particles due to their large surface area (i.e. between 75−140 m^2). The deposition rate of inhaled particles was observed to be size-dependent (Figure 2.4) (Buzea et al., 2007). After entering the body, ENM may reach all other target body systems, where they may cause additional adverse effects.

The way of ENM-organism interaction is governed by the specific physico-chemical properties, among which the most relevant that can lead to toxicological effects include size, shape, surface charge, chemical composition and impurites, coatings and media in which ENM could be dispersed (Sharifi et al., 2012). Both *in vitro* and *in vivo* toxicity of the most common ENM have been recently reviewed (De Stefano et al., 2012; Elsaesser and Howard, 2012; Nel et al., 2006; Oberdörster et al., 2007; Sharifi et al., 2012), highlighting several mechanism of ENM toxicity, such as the presence of oxidative stress, which can cause an inflammatory reaction, the genotoxicity, the protein corona effect (i.e. a bond between proteins of a biological fluid and the surface of an ENM) and the excessive production of reactive oxygen species (ROS) (Boczkowski and Lanone, 2012; Moller et al., 2010; Unfried et al., 2007). Despite these investigations a key challenge to be addressed in the near future is finding correlations between physico-chemical properties and the biological and toxicological effects of cells and tissues exposure to ENM. Within the OECD publication n° 27 (OECD, 2010), the physico-chemical properties and material characterization, when testing specific manufactured ENM for human health and environmental safety, were already listed. The authors suggested to take into account agglomeration/aggregation, water solubility/dispersability, crystalline phase, dustiness, crystallite size, representative TEM pictures, particle size distribution (both as dry and in relevant media), specific surface area, zeta potential (surface charge), surface chemistry (where appropriate), photocatalytic activity, pour density, porosity, octanol-water partition coeffcient (where relevant), redox potential, radical formation potential and other relevant physico-chemical properties and material characterization information (where available).

The existing literature concerning the ENM physico-chemical properties that may drive toxicological effects is still scarse and contradictory due to the heterogeneity of ENM marketed to be tested and experimental desings engaged, even if some results have been achieved and summarized here below.

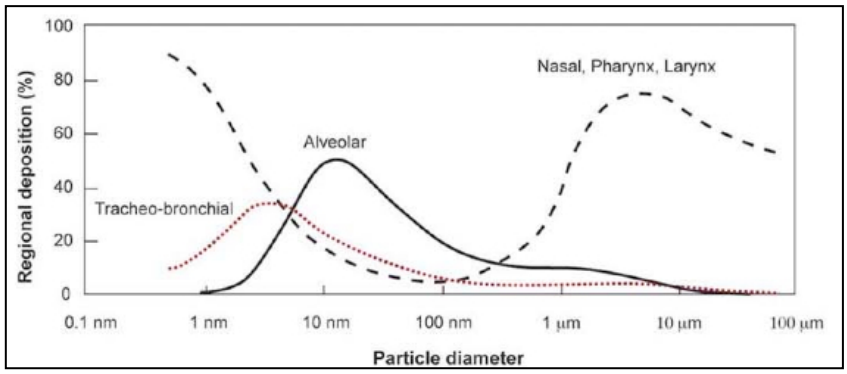

Figure 2.4 – The deposition of inhaled particles as a function of their diameter (nm) (from Buzea et al., 2007).

Particle size and thus surface area have become crucial parameters in a toxicological perspective since the interactions between ENM and biological organisms typically occur at the ENM surface (Sharifi et al., 2012). As the particle size decreases, its surface to volume ratio grows, displaying an higher amount of atoms or molecules on the surface rather than the inner material. The dependence of biological response on the particle size can be observed, for example, considering Chithrani *et al.* and Osaki *et al.* studies, who have been shown that the maximum ENP cellular uptake occurs at an optimal size around 50 nm, for both n-CdSe and n-Au (Chithrani et al., 2006; Osaki et al., 2004), similar to some viruses and lipid-carrying proteins sizes. Conversely Wang *et al.* did not found any size-dependent toxicity belongs to n-Au, probably due to the aggregation of n-Au outside the cell (Wang et al., 2008). Furthermore, the experiments carried out by Rancan *et al.* focused on the penetration of n-SiO_2 in the human skin, observing that the penetration is size-dependent since human skin can efficiently block the penetration of silica particles of above 75 nm in size (Rancan et al., 2012). Finally, as revealed by a lot of studies, the increase of the surface area reactivity and the smaller size of ENM in comparison with the bulk material has led to potential mechanisms of toxicity (Holgate, 2010; Karlsson et al., 2009; Nabeshi et al., 2010; Poland et al., 2008; Powers et al., 2007; Sohaebuddin et al., 2010).

Particle shape is another key factor that could induce the ENM toxicity. ENM can own several shapes, such as fibers, spheres, tubes, rings and planes. One of the most organic nanomaterials employed to date, i.e. CNT, since they possess long and thin geometry may have the potential to cause adverse effects similar to those of asbestos,

when inhaled, such as the development of mesothelioma (Jaurand et al., 2009), even if they differ completely to the chemical composition. Both single-walled CNT (i.e. SWCNT) and multi-walled CNT (i.e. MWCNT) have enhanced the likelihood of some negative effects on tested organisms, such as platelet aggregation and vascular thrombosis in rat carotid arteries (Radomski et al., 2005) and the block of potassium ion channels compared to spherical carbon fullerenes (Park et al., 2003). Recent studies have shown other physiological responses induced by the particle geometry of CNT, QD, n-TiO_2, n-ZnO and n-Au, including chronic inflammation, mutagenic events and mesothelioma development (Aaron et al., 2011; Hsiao and Huang, 2011; Peng et al., 2011; Sun et al., 2011).

Surface charge is a further parameter to be considered in the ENM toxicity field as it influences the interactions between ENM and the surrounded medium or organism that become in contact with. The positive surface charge of n-SiO_2 has been shown that increased both the paracellular permeability (Lin et al., 2006) and the phagocytosis of liposomes by hepatic Kupffer cells (Schiestel et al., 2004), which Nishimori *et al.* shown to be a positive effect that decrease ENM toxicity (Nishimori et al., 2009). Therefore it is thought that the ENP with a positive surface charge decrease hepatic toxicity (Isoda et al., 2011). On the other hand, considering another type of ENP, QD surface charge can affect cytotoxicity (Yacobi et al., 2007), emphasizing that positively charged QD were more cytotoxic compared to negative charged QD (Nagy et al., 2012).

Chemical composition also plays a significant role in toxicity, mainly when ENM come closely in contact with biological organisms. Harper *et al.* has demonstrated that, after a 5-day continuous waterborne exposure of embryonic zebrafish to eleven commercial ENP dispersions with similar particle size, the outcomes in terms of significant morbidity and mortality were considerably different (Harper et al., 2008). Moreover toxicity data on zebrafish, daphinds and algal species, collected by Griffitt *et al.*, underlined that, while n-TiO_2 did not shown any negative effect, n-Ag, n-Cu and their soluble forms caused toxicity in all organisms tested, even if the particle sizes were similar. They also observed that ENP tested were species-specific since the filter-feeding invertebrates were more affected to ENP exposure compared to zebrafish (Griffitt et al., 2008). At the same time Chen *et al.* presented acute toxicity data of n-TiO_2 in mice after intraperitoneal injection with different doses (from 324 to 2592 ug/g, increasing the concentration of a 0.5 factor) and over a wide time range, founding n-TiO_2 in spleen, kidney and liver tissues (Chen et al., 2009). Furthermore the chemical composition as a driver of toxicity was yet

investigated through Sohaebudden *et al.* (Sohaebuddin et al., 2010), finding different negative effects between ENM types, i.e. MWCNT, n-TiO_2 and n-SiO_2, and both cell viability and the kinetics of cell death. A paper recently published (Šiller et al., 2013) underlined that the toxicity tested after 24 and 48 h in sea urchin *Paracentrotus lividus* embryos/larvae given by n-Ag are higher than their equivalent Ag^+ ion dose, highlighting that the defects were already observed at approx. 0.3 mg/l n-Ag.

Finally it has to be understand if the negative effects observed become from the chemical composition of ENM or from some undeclared impurities embedded, i.e. particles and/or substances contained in the manufactured materials or resulting from subsequent treatments but not previously characterized and which can mask the intrinsic toxicity of tested ENM (Jacobsen et al., 2008; Jacobsen et al., 2007).

Recently numerous studies in the field of nanomedicine have stressed the importance regarding the utilization of a coating, both organic (Tri-ethoxy Caprylylsylane, alizarin red S, proteins, amino acids, surfactants) or inorganic (Ag-rings and Au-rings coatings n-FeO), on the surface of an ENM (Mahmoudi and Serpooshan, 2012; Samanta et al., 2008). The aim was to prevent or mitigate ENM adverse effects, stabilizing, avoiding agglomeration and preventing the dissolution and release of toxic ions (Sharifi et al., 2012). As a matter of fact the coating materials can enhance both the dispersibility and stability in commercial products (Kwok et al., 2012) and the biocompatibility and stability in biological media (Lin et al., 2011). In addition the functionalizations/coatings of ENM as imaging agents and targeting devices were used (Thurn et al., 2011). Since their growing use for the benefits listed above, also the toxicity induced by coating materials was investigated. Wang *et al.* have found that gold nanorods are highly cytotoxic to human skin keratinocytes due to the presence of cetyltrimethylammonium bromide (CTAB) as coating material compared with spherical n-Au of different sizes (5-12-20-30-50 nm) (Wang et al., 2008). The cytotoxicity effects againts mouse macrophage (RAW-264.7) and lung epitheial (C-10) cell lines induced by n-Ag was remarked to depend on various factors, among which on surface coating materials used in the n-Ag synthesis (Suresh et al., 2012). The most toxic ENP was poly(diallyldimethylammonium)-coated n-Ag, followed by biogenic-n-Ag and oleate-n-Ag while colloidal and uncoated n-Ag were the least toxic to both RAW-264.7 and C-10. Moreover, as underscored by Zhang *et al.* (Zhang et al., 2012), coating-dependent cytotoxicity was revealed with cetyltrimethylammonium-bromide (CTAB) encapsulated gold nanorods (GNR), which was more cytotoxic than GNR undergone

further polymer coating and citrate stabilized gold nanospheres. Despite of these results, surface coating was also observed to positively affect the *in vivo* toxicity. Indeed the surface modification of n-SiO_2 with amino group and carboxyl group, compared to the unmodified n-SiO_2, attenuated liver toxicity into mice, probably due to the decrease in the n-SiO_2 amount that storage in the liver (Isoda et al., 2011).

Surface roughness can also be a significant parameter in determining the outcome of the ENM-cell interaction, involving in non-specific binding forces that promote cellular uptake (Adeli et al., 2011; Doumari et al., 2011). Hemolytic activity of non-porous and porous-silica ENP of various sizes were tested by Lin *et al.* (Lin and Haynes, 2010), understanding that fewer silanol groups on the porous-silica ENP surface affected the cytotoxicity.

At the same time there are some evidences that the rapid formation of agglomerates of ENM in different media, strongly favored due to the high number density, which increased likelihood of collisions between particles, may enhance ENM cellular uptake, causing inflammation and oxidative stress after exposure (Limbach et al., 2005; Wick et al., 2007). The cell viability has also been shown that may be affected not only by ENM concentration but also by ENM agglomeration induced by fetal calf serum (FCS) content (Drescher et al., 2011). Moreover the cytotoxicity induced by two different colloidal amorphous n-SiO_2 (i.e. AS30 and SM30 Ludox®, owing two different sizes and stabilizing by ammonium and sodium counterions, respectively) on three human cell lines, i.e. A549 (lung adenocarcinoma), CCD-34Lu (normal lung fibroblasts) and HT-1080 (fibrosarcoma), was investigated under different media compositions and exposure times. The results demonstrated that changing these parameters caused different cytotoxicity, due to n-SiO_2 agglomeration induced by serum components, suggesting to carry out proper studies to compare toxicity data obtained with both short- and long-term assays (Fede et al., 2012). On the other hand Kobayashi *et al.* (Kobayashi et al., 2009) did not found a clear relationship in pulmonary inflammation among the rats instilled with n-TiO_2 of the same primary size but different particle agglomerations.

The overall results mentioned above point out that ENM both *in vitro* and *in vivo* toxicity depends mostly on the testing strategy and treatment conditions employed. In this scenario the new branch of toxicology, called nanotoxicology, already proposed for addressing the gaps in toxicological knowledge of ENM (Donaldson et al., 2004), is an extremely useful tool in order to understand the mechanisms of toxicity induced by ENM,

preventing the risks associated with the intensive use of nano-based products in everyday life. While the classical toxicology is generally based on the protocolised characterization of toxicants, with a well established set of methodologies available, employing a mass-based dose metric (Elsaesser and Howard, 2012), the nanotoxicology has less certainty on which to base, in terms of the dose metric, the protocol of bioassays not yet internationally harmonized and validated (De Stefano et al., 2012) and the many more variables and physico-chemical properties, which often differ from the bulk materials. The developed of this new branch of research focuses on the characterization data and toxicological investigations about the most common ENM in order to establish a relationship between physico-chemical properties and their toxic potential, also through supporting tools such as Quantitative Structure-Activity Relationship (QSAR) models, for determining potential risks of ENM following the routes of exposure. To assess this key correlation and ensure that results are reproducible and meaningful, an accurate characterization of ENM at different stages, such as synthesized or as supplied, as administrated, and after administration, is needed (Jiang et al., 2008; Oberdorster et al., 2005; Powers et al., 2007).

Chapter 3

3. Characterization of ENM

3.1 Introduction

Through chapter 2 it was underlined that ENM features, such as particle size, shape, surface charge and agglomeration state, may pose adverse effects to human health and environment, driving their toxicological behavior. Thus, the characterization of ENM is a critical step, both considering the early stages of their life, such as development, manufacturing and commercialization, but also investigating ENM behavior under different chemical and physical conditions and their mobility through several environmental compartments. Unfortunately only a very few reports, mainly focused on the characterization of pristine ENM, have been recently published (Hassellöv et al., 2008; Weinberg et al., 2011), but still less attention has been paid to investigate the thermodynamic and kinetic behavior of ENM dispersed in biological and environmental media (Blinova et al., 2010; Brown et al., 2010). The agglomeration and sedimentation rates has been investigated and proposed only recently as a key property for the interpretation of toxicological results (Allouni et al., 2009; Brunelli et al., 2013; Kato et al., 2009; Keller et al., 2010; Petosa et al., 2012). Thus, effective and reproducible dispersion protocols of ENM in different media are required, in order to provide reproducibility and meaningful toxicological results. Moreover, due to the intensive use of ENM in several applications already mentioned in Table 2.2, there is a need to estimate the concentrations of specific ENM in different environmental media as well as the likelihood of exposure to humans and ecosystem receptors (Keller et al., 2013). Therefore, analytical protocols for identification and quantification of different ENM, in several matrixes, are strongly recommended.

Finally, according to the extremely heterogeneous data collected in the field of nanosafety, a comprehensive investigation of specific ENM should therefore include both the basic and the advanced characterization.

3.2 Characterization techniques

Depending on what measurement of a property is required, a wide set of techniques has to be considered because no individual technique can provide a comprehensive characterization of a selected ENM (Dhawan and Sharma, 2010; Warheit et al., 2008). The most frequently employed techniques can be classified in two main categories: imaging techniques, involving some kind of microscopy, and analytical techniques, which are based on spectroscopy.

An extensive list of techniques and their main features are summarized with Table 3.1, underlining also their different limitations.

Table 3.1 – Specification of techniques for characterization of ENM (adapted from (Hassellöv et al., 2008)).

Method	Approximate size range (nm)	Limit of detection	Properties able to measure	Level of sample perturbation
AFM	0.5 to > 1000	ppb-ppm	Average size; size distribution; agglomeration state as powdered and dispersed form	Medium
Analytical Centrifuge	10 to > 1000	Detection dependant	Separation rate; front tracking	High
BET	1 to > 1000	dry powder	Specific surface area; porosity; pore size distribution	High
DLS	3 to > 1000	ppm	Size distribution; stability in liquid	Minimum
Electrophoresis	3 to > 1000	ppm	Separation	Minimum
EM-EELS/-EDX	analysis spot size: ~1 nm	ppm in single particle	Elemental composition	High
ESEM	40 to > 1000	ppb-ppm	Average size; size distribution	Medium
ES-MS	<3	ppb	Elemental composition; impurities	Medium
FFF	Flow FFF: 1-1000; Sed FFF: 50-1000	detection dependant; UV: ppm; Fluo&ICP: ppb	Separation; Size distribution in aqueous dispersions	Low
HDC	5-1200	detection dependant	Separation; Size distribution in aqueous dispersion	Low
ICP-MS	fractionantion dependant	ppt-ppb	Elemental composition; impurities	Low
ICP-OES	fractionantion dependant	ppb-ppm	Elemental composition; impurities	Low
LIBD	5 to > 1000	ppt	Size distribution	Minimum
Microfiltration	100 to > 1000	detection dependant	Size selecting; minimizing the aggregation state	Low-medium
SEC	0.5-10	detection dependant	Separation; size distribution	Medium
SEM	10 to > 1000	ppb-ppm	Average size; size distribution; agglomeration state	High
SLS	50 to > 1000		Size distribution	Minimum
TEM/HR-TEM	1 to > 1000	ppb-ppm	Average size; size distribution; shape; crystal structure; agglomeration state	High
TEM-SAED	Analysis spot size: 1 nm		Average size; size distribution; shape; crystal structure; agglomeration state	High
TGA		dry powder	Elemental composition; impurities	High
Turbidimetry/ nephelometry	50 to > 1000	ppb-ppm	Agglomeration and sedimentation state	Minimum
Ultrafiltration	1-30	detection dependant	Size selecting; minimizing the aggregation state	Medium
WetSEM	50 to > 1000	ppm	Average size; size distribution; agglomeration state	Low
WetSTEM		ppm	Average size; size distribution; shape; crystal structure; agglomeration state	Low
XRD	0.5 to > 1000	dry powder	Crystal structure	High

3.2.1 Imaging techniques

Taking into account the former group of techniques, these can involve light, such as Near-field Scanning Optical Microscope (NSOM); electrons, as Scanning Electron Microscopy (SEM), often coupled with Energy Dispersion X-ray Spectroscopy (EDS), Transmission Electron Microscopy (TEM) and Scanning Transmission Electron Microscopy (STEM); ions, e.g. Field Ion Microscopy (FIM); scanning probe, like Scanning Tunneling Microscope (STM) and Atomic Force Microscope (AFM). One of the key differences between light and electron microscopy is the type of wavelength, which is much shorter for electrons with respect to the wavelength of photons. Thus, the electron microscopy leads to obtain a higher image resolution than the light microscopy. Moreover, since electrons interact much more efficiently with matter, an electron beam under high vacuum is employed in order to reduce scattering. Finally, because of the electron charge, a magnetic field to drive and focus the electron beam is used (Ashby et al., 2009). Here below the basic principles of the electron microscopy are presented, focusing on those employed in this work, i.e. SEM and TEM.

Electron Microscopy

Since conventional visible-light microscopy (VLM) was not sufficient to satisfy the requirements of resolution when investigating NM, thus electron microscopy (EM) was employed to explore this field of research. The smallest feature that can be resolved with a VLM, according to the Rayleigh criterion, is given by Eq.2:

$$\delta = \frac{0.61\lambda}{\mu \sin\beta} \qquad \text{(Eq. 2)}$$

where λ is the wavelength of the light, μ the refractive index of the viewing medium and β the semi-angle of collection of the magnifying lens. μ and β can be approximated to unity, and then δ is about half the wavelength of the light. Considering the wavelength of the visible light, ranging between approx. 400 and 700 nm, it should

be clear that the investigation of NM, requires more powerful microscopes with higher resolution than VLM technique, like electron microscopy.

Electron microscopy is based on the generation of an electron beam by a proper electron gun, accelerating the electrons toward the specimen in order to obtain a wide range of signals, as shown in (Figure 3.1). The basic structure of both Scanning Electron Microscopy (SEM) and Transmission Electron Microscopy (TEM) can be divided into three components: the illumination system, the objective lens and the imaging system. The role of the illumination system is to create electrons and transfer them to the sample, and consists of the electron gun and condenser lenses (Messing, 2011).

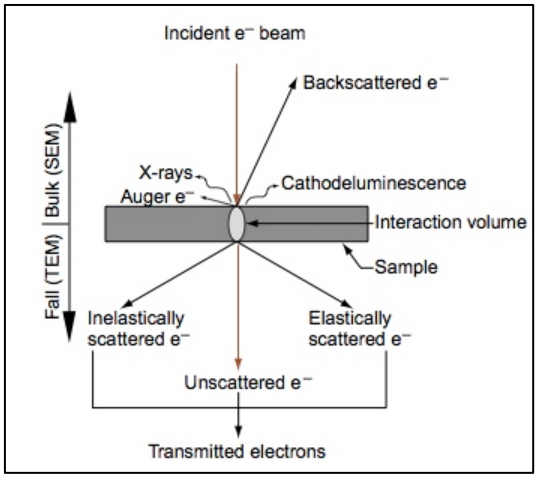

Figure 3.1 – Representative electron beam-sample interactions after irradiation (from (Ashby et al., 2009)).

SEM

Through SEM technique, the collision of electrons derived from an electron beam with the atoms belongs to the sample surface, allows to reveal X rays photons, secondary electrons (SE) or backscattered electrons (BSE). Since electrons have lower wavelength (λ) than photons, EM uses an electron beam, focused by proper lenses, to get very high power resolution, obtaining an observation image mainly based on SE. Indeed, while X rays are electromagnetic waves with λ ranging from 0.01 to 10 nm, the λ of electrons are in the range of 0.1 to 0.005 Å. Among the types of electrons originating in the electron beam, the main differences between SE and BSE are: (i) the outgoing energy from the sample, which is ≤ 50 eV and > 50 eV, respectively; (ii) the depth from which they arise, i.e. few nm for SE and few μm for BSE; (iii) the type of interaction between electrons and surface atoms of the sample, which is anelastic for SE (the total mechanical energy is not preserved) and elastic (constant energy after collision) considering BSE. Furthermore, the information given by SE and BSE are quite different: while SE provide topography of surface and the presence and distribution of electric and magnetic fields, BSE, are used to detect contrast between areas with different chemical compositions, as well as the topography and crystal structure of the sample, since heavy elements (i.e. high atomic number) backscatter electrons are more strongly than lighter elements, appearing brighter in the image. After the generation of electrons by an electron gun, these electrons are accelerated, usually with a voltage between 1kV and 30 kV and demagnified by a set of two condenser lenses. Finally a set of scanning coils force the electron beam to scan over an area of the specimen while the magnetic lenses focus the beam on the sample (Figure 3.2) (Ashby et al., 2009). By operating with SEM, the sample needs to be conductively coated with a conductor material, e.g. gold or graphite, by sputtering on the surface of the insulation material and maintained under ultra high vacuum in order to avoid any interaction between the secondary electrons and gas molecules. The SEM resolution falls approx. between 1 nm and 20 nm in size. The magnification ranges from about 10 times to approx. 500,000 times. The basic layout of a SEM is shown in Figure 3.3 (Ashby et al., 2009).

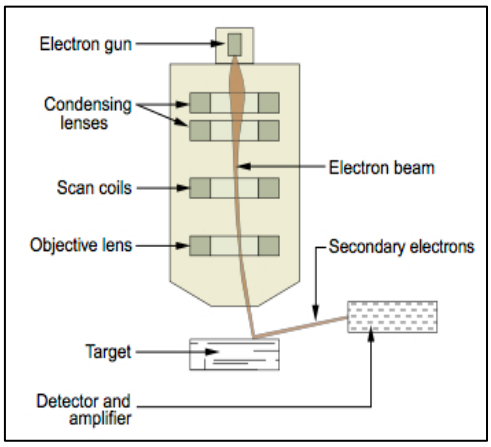

Figure 3.2 – Schematic SEM diagram.

Figure 3.3 –Typical SEM layout.

TEM

This technique used an incident electron beam, transmitted through a very thin (approx. between 5 and 500 nm) specimen at high acceleration voltage, 80-3000 kV, on a conductive grid (e.g. copper grid). Signals are generated by the interaction between the specimen and incident electrons, providing an image by focusing the non-absorbed electrons onto a detector. In general, operating with TEM can reveal three types of transmitted electrons from the sample: unscattered electrons, elastically and inelastically scattered electrons. Unscattered electrons result from incident electrons transmitted through the sample without any interaction with the matter. Thicker areas of the sample have fewer unscattered electrons and appear darker because of the inversely proportional between these electrons and the sample thickness. Scattered electrons by atoms in the specimen during the interaction between the beam and the sample, without losing energy, are called instead elastically scattered electrons. These are transmitted through the remaining portion of the specimen, following Braggs' diffraction law (Eq. 3):

$$n\lambda = 2d\sin\theta \qquad \text{(Eq. 3)}$$

where is an integer, λ is the wavelength of incident wave, d is the spacing between the planes in the atomic lattice, and θ is the angle between the incident ray and the scattering planes. Taking into account that all the incident electrons have the same energy and enter to the sample normal to its surface, the electrons scattered by the same atomic spacing will be scattered by the same angle. These electrons are then gathered by lens and form a pattern of spots, where each spot corresponding to a specific atomic spacing. This diffracted pattern yields information about orientation, atomic arrangements and phases present in the region of interest. Finally, inelastic scattered electrons, caused by incident electrons that interact with atoms of the sample, do not loose energy. Information resulting from these type of electrons can be divided in two groups: (i) inelastic loss of energy by the incident electrons, characteristic of the element, that allows to highlight both compositional and chemical bonding, since these energies are unique to each bonding state of each element; (ii) formation of bands with alternating light and dark lines, knows as Kikuchi bands

(Ohara et al., 2008). TEM operates at high voltages (100 kV to 3 MV), using accelerating voltages of 120, 200 and 300 kV. The TEM resolution limit is determined by various aberrations and not by the accelerating voltage (Ashby et al., 2009). The basic layout of a TEM is shown in Figure 3.4.

Figure 3.4 – A typical TEM layout (from http://www.zmb.uzh.ch/resources/Instruments/electronmicroscopes/philipscm100/TEMCM100ZMBIrchel1.jpg).

3.2.2 Analytical techniques

The analytical techniques include electron spectroscopy, e.g. Energy Dispersive Spectroscopy (EDS) and Electron Energy Loss Spectroscopy (EELS), and vibrational spectroscopy, i.e. Infrared (IF), Fourier Transform Infrared (FTIR) and Raman spectroscopy. Furthermore, other techniques usually employed in the field of ENM characterization are Field Flow Fractionation (FFF), often in combination with Inductively Coupled Plasma Emission spectroscopy (ICP-OES) and Mass Spectrometry (ICP-MS), in order to accurately separate and subsequently detect ENM; Dynamic Light Scattering (DLS), used for the determination of size distribution of particles and colloids in liquid samples; Brunauer-Emmett-Teller (BET) to analyze surface area of a sample; X-ray Diffraction (XRD) for characterizing the crystal structures; analytical centrifuge to investigate the stability of ENM dispersions over time.

Here below the basic principles of the analytical techniques selected on the basis of our research goals are described.

EDS

The EDS method can provide both qualitative and quantitative element analysis, usually coupled with SEM or TEM techniques, using X-rays emitted from electrons. The incident electron beam toward the surface of the specimen causes ionization of electrons of the atoms. After the radiation of the sample, some electrons belonging to the lower-shell are inelastically scattered and emitted from the atom, leaving a vacancy at the lower shell. Some higher-shell electrons fall into the lower shell to fill this vacancy. During this “falling” process electrons emit X-rays, with energies that are unique to the ionized atom, to balance the total energy of the atom itself. Therefore, by measuring the energies of the wavelengths of the X-rays emitted, the composition of the material from a proper region can be determined.

The spatial resolution of EDS technique is a function of the size of the electron probe and the volume of interaction between the beam and the specimen, thus resulting in better resolution when operating with TEM than SEM. In general, a line-

profile or an elemental-map can be obtained when EDS is combined with SEM or TEM system.

XRD

In order to characterize ENM atomic structure, diffraction techniques are usually employed. They are based on the diffraction of an incident beam by reticular planes of the crystalline phases inside the sample. In particular, XRD is based on the measurements of X-ray intensities scattered by the statistically distributed electrons belonging to the atoms of the material. This non-destructive technique is suitable to determine the crystal structure by analyzing the positions and intensities of diffraction peaks typically observed for the well-crystallized material in the range of diffraction angle from 10 to 150°. Moreover the width and the shape of the peak profiles can be obtained, thus evaluating the crystallite size, which usually matches particle size at < 10 nm, through approximated equations, such as Scherrer equation, and microstrain. The Scherrer equation relates the size of sub-micrometre particles, or crystallites, in a solid to the broadening of a peak in a diffraction pattern (Figure 3.5). The formula can be written as:

$$\tau = \frac{K\lambda}{\beta \cos\theta},$$

where τ is the mean size of the crystalline domains, which may be smaller or equal to the grain size; K is the Scherrer constant; λ is the X-Ray wavelength, β is the line broadening at half the maximum intensity (FWHM), after subtracting the instrumental line broadening, θ is the Bragg angle.

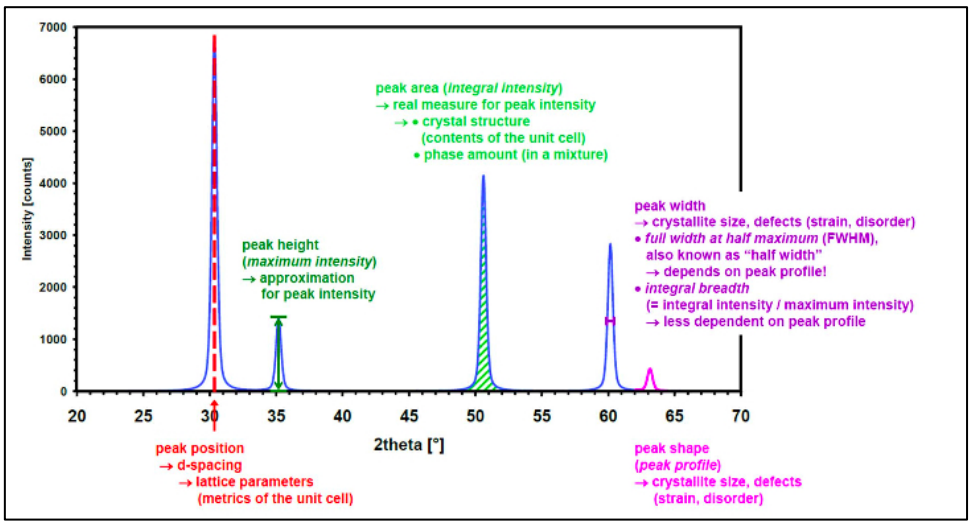

Fig. 3.5 – Information content of an idealized XRD pattern (Mitchell and Perez-Ramirez, 1993).

BET

The BET method is used to measure the specific surface area of solids through the N_2 physisorption, which consists of the N_2 physical adsorption in which the forces between atoms and surface involved are weak (i.e. Van der Waals forces). By BET technique it can be measured the variation between equilibrium and saturation pressure of adsorbent gases at the temperature of adsorption. The BET equation can be expressed by Eq. 4:

$$\frac{1}{\upsilon\left[\left(p_0 - p\right) - 1\right]} \qquad \text{(Eq. 4)}$$

where ν is the adsorbed gas quantity, p_0 is the saturation pressure and p is the equilibrium pressure. Equation 4 is a adsorption isotherm and can be plotted as a straight line as shown in Figure 3.6.

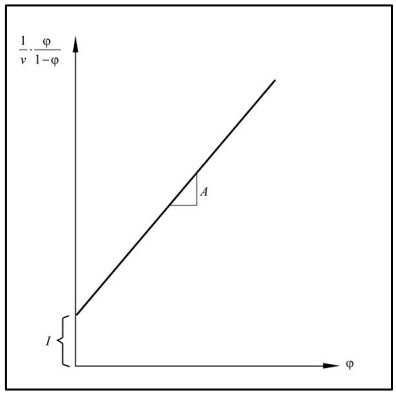

Figure 3.6 – BET plot where $\varphi = p/p_0$. The slope of the line A and the y-intercept I are used to calculate the monolayer adsorbed gas quantity v.

The total surface area S_{total} and a specific surface area S are evaluated by Eq. 5:

$$S_{total} = \frac{\left(\upsilon_m N s\right)}{V} \qquad \text{(Eq. 5)}$$

where v_m is the monolayer adsorbed gas quantity. To calculate the S_{BET} the following equation is used:

$$S_{BET} = \frac{S_{total}}{a} \qquad \text{(Eq. 6)}$$

where N is the Avogadro's number, s is the adsorption cross section of the adsorbing species, V is the molar volume of adsorbate gas and a is the mass of adsorbent, in grams. A typical adsorption-desorption isotherm and pore diameter distribution are shown by figures 3.7-3.8.

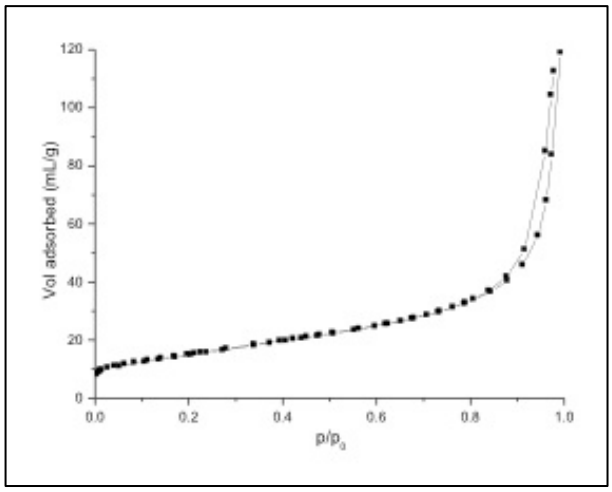

Figure 3.7 – A typical adsorption-desorption isotherm by BET method.

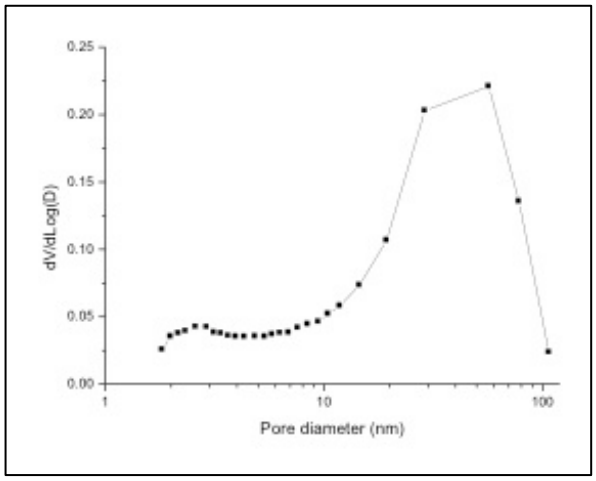

Figure 3.8 – A typical pore size distribution by BET method.

Inductively Coupled Plasma techniques

An Inductively Coupled Plasma is a type of plasma source, i.e. an ionized gas with zero total electric charge, used both in emission spectroscopy and in mass spectrometry. Plasma is maintained by the interaction between a radiofrequency (RF) field and argon (Ar^+) ionized gas. The plasma reaches temperatures up to 10000° C; temperatures useful for the analysis of the samples are between 5500° C and 8000° C, leading to the complete ionization of the elements present in the sample and minimizing possible chemical interferences.

ICP-MS

This analytical technique is a type of highly sensitive mass spectrometry for the determination of several elements. A typical ICP-MS interfaces a plasma source, inductively coupled with a proper mass spectrometer, as a function of the type of the investigation (see Figure 3.9). The mass spectrometer separates the ions of the chemical species included in the sample, generated from plasma, according to their mass/charge (m/z) ratio. The ions thus selected are directed to a detector, which determines their number.

The five main components of this instrument are therefore:

- nebulizer;
- spray chamber;
- plasma torch;
- cones: sampler and skimmer;
- mass spectrometer.

Figure 3.9 – A typical ICP-MS layout.

The nebulizer converts the sample into microscopic droplets while the spray chamber removes the droplets that are too large to be analyzed and homogenizes aerosols. Plasma torch consists of two concentric quartz tubes and within this torch plasma is produced. In the central tube, the sample carried by Ar^+, flows down, coming from the spray chamber. Ar^+ flows down through the outer tube for supplying the plasma. In the final part of the torch, on the opposite side with respect to the spray chamber, there is a coil of copper connected to a RF generator. Plasma is generated when Ar^+ becomes conductive for exposure to an electric discharge. The presence of electric current generates a magnetic field. Ar^+ subjected to electric discharge loses some electrons, which are accelerated by the magnetic field; within the induced magnetic field, the charged particles (electrons and ions) are forced to flow in a circular path. As soon as these particles come in contact with the electromagnetic field heat is developed and a further ionization is observed.

When the sample reaches the torch, the atoms of the chemical elements undergo desolvation, vaporization, atomization and ionization of molecules. The first process separates the solvent decomposing the sample into microscopic particles; vaporization decomposes the particles in a molecular gas; the atomization and ionization dissociate the atoms and ions.

The interface zone is the link between the mechanism of plasma generation, which operates at ambient pressure and at a temperature of 7500° C, and the mass spectrometer, which operates in conditions of high vacuum and low temperature. This specific area is composed of two coaxial cones, i.e. the sampler and skimmer cones, which are two metals disks with a small hole (~1 mm) in the center for sampling the center portion of the ion beam coming from the ICP torch. Due to the small diameters through the disks, ICP-MS has some limitations as to the amount of total dissolved solids in the samples.

Within the interface zone, a pump draws most of Ar^+ allowing ions to pass through the hole of 0.9 mm of the skimmer cone, place at 10 mm from the first. In addition to the skimmer cone, ions are carried into the low pressure region of the mass spectrometer (pressure < 10^{-5} torr) and temperature around 280° C. A lens system focuses the beam to an analyzer, among which the most common is a quadrupole, which enables the serparation analytes according to the mass/charge (m/z) ratio.

The mass spectrometry is based on the possibility of separating a mixture of ions depending on their m/z ratio, generally via static or oscillating magnetic fields. The diagram that shows the abundance of each ion as a function of the ratio m/z is referred to as mass spectrum, typical of each compound, since it is directly related to its chemical structure and to the conditions of ionization. A computer connected to the instrument allows the extremely deep exploration of the mass spectrum obtained, ensuring an excellent resolution and high sensitivity, that it means the ability to detect a slightly peak pronounced immediately adjacent to one of the most emerging. Finally, ions coming out to the quadrupole are captured by a detector, which it is able to produce electrical signals proportional to the ion flux transmitted by the analyzer mass.

DLS

This technique is one of the most common used to measure, through a monochromatic wave, the fluctuations of the intensity of scattered light by particles dispersed in a fluid, caused by the Brownian motion, which is the random movement of particles due to the radiation by the solvent molecules that surrounded them. The incident light wave through the sample can be thought of as consisting of a very rapidly oscillating electric field, of amplitude E_0 (approx. frequency 10^{15} Hz). This alternating field near a particle induces all of the electrons, which are free to be influenced, to oscillate at the same frequency, giving rise in turn to a new oscillating electric field which radiates in all directions. Because in the field of scattering measurement, the quantity of interest is the intensity I_s of the scattered wave instead of the amplitude E_s, this intensity can be calculated as follow: $I_s = (E_s)^2$.

The intensity of scattered light by a single particle depends on its molecular weight and overall size and shape, and also on the difference in the refractive indices of the particle and the surrounding solvent. This dependence is particularly simple when the particle diameter is much smaller than the laser wavelength employed, i.e. when dealing with NP. Thus, in this case the scattering from this type of particles illuminated by a vertically polarized laser will be isotropic, i.e. equal in all directions. By the Rayleigh approximation, $I \propto d^6$ and also $I \propto 1/\lambda^4$, where I = intensity of scattered light, d = particle diameter and λ = laser wavelength.

The fluctuations of the scattered intensity of light induced by the laser are then analyzed by a correlator, which uses some algorithms to compare several signals coming from a detector, placed after the sample. In order to correlate the particle dynamic with the scattered intensity recorded by the detector, a correlation function is used:

$$G(\tau) = \int_0^\infty I(t)I(t+\tau)dt \qquad \text{(Eq. 7)}$$

where τ is decay time and t is the intensity of scattering. By equation 7 it can be stated when a fast decay occurs, smaller particles are detected within the fluid while larger particles show a slower decay over time.
The size of a particle is then calculated by the Stokes-Einstein equation as follow:

$$d(h) = \frac{kT}{3\pi\eta D} \qquad \text{(Eq. 8)}$$

where d(h) = hydrodynamic diameter, D = translational diffusion coefficient, k = Boltzmann's constant, T = absolute temperature and η = viscosity. Thus the equation 8 highlights that the value measured by DLS, called hydrodynamic diameter, is referred to how a particle diffuses within a fluid. This value is the diameter of a sphere that has the same translational diffusion coefficient as the real particle. D will depend not only on the size of the particle but also on any surface structure, as well as the concentration and type of ions in the medium.

In general, a typical DLS, as shown in Figure 3.10, comprises six main components: (i) a monochromatic light beam, i.e. a HeNe laser with λ = 632.8 nm, provides a light source to radiate the sample; (ii) a cuvette to contain the sample; (iii) a detector for measuring the scattered light, in general positioning at 90° from the source beam; (iv) an attenuator to adjust the laser intensity over time with a range of attenuation from 100% to 0.0003%; (v) a correlator to digitalize the scattering intensity signal from the detector, comparing the scattering intensity of particles at consequently time intervals for deriving the rate at which the intensity is varying; (vi) a computer to analyze data collected.

DLS could be employed both as reference technique for primary but also secondary characterization of ENM.

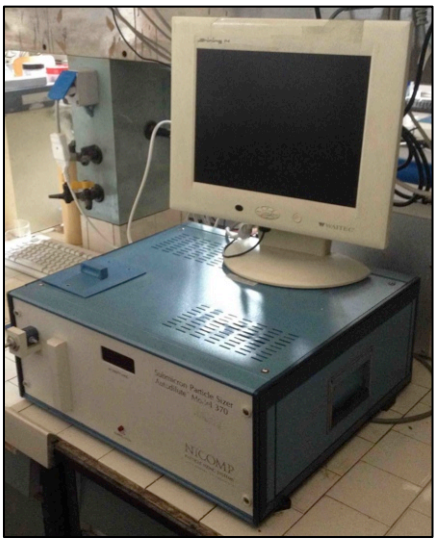

Figure 3.10 – Nicomp 370 DLS (Santa Barbara, CA, USA) layout employed in this thesis.

Analytical Centrifuge

The analytical centrifuge is usually employed to investigate demixing phenomena of a sample in a liquid over time, like sedimentation, flotation and coalescence. The basic principle is represented by a continuous transmission of a monochromatic light beam through a sample, which is placed in a proper vessel, over the total length of the measurement vessel. In detail, parallel light I_0 illuminates the entire sample cell and the transmitted light I is detected by thousands of sensors arranged linearly across the whole sample from the top to the bottom with a micro-scale resolution (see Figure 3.11). The resulting transmission profile shows the intensity of the light transmitted as a function of the radial coordinates. The radius specifies the distance from the center of the rotor. Therefore the largest radius corresponds with the bottom of the vessel. By calculating the area below the profile obtained by the monochromatic light beam that irradiates the sample (see Figure 3.12), both the sedimentation rate and the shifting (called front tracking) of the sample

from the beginning to the bottom of the cell over time can be evaluated. The analytical centrifuge employed is shown in Figure 3.13.

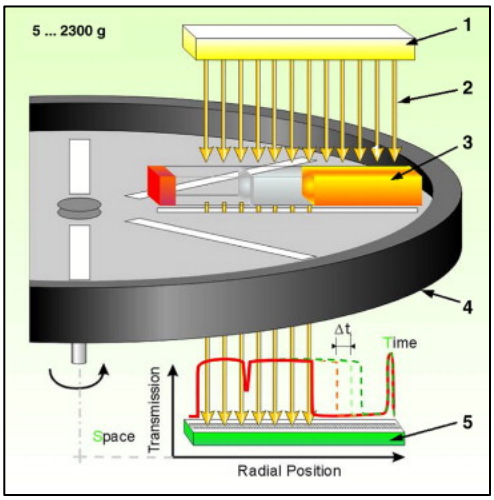

Figure 3.11 – A general scheme of the multisample analytical centrifuge. The light source (1) sends out parallel NIR-light (2), which passes through the sample cells (3) lying on the rotor (4). The distribution of local transmission is recorded over the entire sample length by the CCD-Line detector (5) (from (Lerche and Sobisch, 2007).

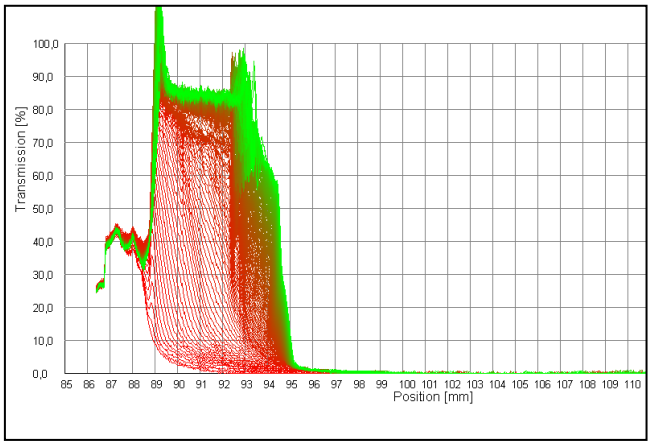

Figure 3.12 – A typical transmission profile obtained during centrifugation of a nano-based paint at 2000 rpm (corresponding to a centrifugal acceleration of 500 x g). The first profiles given by the centrifuge are in red while the last obtained are in green. The

colored area ranging from 88 to 95 mm represents the moving boundary liquid-solid as a function of the transmission % over time.

Figure 3.13 – The 316 LUM G.m.B.H. (Berlin, D) analytical centrifuge employed in this thesis.

Chapter 4

4. Experimental section

4.1 Introduction and objectives

As previously discussed through paragraph 2.4, the physico-chemical properties of ENM are expected to influence the biological response and effects on humans and environment (Suresh et al., 2013). Since the parameters causing adverse effect vary depending on which ENM is considered, there is still an urgent need to carry out a comprehensive characterization of ENM. Thus, it is crucial to extend primary and secondary characterization to better link the investigation of pristine ENM with characterization under test conditions.

According to recent requirements from nanosafety and to the latest Communication from European Commission (COM(2012)527, 2012), the methodological approach was divided as follows: (i) completion of primary characterization data collection from pristine ENM; (ii) secondary characterization of ENM, oriented to assess the ENM behavior in environmental media, especially in terms of agglomeration and sedimentation, as well as to investigate the ENM biodistribution after toxicological testing, to support the field of nanotoxicology. In addition, because of the need to standardize protocols suitable for ENM risk assessment, highlighted by recent literature (Dusinska and NanoTEST-consortium, 2009; Macken et al., 2012; Magdolenova et al., 2012), both dispersion protocols of tested ENP in several biological media and analytical protocols for the ENM identification and quantification in biological samples from toxicological testing, have been developed.

4.2 Materials and methods

Samples

Table 4.1 shows the list of ENM investigated in this work. The NRCWE rutile series have been chosen by project partners based on a pre-selection study to identify a comparable (phase, purity, and highly dispersable) small and large nano-size TiO_2 of which the small-size has been functionalized to obtain a positive (NRCWE-002) and negative (NRCWE-003) charge. All other samples are obtained from the NAPIRA source at the Joint Research Centre at Ispra, Italy, except P25 and n-Ag 47MN-03, purchased by manufacturers.

Table 4.1 – Summary of the selected ENM.

Material	**NM code**	**CAS-number**	**Original Source**
n-TiO_2	NRCWE-001	13463-67-7	NanoAmor
n-TiO_2	NRCWE-002	13463-67-7	Modified NRCWE-001
n-TiO_2	NRCWE-003	13463-67-7	Modified NRCWE-001
n-TiO_2	NRCWE-004	13463-67-7	NaBond
n-TiO_2	NM-101	13463-67-7	Hombikat UV100
n-TiO_2	P25	13463-67-7	Evonik Degussa Aeroxide P25 Degussa
n-ZnO	NM-110	1314-13-2	BASF Z-Cote
n-ZnO	NM-111	1314-13-2; 2943-75-1	BASF Z-Cote HP1
n-Ag	NM-300	7440-22-4	RAS GmbH
n-Ag	47MN-03	7440-22-4	Inframat
MWCNT	NM-400	7782-42-5	Nanocyl
MWCNT	NM-402	7782-42-5	Arkema Graphistrength C100

4.2.1 Primary characterization

Techniques and details about samples preparation employed by project partners for ENM primary characterization are described here below. Within primary ENM investigation, shape and size distribution by TEM, as well as inorganic impurities by ICP-OES were the performed activities of this thesis.

Ultrahigh-pure water (minimum resistivity: 18.2 MΩ cm), that hereinafter will be referred as MilliQ, produced by a MilliQ water purifier system (Millipore, Bedford, MA, USA), was used throughout this work.

Electron microscopy

Scanning Electron Microscopy (SEM) analysis was conducted on dried powder sub-samples by means of a scanning electron microscope JEOL JSM 5600 LV (Tokyo, Japan). Transmission electron microscopy was carried out using a JEOL (Tokyo, Japan) 3010 transmission electron microscope operating at 300 kV.

Samples were prepared on carbon-coated TEM Cu-grids after dispersion in approximately 15 µL of ethanol (EtOH). Particle dispersions in EtOH were deposited onto the inner meshed surface of the TEM grid. After a few seconds, the excess solution was removed with a filter paper and the grids were dried overnight in the dark at 25 °C. The particle size distribution was determined from the analysis of between 500-1000 particles, randomly-examined from collected micrographs. SEM analysis of P25 and 47MN-03 samples were not yet performed due to the limited available samples amount.

XRD observations

The silver sample, NM-300, was measured once as a liquid in a capillary with transmission; all other samples were measured as powder in reflection mode. The diffractometer used for all samples was a Bruker D8 with Bragg-Brentano setup, equipped with a monochromator and using Cu radiation (0.0197, scan time 1 s pr. step).

One set of analyses of the n-TiO_2 and n-ZnO were conducted by addition of a known amount of an α-quartz reference material (NIST SRM1878a) for quantitative determination of the volume fractions of the crystalline and X-ray diffraction amorphous phases by Rietveld refinement. The uncertainty in estimation of the amorphous fraction is relatively high (i.e. ±10 w%) due to the difficulty in preparing homogeneous samples, except for P25, (i.e. ±1 w%). 47MN-03 was not measured due to the limited sample amount available.

Average crystallite sizes were also determined using Rietveld refinement using the program TOPAS. Potential deviation from the true value mainly depends on the quality of the X-ray diffraction pattern.

Specific surface area and pore size distribution analysis

BET nitrogen physisorption measurements were performed at 77K using an ASAP 2000 sorptometer (Micromeritics, USA). The samples (~400 mg) were degassed at 473K for 2 hours prior to the sorption experiment. The total pore volume, V_{tot}, was measured as the adsorbed amount of N_2 at P/P_0 values near to 0.98 allowing the surface area to be calculated by the BET equation. The pore size distribution was determined by the Barrett-Joyner-Halenda (BJH) method (Barrett et al., 1951) applied to the N_2 desorption isotherm branch.

Elemental analysis

The presence of any inorganic impurities in the tested ENM was investigated by digesting powdered ENM with various oxidant mixtures, temperature and time (carefully optimized for each sample) in an Ethos MLS-1200 Mega (Milestone Corporation, Sorisole, Italy). The resulting solution was then diluted to 25 ml of MilliQ, which was analyzed by an Optima 5300DV ICP-OES (Perkin-Elmer, MA, USA).

All employed materials were teflon-based and properly handled in order to remove/minimize undesired impurities during ICP analyses.

Raman spectroscopy

The structural quality of the MWCNT samples (NM-400 and NM-402) were assessed from Raman spectroscopy, using a Horiba Jobin-Yvon Labram HR Raman spectrometer equipped with a CCD detector with a resolution of 1024 x 256. The wavelength used was 632.82 nm to assess the intensity of the D (Defect) and G (Graphite) bands for preliminary quality assessment. The data should be used with caution as there was no shielding against light causing some signal interference in the laboratory where the analysis was conducted.

4.2.2 Secondary characterization

The secondary characterization performed was divided in: (I) an investigation of ENM interactions with biological samples, assessing both ENP stability in biological media and ENM biodistribution in a secondary target organ from toxicological testing; (II) a study on agglomeration and sedimentation behavior of n-TiO_2 P25 in both synthetic and real waters, also determining the actual P25 exposure concentration over the experiment time course, tipycally applied in toxicological testing.

The behavior of ENP listed in Table 4.1, dispersed in biological media usually used for cell culture, was carried out by Dynamic Light Scattering (DLS) and analytical centrifuge, except for CNT. According to their physico-chemical characteristics (i.e. elongated shape, hollow structure, high aspect ratio) and to results from experiments performed within this work (data not shown), CNT stability was not possible to be evaluated, due to the formation of large and elongated agglomerates that prevent a correct estimation of their size distribution and sedimentation rates by applied techniques.

As a result, tailored dispersion protocols for each ENP tested were developed, according to project partners requirements. The description about particle handling and sonication protocols is presented in paragraph 4.3.

Furthermore, the secondary characterization was extended to a biodistribution study, to identify and quantify ENM in a secondary target organ, i.e. the mice brain from toxicological testing. The ENM studied is listed in Table 4.1, except for n-TiO_2 P25 and n-Ag 47MN-03, not belonging to the ENPRA project. Microwave-assisted digestion method, followed by ICP-MS analysis, were the employed techniques. Firstly, the extraction efficiency of 5 ENM (n-TiO_2 NM-101; n-ZnO NM-110; n-Ag 47MN-03; MWCNT NM-400 and NM-402; total number of samples: 115), specifically added to dry biological samples, was evaluated. Furthermore, according to ENM extraction results, quantification of several ENM (i.e. n-TiO_2 NRCWE-001; n-TiO_2 NRCWE-002; n-TiO_2 NRCWE-003; n-TiO_2 NRCWE-004; n-TiO_2 NM-101; n-ZnO NM-110; n-ZnO NM-111; n-Ag NM-300; MWCNT NM-400 and MWCNT NM-402; total number of samples: 240) from the same biological matrix was carried out.

An Ethos MLS-1200 Mega (Milestone Corporation, Sorisole, Italy) microwave oven for digesting samples with acid mixtures, temperature and time, depending on

each ENM, followed by an Agilent (Tokyo, Japan) 7700x ICP-MS for ENM quantification, were employed.

Nitric acid (HNO_3) puriss. p.a., ACS reagent ISO ≥69% and Hydrochloric acid (HCl) reagent grade 37% were purchased from Sigma Aldrich (Steinheim, Germany). All employed materials were teflon-based and properly handled in order to remove/minimize undesired impurities during ICP analysis.

Toxicological experiments performed by ENPRA project partners are described here below.

Animals

Female C57BL/6N mice of 7-8 weeks with an average body weight of 20.3 g (ranging between 18.2-21.4 g) were obtained from Taconic (Ry, Denmark). All mice were given free access to tap water and standard mouse chow diet. The mice were kept under specific pathogen free (SPF) conditions and were allowed to acclimatize for 1–2 weeks before they entered the experimental protocol. Husbandry conditions were maintained according to all applicable provisions of the Dutch national law: Experiments on Animals Act. The experiments were approved by an independent ethical committee prior to the study and performed at the National Institute of Public Health and the Environment (RIVM, Netherlands).

Intratracheal instillation

According to the stock dispersions preparation, further described in paragraph 4.3.2, the mice were intratracheally instilled with ENM in Table 4.1 (except for P25 and 47MN-03, not belonging to the ENPRA project) under 4% isoflurane anesthesia, with a dose range of 0, 1, 4, 8, 16, 32, 64 and 128 µg/mouse. Vehicle control mice for NM-101, NRCWE-001, NRCWE-002, NRCWE-003, NRCWE-004, MWCNT NM-400, MWCNT NM-402 received the dispersion media with 2% serum without ENM. For both types of n-ZnO (i.e. NM-110 and NM-111), this included 0.5% ethanol in MilliQ with 2% mouse serum. For n-Ag NM-300, the vehicle control was the commercially available Ag dispersant (i.e. 9JRC Nanorepository) with 2% serum. The animals were sacrificed 24 hours after instillation. The brains were taken out approximately 10 minutes after

exsanguination and taking out the lungs. The brains were snap-frozen in liquid nitrogen,sterilized, lyophilizated and stored at -80°C.

Further investigation was performed to assess the n-TiO_2 P25 stability over time, in both synthetic and real aqueous solutions by means of nephelometry and DLS. The sedimentation profiles over 50 h (30 s measurements every 15 min), as typically required by toxicological tests, at different P25 concentrations (0.01, 0.1, 1 and 10 mg/l), including those likely to be found in natural waters, were obtained as relative variation with time of the scattered light normalized with respect to the initial scattering value (I/I_0). According to Lambert-Beer law at low concentrations (i.e. $<10^{-5}$ M), which states that the light intensity is directly proportional to the dispersed particles concentration, the P25 sedimentation profiles were plotted as $\ln(C/C_0)$ vs. time, where C is the concentration at a defined time and C_0 is the initial concentration. Furthermore, agglomeration and size distribution of P25 dispersed in aqueous solutions were assessed by DLS 0.2, 25 and 50 h after dispersions preparation, excluding the lowest concentration (i.e. 0.01 mg/l) because of its sensitivity (too low signal, i.e. <60 kHz).

All experiments carried out within the secondary characterization were performed in triplicate and reported results were the average of the intensity of the light scattered or transmitted from the dispersed ENP in different media.

Here below a description about the media and sample preparation for each technique employed is presented.

Media preparation

Biological media

Dulbecco's Modified Eagle's Medium Nutrient Mixture (DMEM, cod. D6046), Dulbecco's Modified Eagle's Medium Nutrient Mixture F-12 HAM (DMEM-F12-HAM, cod. D6421), Roswell Park Memorial Institute 1640 Nutrient Mixture (RPMI-1640, cod. R8758), as well as Fetal Bovine Serum (FBS, cod. F9665), were obtained from Sigma-Aldrich (Steinheim, Germany).

Synthetic and real sea and estuarine-like water media (Brunelli et al., 2013)

The artificial fresh and seawater solutions (Allen et al., 2010) were prepared by dissolving analytical reagent grade inorganic salts from Sigma-Aldrich (St. Louis, MI, USA) in MilliQ by magnetic stirring; the solutions were then aerated overnight with filtered laboratory air in order to guarantee air saturation (pH 8.2 ± 0.2). A common growth medium for freshwater crustaceans (e.g., Daphnia magna) was prepared according to ASTM E729-E796 protocol (ASTM and E729-96, 2004 (2007)) and used as synthetic freshwater (AFW); two artificial seawater solutions (ASW1, ASW2), usually employed as culture media for marine algae and marine invertebrates such as *Phaeodactylum tricornutum* and *Artemia franciscana*, respectively, were prepared according to ASTM E724-E798 protocol (ASTM and E724-98, 2004 (2012)) and utilized as synthetic seawaters: ASW1 and ASW2 slightly differed in the ionic composition, salinity and IS. The synthetic solution AEW (0.5 % salinity) was instead obtained by appropriate dilution with MilliQ of the salt solution ASW2. Samples of natural waters were collected in the Venice Lagoon (Italy) (lagoon water, LW) and in the Northern Adriatic Sea, 6 km far from the coast (seawater, SW), respectively. All solutions were stored at 4 °C in the dark and filtered at 0.22 μm before use. The solution salinity of natural salt waters was measured at 22 °C with a salinometer PCE-0100 (Atago, Tokyo, Japan), while their solutions specific conductance was determined at 22 °C with an electrical conductivity meter HD 8706 (DeltaOhm, Padua, Italy). The organic carbon content was determined by using a Total Organic Carbon analyser TOC-5050A (Shimadzu, Kyoto, Japan). Samples were previously acidified with H_3PO_4 (25 % w/w) and the inorganic carbon was then removed by heating and ventilation for 5 min (Nieuwenhuize et al., 1994). Compositions and physico-chemical parameters of prepared aqueous solutions are reported in Table 4.2. The salinity value of the artificial solution AEW was selected on the basis of the thalassic series, which identifies 0.5 % salinity as one of the boundary values of oligohaline waters (Mantyla, 1987). The AFW solution contained only 0.2 g/l of the naturally occurring pH buffer $NaHCO_3$ and represented the electrolyte back- ground reference.

Table 4.2 - Chemical composition and physico-chemical characteristics of the tested aqueous solutions (AFW: artificial freshwater; AEW: artificial estuarine water; ASW1: artificial seawater 1; ASW2: artificial seawater 2; LW; lagoon water; SW: seawater).

	AFW	AEW	ASW1	ASW2	LW	SW
Ionic Composition (mg/l)						
Ca^{2+}	<0.1	5.6	274.5	404	413	427
K^{+}	<0.1	5.9	344	402	414	467
Mg^{2+}	<0.1	18.5	1167	1296	1341	1405
Na^{+}	54.7	156.1	10205	10922	11289	11648
Sr^{2+}	<0.1	<0.1	<0.1	6.13	<0.1	<0.1
Cl^{-}	<0.1	274	17650	19203	19256	21053
BO_3^{3-}	<0.1	0.6	21.8	28.8	54.8	71.9
Br^{-}	<0.1	0.8	<0.1	67	142	153
SiO_3^{2-}	<0.1	<0.1	<0.1	10.6	<0.1	<0.1
SO_4^{2-}	<0.1	46.1	2986	3228	2933	2988
HCO_3^{-}	145.2	1.8	145.2	145.2	<0.1	<0.1
pH	8.14	8.06	8.1	8.08	8.14	8.17
DOC (mg/l)	<0.1	<0.1	<0.1	<0.1	1.8	2.16
Specific Conductance at 22 °C (mS)	0.21	0.67	42.8	47.3	41.8	47.8
Salinity (‰)	< 1	< 1	33	35	32	35
IS (mmol/l)	2.0	9.8	630	690	932	984
Divalent cation concentration (mmol/l)	<0.1	1.0	55	63	92	102

Size distribution and agglomeration rate in liquid media

Hydrodynamic size distribution and agglomeration rate of ENP dispersed in biological and aqueous media was determined by Dynamic Light Scattering (DLS) with a Nicomp Submicron Particle Sizer Autodilute® Model 370 (Santa Barbara, CA, USA), using a 90° scattering angle. Approx. 2 ml of ENP dispersion in borosilicate glass culture tubes 6x50 mm was used for each measurement. The viscosity and refractive index were selected as a function of each medium tested; temperature was set at 37°C, as *in vitro* experiments, for biological dispersions and at 22°C for synthetic and real sea and estuarine-like aqueous dispersions.

Sedimentation

The sedimentation behaviour of ENP in biological media was investigated by means of an analytical centrifuge 316 by LUM G.m.B.H. (Berlin, D). According to all *in vitro* experiments performed at human body temperature and last up to a few days, T and speed were set at 37°C and 1000 rpm respectively, simulating 24 h.

Moreover, regarding P25 dispersed in synthetic and real water samples, the settling over time of n-TiO_2 was carried out by using a fluorescence spectrophotometer LS55 (Perkin Elmer, Waltham, MA, USA) employed as nephelometer, by setting $\lambda_{ex} = \lambda_{em}$ (Lawler and Townshend, 2005), measuring the light scattered by particles at 90° with respect to the light source. Emission filter opening, excitation and emission slit widths were 2.5 and 20 nm, respectively, according to the investigated sample and initial concentrations.

5 Results

5.1 Primary characterization

A typical physico-chemical characterization for sample n-TiO_2 NRCWE-001 is presented here below, while Annex 1 is dedicated to primary characterization data about all others ENM, in order to increase readability of Chapter 4. With regard to analysis by TEM, particles size distribution of ENM samples was calculated, asking specifically to projetc partners, to ensure the relevance of sampled areas as well as to prepare as homogeneous and dispersed as possible samples, in order to avoid particles agglomeration to finally achieve a reliable statistical processing. Both particles size distribution from TEM images and ENM inorganic impurities of concern were carried out within this thesis and the results were added to primary characterization data. A summary of all primary characterization data collected in collaboration with both ENPRA and PRIN project partners is summarized in Tables 5.4a-b.

n-TiO_2 NRCWE-001

NM-Source: NRCWE, Copenhagen, Denmark
Producer/Vender: NanoAmor
Content: Titanium dioxide powder
Coating: no coating (from supplier)
Appearance: White, ultrafine powder

Phase composition

XRD analyses suggest that NRCWE-001 mostly consists of rutile (75 weight%), as shown in Figure 5.1. The sample may contain some amorphous material (19 w%) and minor anatase (6 w%). Anatase was not observed in the second analysis nor in

the surface modified versions of the same sample (NRCWE 002 and 003). Later

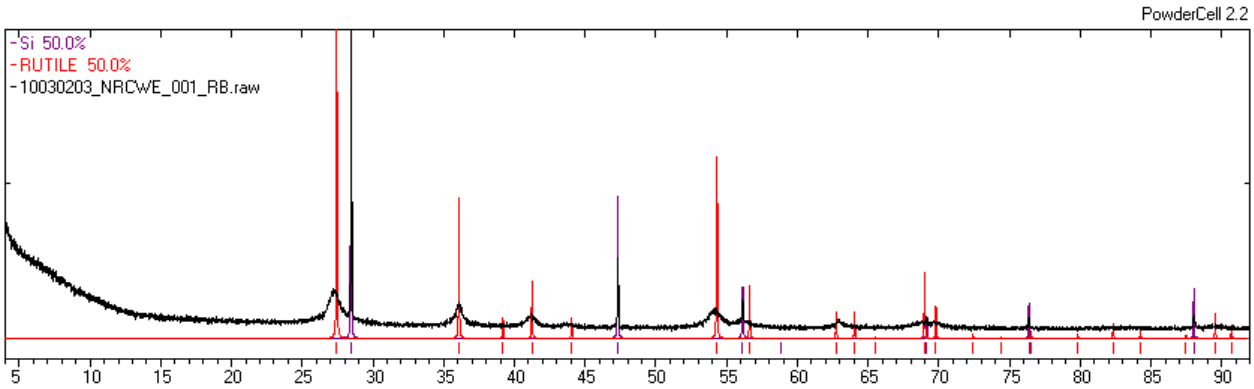

measurements on the pure material have not shown any anatase.

Figure 5.1 - X-ray powder diffraction data show the presence of rutile (red peaks) and the dopant silicon (purple peaks). Y-axis is referred to intensity (arbitrary unit) and x-axis to degrees of diffraction angle (2θ).

Particle Size and Morphology

XRD analyses highlight a crystallite size of 10±1 nm. SEM analysis showed the presence of agglomerates with irregular shape from 0.5 μm to approx. 25 μm, with no appreciable predominant size (Figures 5.2a and b). By TEM, the sample appeared with mostly irregular polyhedral particles, with an average size range for 80% particles from 80 to 400 nm (Figures 5.2c to f).

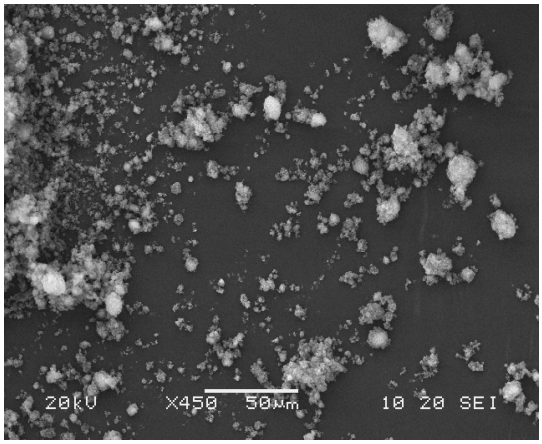

a)

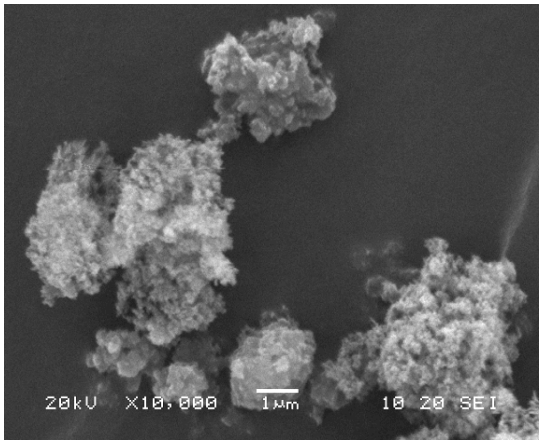

b)

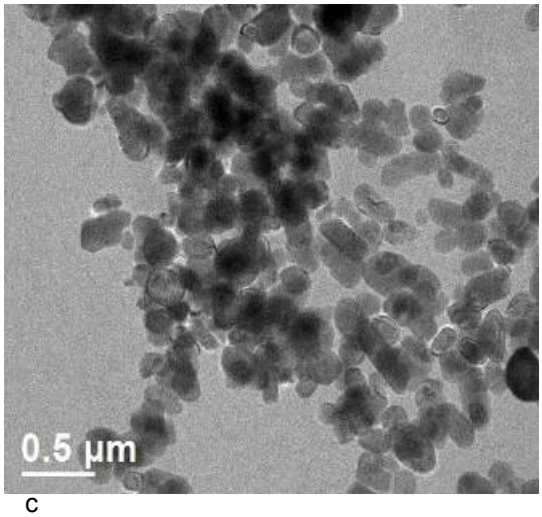

c

c)

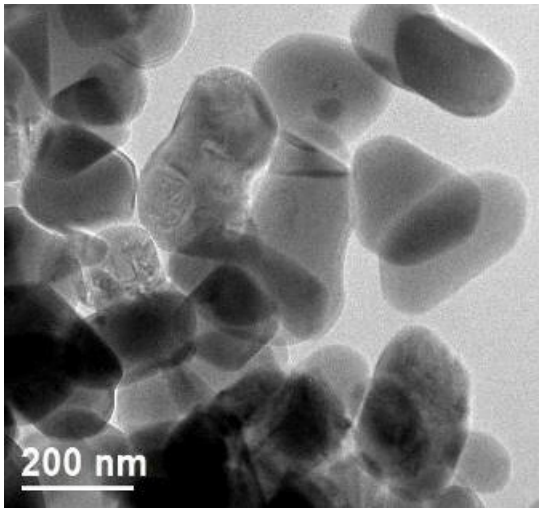

d)

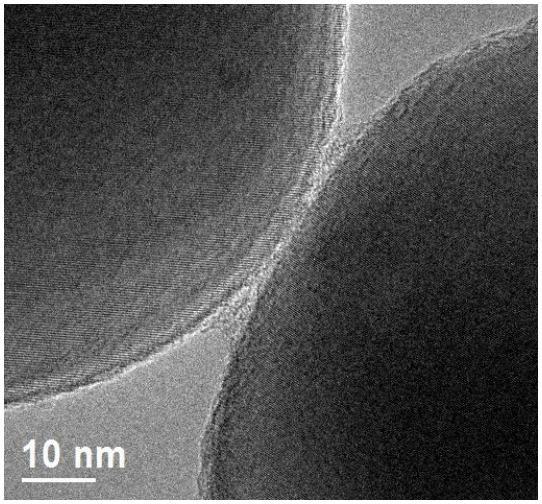

e)

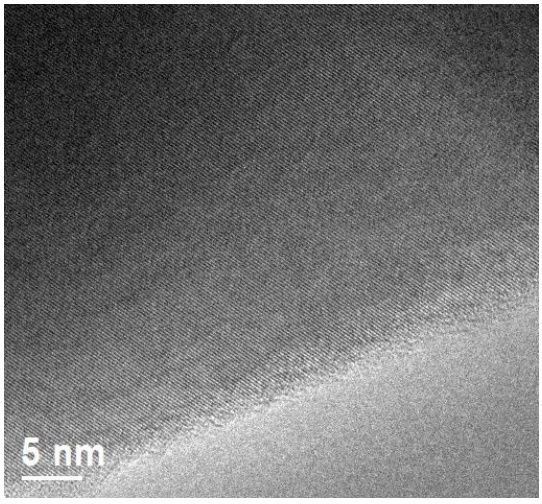

f)

Figure 5.2 – EM pictures of n-TiO_2 NRCWE-001. a) Overview of powder particle aggregates and/or agglomerates. b) Close-up showing the surface morphology of TiO_2 agglomerates/aggregates TEM pictures of NRCWE 001. c) Agglomerated TiO_2

particles; d) Close-up showing mixture of agglomerates and single particles; e) Amorphous material at the interface between two particles; f) High-resolution image showing high crystallinity to the rim of the crystallites.

BET Surface area

Specific surface area was 99±0.5 m^2/g.

Elemental analysis

Inorganic impurities, detected by ICP-OES, are summarized in Table 5.1. No individual impurity particles or crystal structures of the elements listed below were identified by TEM-EDX.

Table 5.1 – Trace elements impurities revealed in n-TiO_2 NRCWE 001.

Element	**Concentration (µg/g)**	**LOD (µg/g)**
Co	764±35	0.1
Fe	151±11	0.1
Cr	43±1.7	0.3
V	4.6±0.8	0.1
Zn	4.3±3.2	0.2
Mn	2.1±0.2	0.01

Table 5.2a – Data regarding physico-chemical features of the tested ENM.

	n-TiO_2 NRCWE-001	**n-TiO_2 NRCWE-002**	**n-TiO_2 NRCWE-003**	**n-TiO_2 NRCWE-004**	**n-TiO_2 NM-101**	**n-TiO_2 P25**
Coating*	-	tri-ethoxypro-pylaminosilane	Caprylamine	-	-	-
Primary size declared (measured)[1] (nm)	80-400 (80%)	80-400	80-400	1-2000	4-100	21 (27±10)
Crystallite size[2] (nm)	10±1	9.7±0.4	10.1±0.5	94	7	21
Shape[1]	Irregular polyhedral particles	Irregular polyhedral particles	Irregular polyhedral particles	Different morphologies identified	Two morphologies identified	Irregular polyhedral and some spherical particles
Crystalline phases (%)[2]	An:Br:Ru:Am: 6:0:75:19	An:Br:Ru:Am: 0:0:62:38	An:Br:Ru:Am: 0:0:70:30	An:Br:Ru:Am: 0:0:44:56	An:Br:Ru:Am: 48:0:1:51	An:Br:Ru:Am 86.5:0:13.5: 0
Specific surface area[3] (m^2/g)	99 (±0.5)	84.3 (±0.5)	84.2 (±0.5)	5.1 (±0.5)	322 (±2)	54(±0.2)
Pore Volume[3] (ml/g)	-	-	-	-	0.4	0.2
Inorganic Impurities of concern (ug/g)[4]	Co (764±35) Fe (151±11)	Co (758±32) Fe (161±12)	Co (762±33) Fe (155±9)	Co (877±24)	Co (921±37) Cr (53±9) Fe (36±11)	Mg (323±57) Na (24±6)

Detected by [1] TEM; [2] XRD; [3] BET; [4] ICP-OES / ICP-MS

*Data from supplier

Table 5.2b – Data regarding physico-chemical features of the tested ENM.

	n-ZnO NM-110	**n-ZnO NM-111**	**n-Ag NM-300 (density: 10.49 g/cm^3)**	**n-Ag 47MN-03**	**MWCNT NM-400**	**MWCNT NM-402**
Coating*	-	triethoxy-caprylylsilane 130	4% Polyoxyethylene glycerol trioleate; 4% Tween 20	-	Pyrogenic carbon	Pyrogenic carbon
Primary size declared (measured)[1] (nm)	20-350	10-450	< 20 (18±4)	40-90 (61±20)	Ø: 5-35 nm (~80%: 10-15 nm) L: 0.7-3 µm (80%)	Ø: 6-20 nm (80%) L: 0.7-4 µm (80%)
Crystallite size[2] (nm)	71	58	4	-	-	-
Shape[1]	Polyhedral particles, some irregular, varied morphology	Polyhedral particles, some irregular, varied morphology	Individual (dispersed) idiomorphic crystallites	Irregular elongated polyhedrons; spherical particles with rounded and smooth edges	Bent multiwalled	Bent and partially entangled multiwalled
Crystalline phases (%)[2]	Zincite:Am 52:48	Zincite:Am 34:66	Ag_m	100 Ag	-	-
Specific surface area[3] (m^2/g)	14 (±0.1)	18 (±0.1)	-	3.8±0.1	298 (±1)	225 (±1)
Pore Volume[3] (ml/g)	0.1	0.1	-	-	1.4	1.2
Inorganic Impurities of concern (ug/g)[4]	-	-	Fe (28±5) Zn (20±13) As (5±1)	-	Al (49370±650) Fe (3570±130) Co (2080±60)	Al (32190±7130) Fe (17140±1110) Co (18±1)

Detected by [1] TEM; [2] XRD; [3] BET; [4] ICP-OES / ICP-MS

*Data from supplier

Among all n-TiO_2 samples studied, as previously mentioned in paragraph 4.2, NRCWE-001 was functionalized with two different chemical groups to obtain NRCWE-002 and NRCWE-003. Thus, their physico-chemical characteristics were almost the same, except for specific surface area, slightly lower (84 instead of 99 m^2/g) exhibited by the two-coated samples. By TEM analyses, particles shape of the whole set of n-TiO_2 samples was mainly characterized by irregular polyhedrons together with some spherical particles. NRCWE-004 displayed the largest average crystallite size (i.e. 94 nm) and size distribution (1-2000 nm). As far the crystalline phases, rutile was the predominant phase (between 62 and 75%) for NRCWE-001 and for the two modified samples, while P25 showed 86% of anatase and 13.5% rutile. NRWCE-004 and NM-101 were mainly constituted by two phases: 44% rutile and 56% amorphous and 48% anatase and 51% amorphous phase, respectively. The specific surface area, calculated by BET, indicated the highest value (322±2 m^2/g) for NM-101, compared to the lowest observed for P25 (54±0.2 m^2/g) and NRCWE-004 (5.1±0.5 m^2/g). The n-TiO_2 inorganic impurities of concern were mostly Fe and Co, except for NRCWE-003 (Fe only) and P25 (Mg only).

As far the two n-ZnO samples, they differed for several characteristics: (i) coating (pristine NM-110 instead of the triethoxycaprilsilane coating for NM-111); (ii) crystallite size, larger for NM-110 (71 nm instead of 58 nm) but with a narrower size distribution compared to NM-111 (20-350 nm and 10-450 nm, respectively); (iii) crystalline phases (52% zincite and 48% amorphous for NM-110 compared to 34% zincite and 66% amorphous for NM-111). On the other hand, particle morphology, specific surface area, pore volume as well as inorganic impurities were practically the same.

The comparison of the main physico-chemical characteristics between the two n-Ag samples is not suitable because of the composition state (NM-300 was a dispersion, with 10.49 g/cm^3 density as well as 4% polyoxyethylene glycerol trioleate and 4% tween 20 as stabilizers, while 47MN-03 was an n-Ag powder). NM-300 showed a crystallite size of 4 nm, and a size distribution in the range of 14-22 nm, with individual idiomorphic crystallites due to the presence of stabilizers. The inorganic impurities of concern were mainly Fe, Zn and As. TEM analysis of n-Ag powder sample showed a slightly difference between the size distribution declared (40-90 nm)

and that measured (41-81 nm). Particles were both irregular elongated polyhedrons and spherical with rounded edges and showed a specific surface area of 3.8±0.1 m^2/g. The absence of inorganic impurities was confirmed by ICP-MS analyses.

Finally, two types of MWCNT were characterized: NM 400 had larger diameter (5-35 nm vs. 6-20 nm) and shorter length (0.7-3 μm vs. 0.7-4 μm) compared to NM-402. By TEM analysis, the samples appeared as bent multiwalled, with large agglomerates, in particularly observed for NM-402. NM-400 specific surface area was larger (298±1 m^2/g) than that of NM-402 (225±1 m^2/g), with similar pore volume (1.4 and 1.2 ml/g, respectively). NM-400 showed Fe, Co and Zn as inorganic impurities of concern, instead of Fe only, detected in NM-402.

5.2 Secondary characterization

The results obtained from ENP interaction with biological media are presented as follows: firstly, the biological media composition, the handling of ENP samples, the preparation of stock dispersions (step 1) for *in vitro* and *in vivo* bioassays as well as the development of ENP dispersion protocols (steps 2a-b) are reported. According to the obtained results, stability data of ENM, dispersed in biological media, are presented. Furthermore, on the basis of ENM inorganic impurities detected (see Table 5.2a and b), the development of a general analytical protocol, for ENM determination in biological samples was developed. Specific operating conditions are reported in Table 5.5. Extraction efficiency and biodistribution results of inorganic elements, selected as tracers of the ENM presence in a secondary target organ (i.e. mice brain), are displayed, according to the analytical protocol developed.

As far the secondary characterization oriented to assess dose-response relationship of n-TiO_2 P25, the characterization of aqueous solutions, toghether with agglomeration data and sedimentation profiles of n-TiO_2 P25 over time are shown.

Biological media composition

DMEM (D6041) is mainly composed by low-glucose amount (1000 mg/l), inorganic salts, such as NaCl (6400 mg/l) and $NaHCO_3$ (3700 mg/l), amino acids (30-500 mg/l), vitamins (4-7 mg/l) and other components (<0.1 mg/l). In order to improve the stability of the medium, pyridoxal, usually used in the original DMEM-Hi formulation, has been replaced by pyridoxine.

DMEM-F12-HAM (D6421) is a 50:50 mixture of DMEM and Ham's F12 media that has proven to be useful in a wide range of cell culture applications, especially when supplemented with FBS. It is mostly made up by glucose (3000 mg/l), an Hepes buffer solution (3600 mg/l), inorganic salts, such as NaCl (7000 mg/l) and $NaHCO_3$ (1200 mg/l), amino acids (4-500 mg/l), vitamins (2-13 mg/l) and other components (<0.1 mg/l).

RPMI-1640 (R8758) medium includes glucose (2000 mg/l), inorganic salts, such as NaCl (6000 mg/l) and $NaHCO_3$ (2000 mg/l), amino acids (20-300 mg/l), vitamins (0.2-35 mg/l) and other components (<0.1 mg/l).

Hemoglobin (≤20 mg/dl), hormones, growth factors and carrier proteins of the blood are the main components of FBS (F9665). The impurities declared are ≤10 endotoxin unit (EU)/ml. Because endotoxin molecular weight can range in a wide interval (10000-1000000 Da), endotoxin levels are measured in "endotoxin units" (EU). One EU is approximately equivalent to 100 pg of E. Coli lipopolysaccharide—the amount present in around 10^5 bacteria. Humans can develop symptoms when exposed to as little as 5 EU/kg body weight.

Dispersion protocols in the tested biological media

Handling of vials:

All ENP have been distributed in vials under argon and should be stored dried at RT in the dark. Except for n-Ag NM-300, all ENP can be repeatedly used for a maximum of one week from the first opening of the vial, according to ENPRA project partners. Since some vials containing NM-300 dispersion showed sediments and/or silver-like material floating on the surface, carefully check for any residual material on the bottom before opening and follow the specific protocol designed for handling NM-300 dispersion. Only in the case of reuse of NM-300 dispersion, its container has to be sealed under argon to maintain sample purity. After opening a vial, it is recommended to work as fast as possible.

Step 1 - Stock dispersion:

Firstly, ENP stock dispersions were prepared (final concentration 2.56 mg ENP/ml) as follows:

- weigh 5.12 mg of powder ENP with Sartorius analytical microbalance in a tin sample holder and gently place it into 4 ml vial;
- add 2 ml MilliQ and 2% vol FBS, used as stabilizer;
- sonicate the obtained stock dispersion with a probe sonicator (not bath) for at least 10 min at 100W. Be careful to cool the flask during sonication with water and ice in order not to increase the dispersion temperature, and not let the probe tip to touch the flask inner walls.

For n-ZnO NM-111 only, because of the coating, wet the sample with 0.5 vol.% EtOH before sonication to achieve a good dispersion in the medium.

Step 2a - Dispersion protocols for ENP (except for n-Ag NM-300):

Therefore, each stock dispersion was separately added to DMEM (D6041) plus 10% vol FBS, DMEM-HAM-F12 (D6421) plus 2% vol FBS and RPMI-1640 (R8758), following the optimized procedure below (final concentration of 0.256 mg ENP/ml, according to ENPRA project partners):

1. Withdraw 1 ml stock dispersion and add it to 9 ml biological medium;
2. sonicate the resulting dispersion with a probe sonicator (not bath) for 15 min at 100 Watt. Be careful to cool the flask during sonication with water and ice in order not to increase the dispersion temperature, and not let the probe tip to touch the flask inner walls;
3. Check if the resulting dispersion will be stable over time, almost for DLS measurements. If not, repeat the preparation procedure.

Step 2b - Dispersion protocol for n-Ag NM-300:

The n-Ag NM-300 vial contains 0.5 g silver to 5 ml de-ionised water (75%) with stabilizing agent 7% ammonium nitrate and 8% emulsifiers (4% each of Polyoxyethylene Glycerol Trioleate and Polyoxyethylene(20) Sorbitan mono-Laurat (Tween 20). The material is very viscous (density: 1.1±0.03 g/ml), and weighing is therefore recommended for dilution. For dilution use at least 25 ml dispersion medium, considering that 1 ml NM-300 to 38.0625 ml dispersion medium will give a concentration of 2.56 mg/ml. The dispersion preparation was as follows:

1. withdraw 0.1 ml NM-300 and add to 3.806 ml of MilliQ plus 2% vol FBS, to obtain the n-Ag NM-300 stock dispersion (final concentration: 2.56 mg/ml);
2. withdraw 1 ml stock dispersion and add it to 9 ml biological medium;
3. sonicate the resulting dispersion with a probe sonicator for 15 min at 100 Watt. Be careful to cool the flask during sonication with water and ice in order not to increase the dispersion temperature, and not let the probe tip to touch the flask inner walls;
4. check if the resulting dispersion will be stable over time, almost for DLS measurements. If not, repeat the preparation procedure.

Stability of ENP in biological media

Figure 5.3 shows the typical size distribution of NRCWE-001 dispersed in F12+2% vol FBS, after the probe sonication, carried out by DLS. In order to increase readability, all size distribution data about other ENP dispersed in the selected biological media are summarized in Table 5.3. Sedimentation rate, expressed as % of demixing (i.e. the separation of components in dispersion), calculated simulating 24 h of real sedimentation by means of analytical centrifuge, is presented for all ENP through Figures 4.4-4.12. Table 5.4 summarises the % of demixing for the whole set of ENP investigated, achieved by analytical centrifugation, simulating 24 h of real sedimentation. The demixing of NM300 in all biological media resulted to be <1% due to the presence of stabilizers, thus it was not reported as graph.

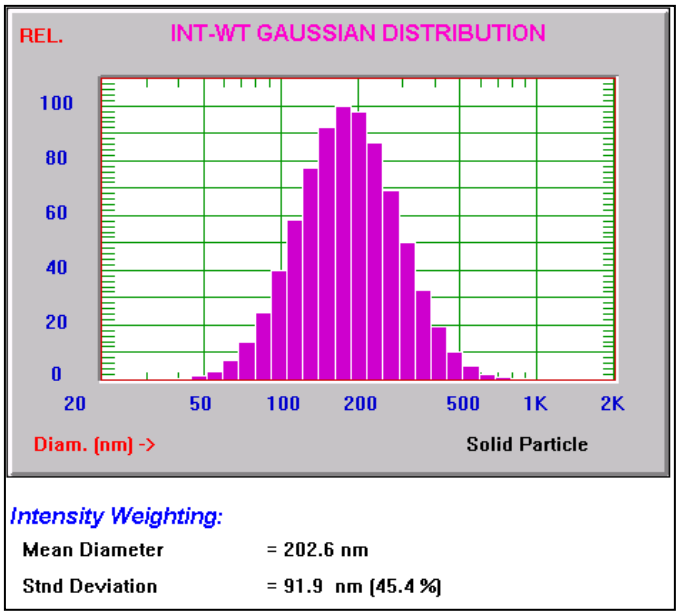

Figure 5.3 – Gaussian distribution of n-TiO_2 NRCWE-001 sample, when dispersed in DMEM-F12-HAM, immediately after probe sonication.

Table 5.3 – Size distribution of ENP (2.56 mg/ml), dispersed in the selected biological media, immediately after probe sonication.

ENP	Size distribution (average ± std dev, nm) in biological medium		
	DMEM+10 vol% FBS	**F12+2 vol% FBS**	**RPMI**
n-TiO_2 NRCWE-001	203 ± 92	202 ± 92	1338 ± 819
n-TiO_2 NRCWE-002	287 ± 174	258 ± 152	2149 ± 1426
n-TiO_2 NRCWE-003	936 ± 653	1112 ± 660	1022 ± 690
n-TiO_2 NRCWE-004	339 ± 184	389 ± 249	465 ± 322
n-TiO_2 NM-101	597 ± 288	544 ± 306	532 ± 256
n-TiO_2 P25	258 ± 101	302 ± 173	567 ± 298
n-ZnO NM-110	306 ± 127	313 ± 116	313 ± 105
n-ZnO NM-111	313 ± 118	315 ± 108	310 ± 103
n-Ag NM-300	97 ± 52	97 ± 51	95 ± 50
n-Ag 47MN-03	89 ± 33	101 ± 41	443 ± 178

Table 5.3 indicated significant different size distributions, and thus agglomeration, among all ENP dispersed in the selected biological samples. NRCWE-003, NM-101, NM-110 and NM-111 presented stable size distributions regardless of the medium and the amount of FBS added. NRCWE-004 and P25 showed a general wider size distribution, increasing by a factor of 0.8 and 2, respectively, moving from the more stable biological media, which means relatively constant average size distribution over time (i.e. DMEM+10 vol% FBS and F12+2 vol% FBS), to the medium without any stabilizer addition (i.e. RPMI). An even greater increase of agglomerates size measured in RPMI medium is underlined by high values recorded for NRCWE-001 (2149±1426 nm), NRCWE-002 (1138±819 nm) and 47MN-03 (443±178 nm).

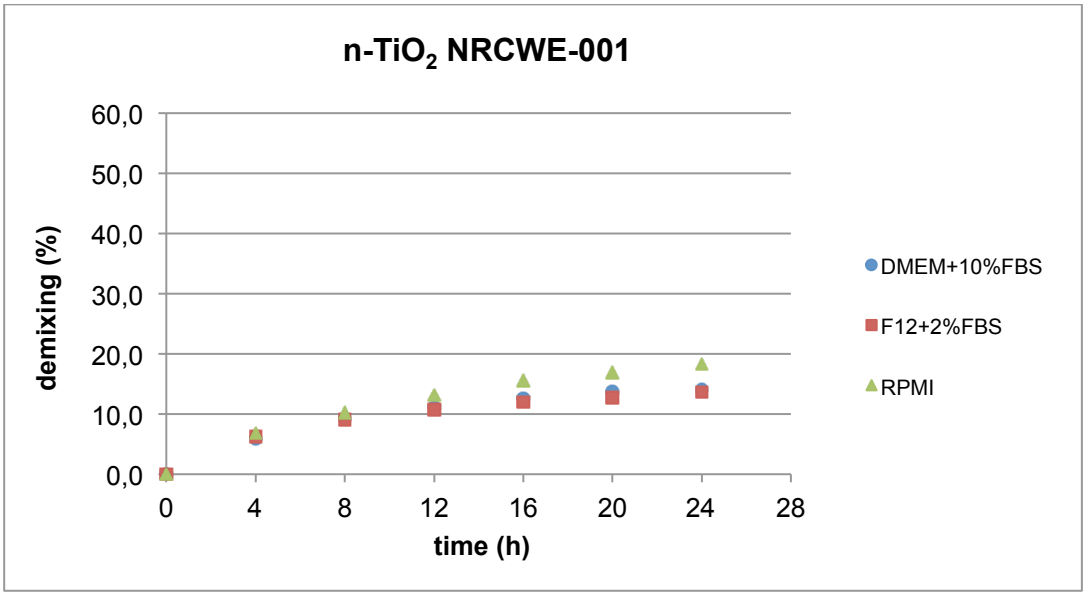

Figure 5.4 - Demixing of n-TiO_2 NRCWE-001 sample in the selected biological media.

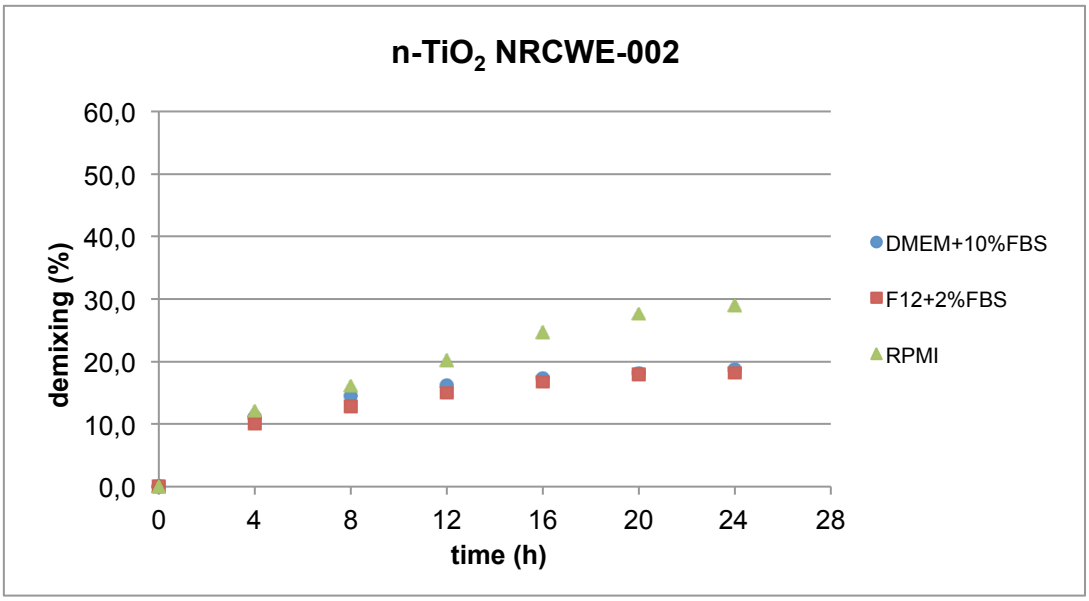

Figure 5.5 - Demixing of NRCWE-002 sample in the selected biological media.

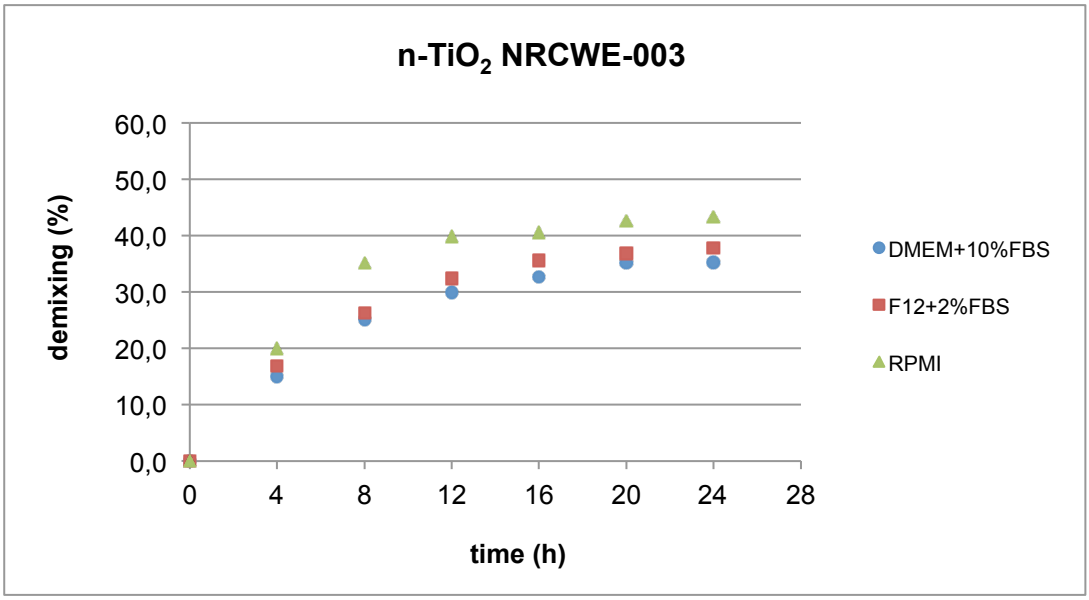

Figure 5.6 - Demixing of n-TiO_2 NRCWE-003 sample in the selected biological media.

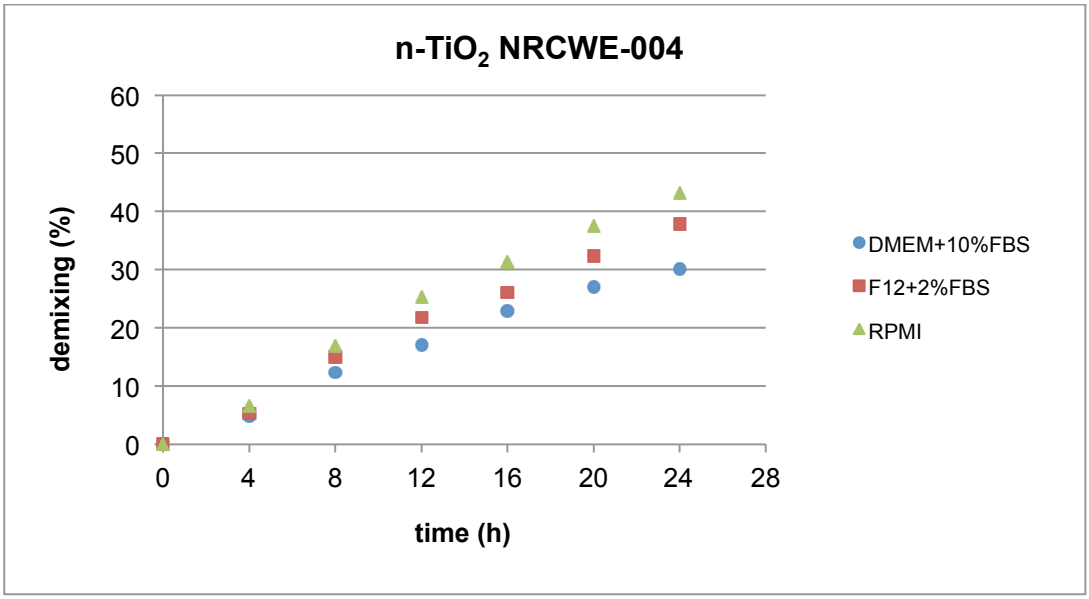

Figure 5.7 - Demixing of n-TiO_2 NRCWE-004 sample in the selected biological media.

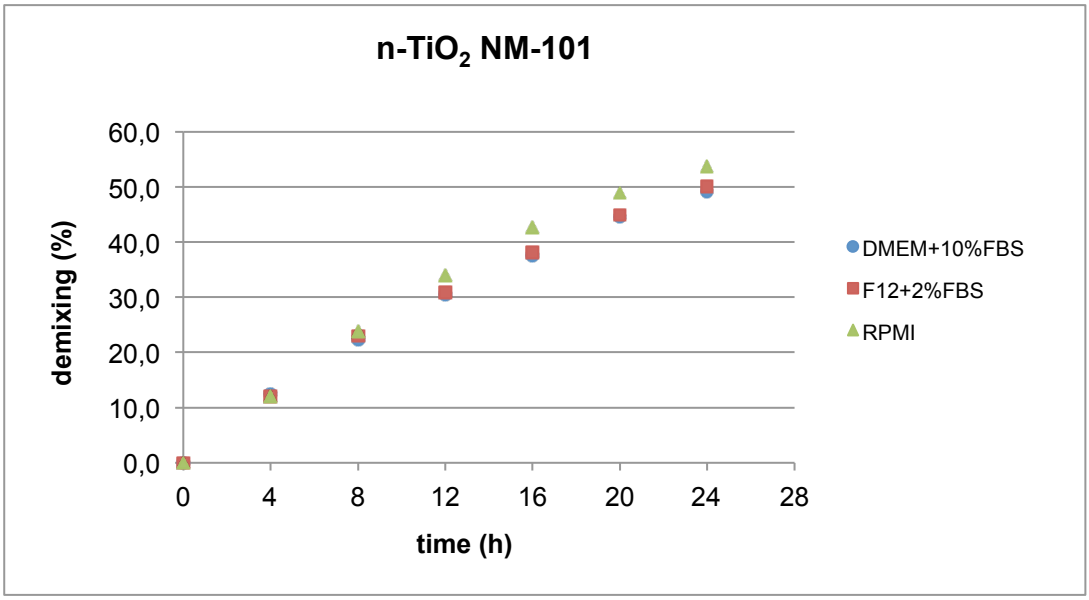

Figure 5.8 - Demixing of n-TiO_2 NM-101 sample in the selected biological media.

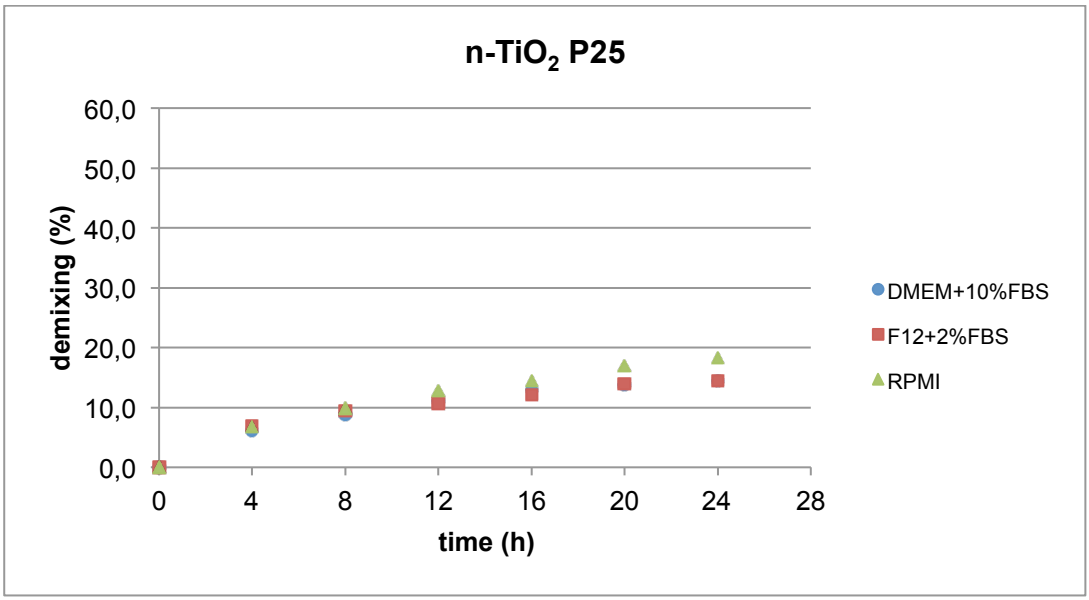

Figure 5.9 - Demixing of n-TiO_2 P25 sample in the selected biological media.

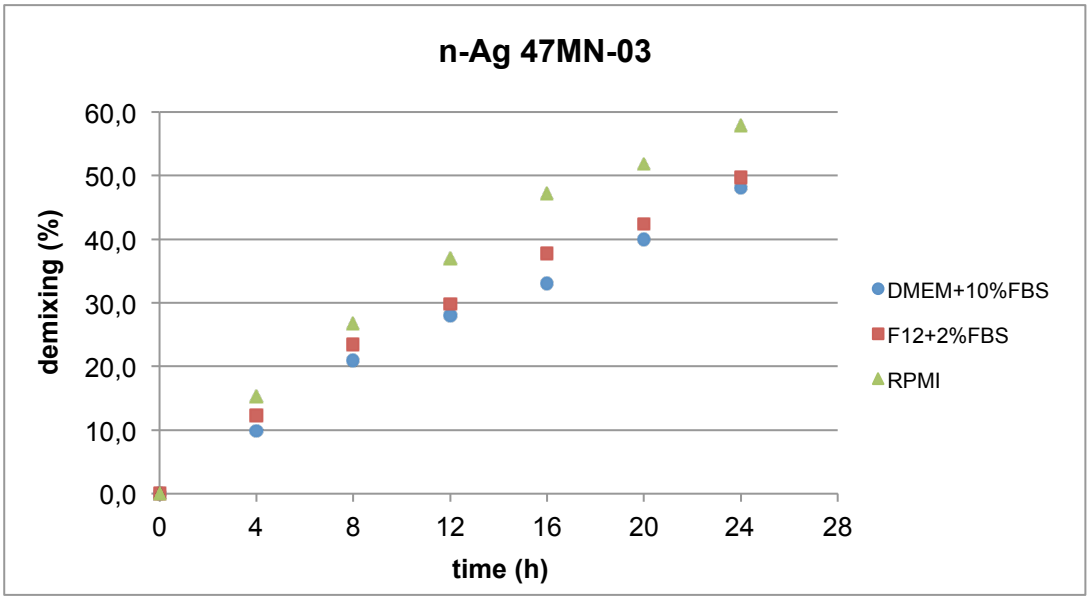

Figure 5.10 - Demixing of n-Ag 47MN-03 sample in the selected biological media.

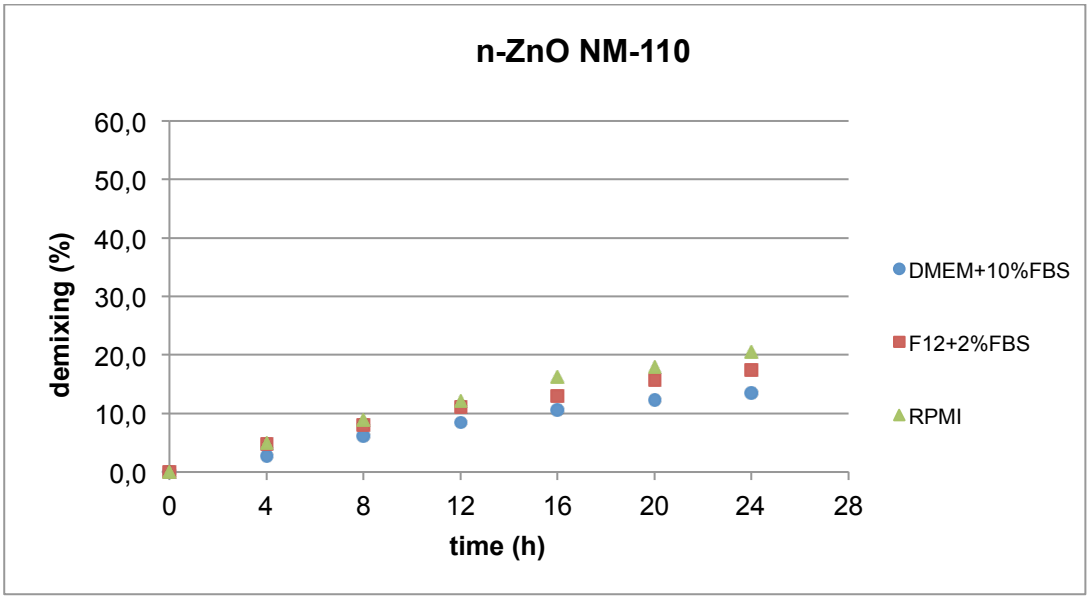

Figure 5.11 - Demixing of n-ZnO NM-110 sample in the selected biological media.

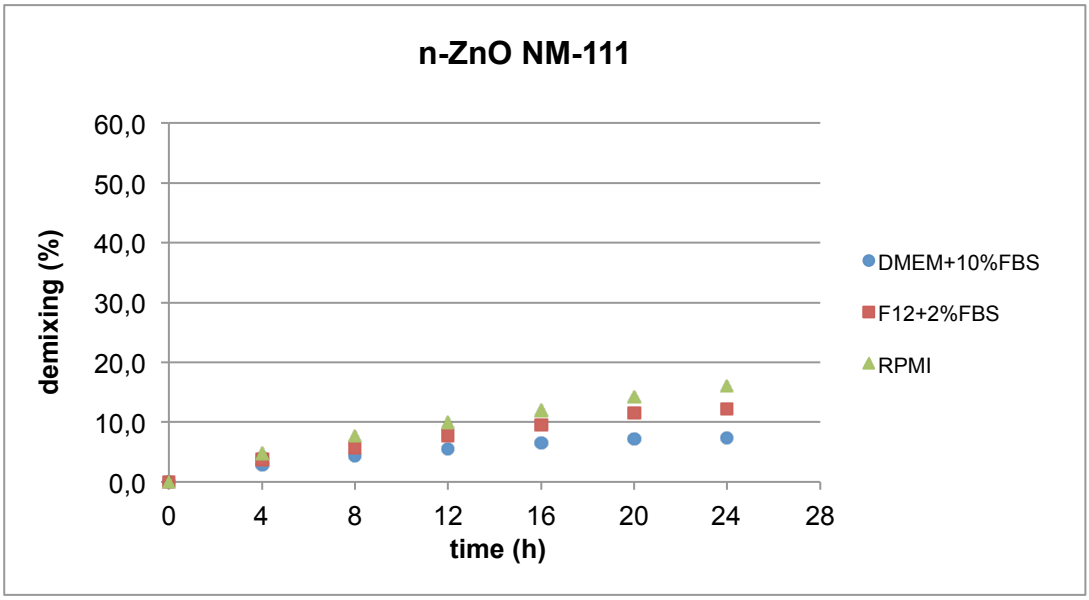

Figure 5.12 - Demixing of n-ZnO NM-111 sample in the selected biological media.

Table 5.4 - Percentage of demixing after analytical centrifugation simulating 24 h of real sedimentation, for all the ENP dispersed in the three biological media selected. The n-Ag NM-300 dispersion was not included because of its intrinsic stability over time.

ENP samples / biological media	DMEM+10%FBS	F12+2%FBS	RPMI
n-TiO_2 NRCWE-001	14.1	13.6	18.3
n-TiO_2 NRCWE-002	18.8	18.3	29.0
n-TiO_2 NRCWE-003	35.3	37.9	43.4
n-TiO_2 NRCWE-004	30.1	37.8	43.2
n-TiO_2 NM-101	49.1	50.1	53.7
n-TiO_2 P25	14.5	14.4	18.3
n-Ag 47MN-03	48	49.7	57.9
n-ZnO NM-110	7.4	12.2	16.0
n-ZnO NM-111	13.5	17.4	20.5

ENM biodistribution in a secondary target organ

Analytical protocol

Important note: Development of all methods was made by using an Ethos MLS-1200 Mega (Milestone, Sorisole**,** Italy) microwave oven and an Agilent (Tokyo, Japan) 7700x ICP-MS. The use of different microwave oven and ICP instrumentations than those used here has not been performed, thus results cannot be guaranteed. Further optimization of tests conditions is strongly suggested for other instrumentations.

- 400 mg of dry biological sample, from toxicological testing, and approx. 20 µg of powder ENM were placed into a sealed Teflon-lined reaction vessel, together with an acid mixture specific for each ENM, and then inserted into the rotor of the microwave oven. Each sample was digested by a tailored microwave-assisted digestion method, selecting the digestion temperature and time as a function of each ENM.
- The obtained acid solution, after cooling, was transferred into a teflon flask and diluted to 25 ml with MilliQ.
- The resulting solution was stored in a teflon bottle for subsequent analysis by ICP-MS.

Table 5.5 – Specific acid mixture, digestion temperature and time of each ENM tested. The microwave digestion is characterized by three steps (Figure 5.13): (i) increase of T to the set value selected over the first time-interval; (ii) kept T constant over the second time-interval; (iii) cooling phase over the third time-interval.

ENM	Acid mixture	Digestion T and time
n-TiO_2	HNO_3 (8 ml)	(i) 220°C for 10 min (ii) 220°C for 10 min
n-ZnO	HNO_3 (8 ml)	(i) 220°C for 10 min (ii) 220°C for 10 min
n-Ag	HCl (7 ml) HNO_3 (2.5 ml)	(i) 220°C for 10 min (ii) 220°C for 30 min
MWCNT	HNO_3 (10 ml)	(i) 220°C for 15 min (ii) 220°C for 45 min

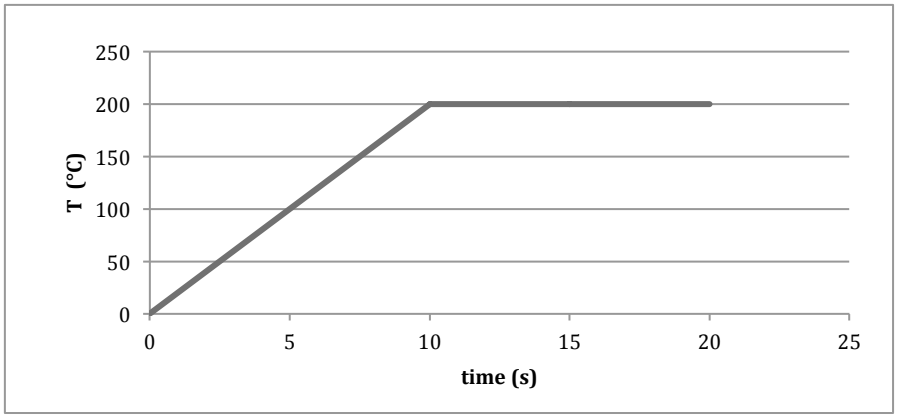

Figure 5.13 – A typical microwave digestion program used for n-TiO_2 samples.

ENM extraction efficiency

Figure 5.14 shows different average % of ENM extraction efficiency, depending on sample tested and acid mixture employed. Limit of detection (LOD) obtained for each element of concern were: 0.7 ng/g for Ti, 1.1 ng/g for Zn, 0.8 ng/g for Ag, 0.9 ng/g for Al and 0.1 ng/g for Co. Extraction efficiency of 81±38% Ti (47% RSD) and 84±43% Zn (51% RSD) were obtained from samples administrated with n-TiO_2 NM-101 and n-ZnO NM-110, respectively, while the extraction efficiency of Ag was slightly above the initial amount added (104±23%, with 22% RSD). With regard to MWCNT, after determination of their inorganic impurities performed within the primary characterization, Al and Co for NM-400 and Al only for NM-402 were selected as tracers of MWCNT in the investigated biological samples. Extraction efficiency of 90±20% Al and 92±20% Co (22% RSD for both) for NM-400 and 72±9% Al (12.5% RSD) for NM-402 were obtained.

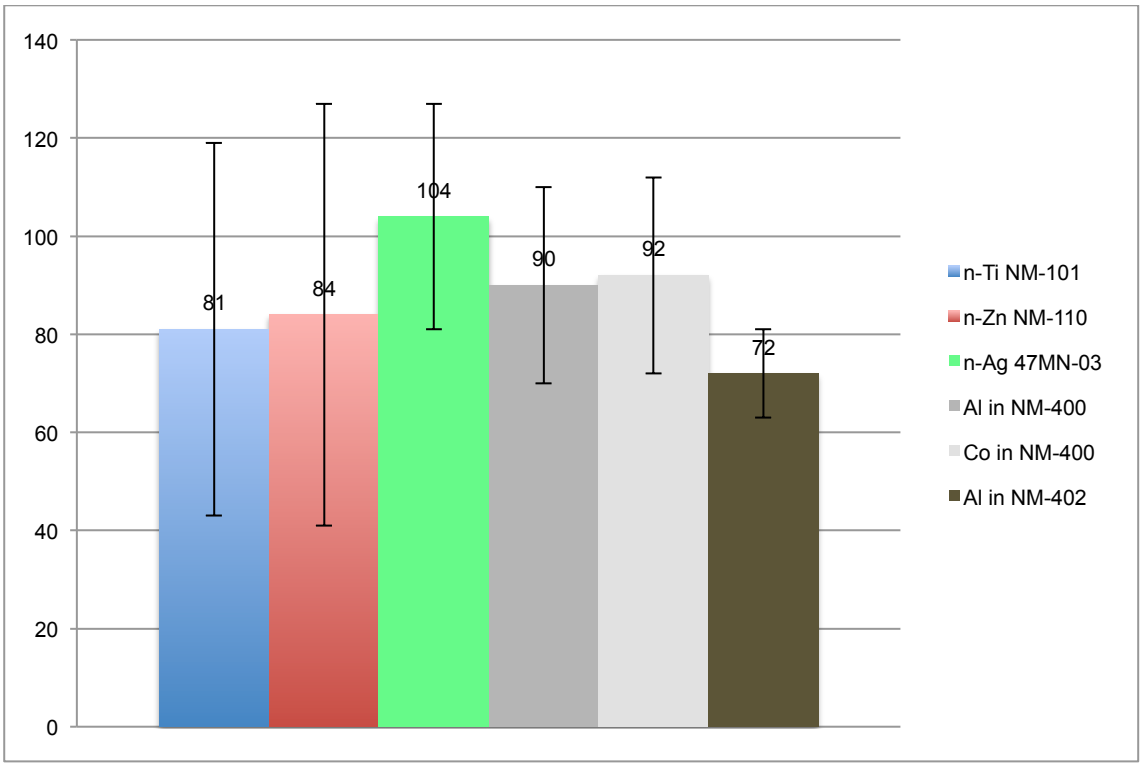

Figure 5.14 - Average % of extraction efficiency for ENM and their inorganic tracers, added to dry biological samples analyzed by Agilent 7700x ICP-MS (115 samples: 28 of n-TiO_2 NM-101, 24 each of n-ZnO NM-110 and n-Ag 47MN-03; 20 of MWCNT NM-400 and 19 of MWCNT NM-402).

ENM quantification after toxicological testing

According to analytical protocols developed and taking into account the toxicological experiments performed by ENPRA project partners by intratracheally instillation of ENM to mice at different concentrations (i.e. 1, 4, 8, 16, 32, 64 and 128 ug ENM/animal), the overall ICP-MS data regarding the ENM quantification in mice brains (received as powder form) are summarized in Table 5.6. Figures 5.15 and 5.16 display the values obtained from samples instilled with the whole set of tested n-TiO_2 and MWCNT. Data from biological samples to which was administered n-ZnO (i.e. NM-110 and NM-111) and n-Ag NM-300 are not reported, since they were below the limit of detection (LOD). The overall results (total number of samples: 240, 24 samples for each ENM) are expressed as the average of three samples at the same initial ENM concentration used for toxicological testing. Since some data presented a wide range of standard deviation (Table 5.6), which would make the values below 0 without a physical meaning, figures 5.15 and 5.16 show only the positive error bars for those samples.

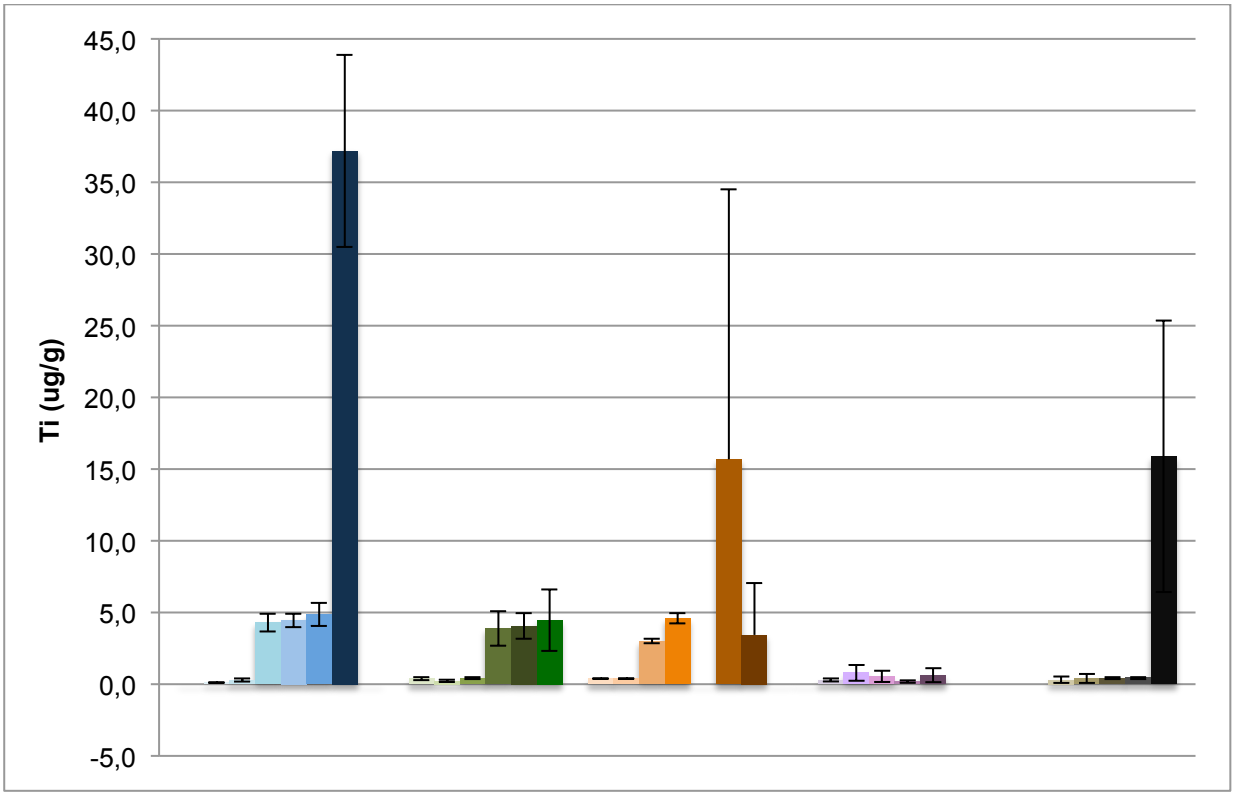

Figure 5.15 – Ti concentrations (ug/g) detected for 24 samples for each ENM, which individually received (from left to right) NRCWE-001, NRCWE-002, NRCWE-003,

NRCWE-004 and NM-101 by intratracheally instillation, at different tested concentrations (from left to right: 4, 8, 16, 32, 64 and 128 ug/animal displayed for NRCWE-001 and NRCWE-002; 1, 4, 8, 16, 64 and 128 ug/animal displayed for NRCWE-003; 4, 8, 16, 32 and 64 ug/animal displayed for NRCWE-004 and 8, 16, 32, 64 and 128 ug/animal displayed for NM-101). The values <LOD are not reported.

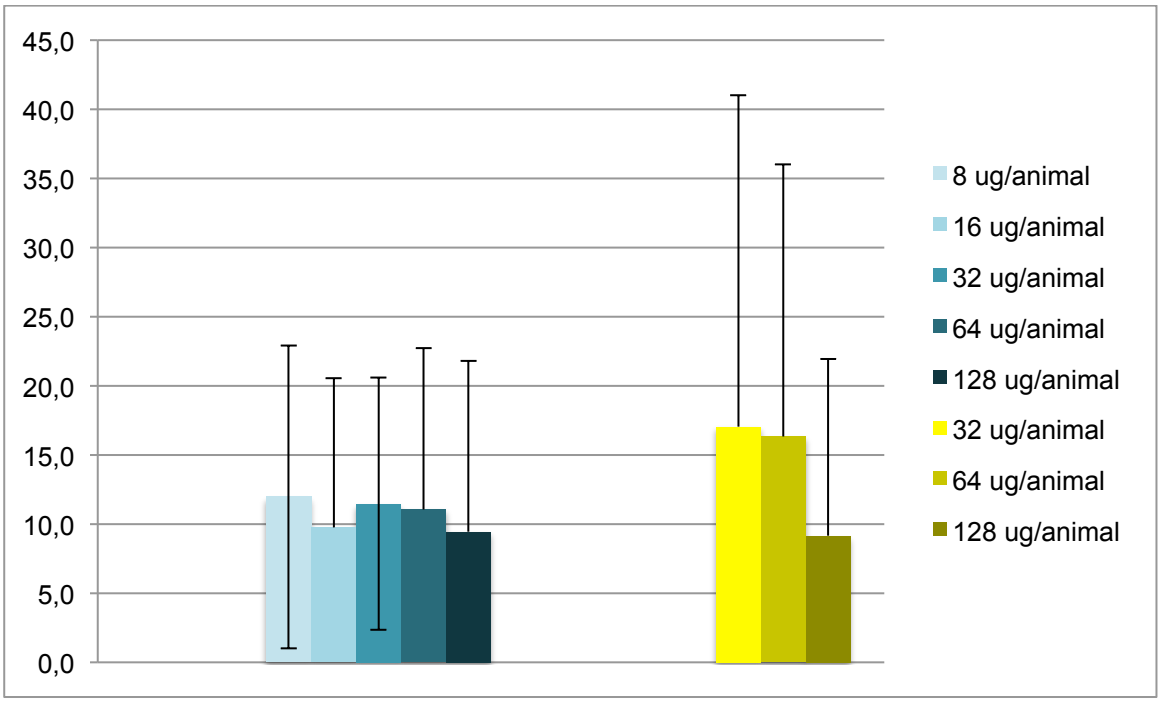

Figure 5.16 – Al concentrations (ug/g) detected for 24 samples for each ENM, which individually received NM-400 (on the left) and NM-402 (on the right) by intratracheally instillation, at different tested concentrations (i.e., from left to right, 8, 16, 32, 64 and 128 ug ENM/animal for NM-400 and 32, 64 and 128 ug ENM/animal for NM-402).

Table 5.6 – Concentrations of Ti (ug/g) in samples (240 in total) treated with 5 different n-TiO_2 (the NRCWE series plus NM-101) and Al in samples instilled with both MWCNT NM-400 and NM-402, detected by ICP-MS, according to analytical protocols developed at pag. 72. Data from biological samples administered with both n-ZnO NM-110 and NM-111 and n-Ag NM-300 are not reported because both Zn and Ag were below Limit Of Detection (LOD). Moreover, also Co searched in samples treated by NM-400 was <LOD.

	NRCWE-001 avg ± st dev	**NRCWE-002 avg ± st dev**	**NRCWE-003 avg ± st dev**	**NRCWE-004 avg ± st dev**	**NM-101 avg ± st dev**	**Al from NM-400 instillation avg ± st dev**	**Al from NM-402 instillation avg ± st dev**
control	< LOD	< LOD	< LOD	< LOD	< LOD	< LOD	< LOD
1 ug/animal	< LOD	< LOD	0.4±0.01	< LOD	< LOD	< LOD	< LOD
4 ug/animal	0.1±0.03	0.4±0.1	0.4±0.01	0.3±0.1	< LOD	< LOD	< LOD
8 ug/animal	0.3±0.1	0.3±0.08	3±0.2	0.8±0.6	0.3±0.2	12±11	< LOD
16 ug/animal	4.3±0.6	0.4±0.07	4.6±0.4	0.5±0.4	0.4±0.3	9.8±10.8	< LOD
32 ug/animal	4.5±0.5	3.9±1.2	< LOD	0.2±0.1	0.4±0.1	11.5±9.1	17±24
64 ug/animal	4.9±0.8	4.1±0.9	15.7±18.8	0.6±0.5	0.4±0.1	11.1±11.7	16.3±19.7
128 ug/animal	37.2±6.7	4.5±2.2	3.5±3.6	< LOD	15.9±9.5	9.5±12.4	9.2±12.8

ENM extraction efficiency data underlined that Ag values from mices administrated with n-Ag were the highest (104±23%). Comparing Al amounts from the two MWCNT samples (Figure 5.14), lower extraction efficiency of NM-402 was found likely because of the lower level of Al impurity (32 mg/g for NM-402 instead of 51 mg/g for NM-400).

As far the ENM quantification after toxicological testing, as reported in Table 5.6 and in Figure 5.15, among all the samples treated with n-TiO_2, all the controls (i.e. no ENM instilled) and the 1 ug ENM/animal initial concentration did not shown Ti, except for NRCWE-003, with 0.4±0.01 ug/g at 1 ug ENM/animal initial concentration. Increasing initial concentration to 4 and 8 ug ENM/animal, values showed a concentration range between 0.1±0.03 and 3±0.2 ug/g (for NRCWE-001 and NRCWE-003, respectively), representing the $4 \cdot 10^{-7}$% and $3 \cdot 10^{-5}$% initial concentrations. Taking into account the 16 ug ENM/animal initial concentration, NRCWE-001 and NRCWE-003 exhibited the highest amount of Ti (i.e. $7 \cdot 10^{-5}$% initial concentration), while the concentration range of other samples administered with n-TiO_2 was extremely low

(from 0.4±0.07 to 0.5±0.4 ug/g, equal to $6 \cdot 10^{-6}$ and $8 \cdot 10^{-6}$% initial concentration). As far 32 ug ENM/animal initial concentration, the highest concentrations were recorded for NRCWE-001 and NRCWE-002 (i.e. $1 \cdot 10^{-4}$% of the dose), instead of very low Ti amounts for the other samples in which n-TiO_2 was added (i.e. 0.2±0.1 ug/g for NRCWE-004, 0.4±0.1 ug/g for NM-101 and <LOD for NRCWE-003). Increasing initial concentration to 64 ug ENM/animal, NRCWE-003 showed the greatest growth of Ti amount but with a wide range of values included (i.e. 29 ug/g, 2 ug/g and <LOD), giving 15.7±18.8 ug/g as the average of the three samples. Moreover, Ti concentration in samples treated with NRCWE-004 increased by an order of magnitude (from $6 \cdot 10^{-6}$ to $4 \cdot 10^{-5}$% of the dose), compared to the experiments carried out at 32 ug ENM/initial concentration, while Ti concentrations in samples that received NRCWE-001, NRCWE-002 and NM-101 were almost the same as the previous concentrations recorded. Finally, the highest initial concentration tested (i.e. 128 ug ENM/animal), the highest Ti values recorded for NRCWE-001 (i.e. 37.2±6.7 ug/g, representing $5 \cdot 10^{-3}$% initial concentration), NRCWE-002 (i.e. 4.5±2.2 ug/g, representing $6 \cdot 10^{-4}$% of the initial concentration) and NM-101 (i.e. 15.9±9.5 ug/g, equal to $2 \cdot 10^{-3}$% of the dose). Despite this, NRCWE-003 showed a significantly decrease of Ti amount measured (i.e. 3.5±3.6 ug/g, equal to $4 \cdot 10^{-4}$% of the initial concentration), compared to those observed for lower initial concentrations, whereas Ti was <LOD in samples which received NRCWE-004.

As far as MWCNT samples are concerned, both Al and Co for NM-400 and Al only for NM-402, according to primary characterization results, the analytical protocols developed as well as their low values in biota (i.e. order of ug/g), were selected as tracers of the MWCNT presence in biological samples. According to this, Figure 5.16 shows that Al was the only element detected by ICP-MS. Furthermore, Al was <LOD for samples treated with NM-400 at 0, 1 and 4 ug ENM/animal (see Table 5.6), and for samples administered with NM-402 up to 16 ug ENM/animal. Moving from the lowest concentrations tested (i.e. 8 ug ENM/animal initial concentration for NM-400 and 32 ug ENM/animal initial concentration for NM-402) to 64 ug ENM/animal instilled, both samples showed an increase of Al concentration, by one order of magnitude (i.e. from 10^{-4}% to 10^{-3}% of the dose). A sligthly decrease of Al concentration was observed at the highest concentration tested, resulting in 9.5±12.4 ug/g and 9.2±12.8 ug/g in NM-

400 and NM-402, respectively. It was also observed that the values of the standard deviations calculated for these samples were greater compared to those of Ti from n-TiO_2 samples.

Secondary characterization in water media

Characterization of aqueous solutions

Table 4.2 shows the ionic composition, pH, dissolved organic carbon (DOC), conductance, salinity, ionic strength (IS) and divalent cation concentration of the aqueous solutions before dispersing the n-TiO_2 P25 powder. Sodium bicarbonate, a naturally occurring buffer commonly added to culture media for toxicological studies, was added to all artificial solutions in order to ensure the pH stability in the 8.0–8.2 range. DOC was negligible (<0.2 mM) in all artificial samples, thus preventing stabilization of the dispersed P25 by interaction with organic matter. Ionic composition, IS, specific conductance, and divalent cation concentration were already reported to greatly affect n-TiO_2 stability in solution (French et al., 2009). These parameters varied widely in the prepared dispersions and can be regarded as the key variables affecting P25 behavior under the tested physico-chemical conditions. The artificial estuarine-like sample, AEW, exhibited values of most parameters very similar to those of the artificial freshwater, AFW.

Agglomeration and sedimentation of n-TiO_2 P25 in aqueous dispersions

As far P25 dispersed in synthetic and real sea and estuarine-like water samples, Table 5.7 shows DLS agglomeration data, recorded at selected concentrations (0.1, 1 and 10 mg/l) and times (0.2, 25 and 50 h). Moreover, Figures 5.17-5.19 display the sedimentation profiles of three representative samples, i.e. the synthetic freshwater sample (AFW), one synthetic seawater sample (ASW1) and the real seawater sample (SW), by plotting $\ln(C/C_0)$ versus time. The sedimentation profiles of all other tested aqueous dispersions, for each P25 concentration tested, are provided in Annex 2.

The sedimentation rates were calculated according to a first-order decay equation (Eq. 14), applied to fit the obtained sedimentation profiles (Brunelli et al., 2013).

Considering the first-order linear equation below:

$$\frac{dC}{dt} = -kC \qquad \text{(Eq. 9)}$$

where C is concentration at time t and k is first order rate constant, Eq. 9 was analytically integrated as follow:

$$\frac{dC}{C} = kdt \qquad \text{(Eq. 10)}$$

$$\ln C = kt + p \qquad \text{(Eq. 11)}$$

where p is a constant.

By introducing the initial condition $C(t_0)=C_0$ and setting $t_0=0$, it resulted:

$$\ln \frac{C}{C_0} = -kt \qquad \text{(Eq. 12)}$$

$$\ln C = \ln C_0 - kt \qquad \text{(Eq. 13)}$$

$$C = C_0 e^{-kt} \qquad \text{(Eq. 14)}$$

From Eq. 12, the first order rate constant (k) was calculated as follow:

$$k = -\frac{\ln\left(\frac{C}{C_0}\right)}{t} \qquad \text{(Eq. 15).}$$

The overall sedimentation profiles fitted well with a first-order kinetic (Eq. 14), and the rate constant k (i.e. the slope of the graph), for each dispersion, was calculated according to Eq. 15. The k values and the correlation coefficients (R^2) are summarized in Table 5.8. R^2 resulted satisfactory for all the tested dispersions, except for ASW2 and AEW at 0.01 mg/l and AFW at 0.1 and 10 mg/l, respectively, for which

R^2 was calculated 10 or 5 h from the beginning of the experiment, as a function of the straight-line behavior observed (Brunelli et al., 2013).

Table 5.7 – Size distribution (average ± standard deviation, nm) of n-TiO_2 P25 dispersed in the tested aqueous solutions at different concentration levels and times (AFW: artificial freshwater; AEW: artificial estuarine water; ASW1: artificial seawater 1; ASW2: artificial seawater 2; LW; lagoon water; SW: seawater).

mg/l	Time (h)	AFW	AEW	ASW1	ASW2	LW	SW
0.1	0.2	221±3	164±15	180±21	297±47	262±32	229±25
	25	290±15	220±18	207±26	381±90	156±9	448±55
	50	251 ± 4	270 ± 10	304 ± 38	246 ± 16	161 ± 8	315 ± 41
1.0	0.2	294 ± 37	194 ± 11	161 ± 19	350 ± 41	331 ± 71	375 ± 31
	25	225 ± 8	607 ± 10	799 ± 120	466 ± 9	827 ± 166	610 ± 52
	50	228 ± 15	663 ± 69	738 ± 84	519 ± 59	514 ± 63	512 ± 51
10	0.2	290 ± 19	271 ± 34	505 ± 24	401 ± 42	492 ± 43	598 ± 41
	25	627 ± 25	226 ± 14	531 ± 51	883 ± 114	608 ± 53	720 ± 62
	50	548 ± 29	211 ± 11	344 ± 30	1137 ± 48	419 ± 8	588 ± 64

Table 5.7 displays that the formation of agglomerates was observed immediately after the DLS measurement (i.e. 0.2 h or 12 min), regardless the initial concentration of P25. The average size of agglomerates at 0.2 h was found in the range of 164-405 nm for the artificial samples (i.e. AFW, AEW, ASW1, ASW2), and of 492 and 598 nm for the real samples (i.e. LW and SW), respectively. Then, a general growth of the agglomerates size, up to 800–880 nm, was recorded at 25 h, with some exceptions (e.g. AFW at 1.0 mg/l and LW at 0.1 mg/l). The average sizes of agglomerates after 50 h did not shown the same trend as after 25 h, because of some decreases in size distribution. In detail, AFW was the only aqueous dispersion presenting stable agglomerates (around 200 nm size) throughout the entire experiment time, both at 0.1 and 1 mg/l. The values of P25 agglomerates for salt solutions after 0.2 h at 10 mg/l were higher (up to 598 ± 41 nm recorded for SW) compared to those at lower initial concentrations. Over the experiment time course,

the average sizes of agglomerates became generally larger, reaching 1137 ± 48 nm for ASW2 at 50 h. The smaller agglomerates of P25, recorded in the freshwater dispersion, compared to the other dispersions, are likely related to the lower salinity and divalent cation concentration, thus decreasing the probability of interaction between P25 and the surrounding ions.

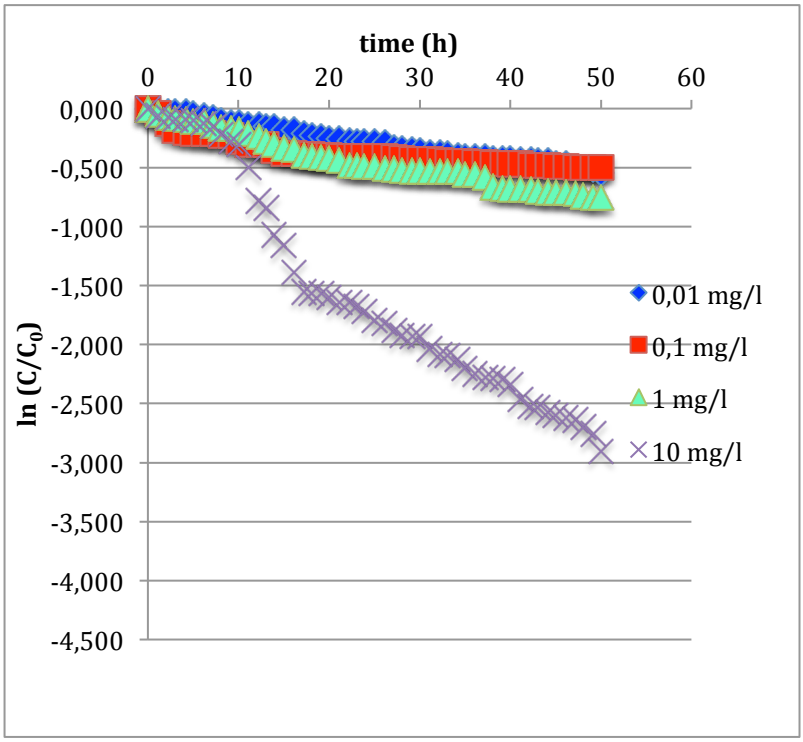

Figure 5.17 - Sedimentation profiles of n-TiO_2 P25 dispersed into AFW (synthetic freshwater sample) at the tested concentrations.

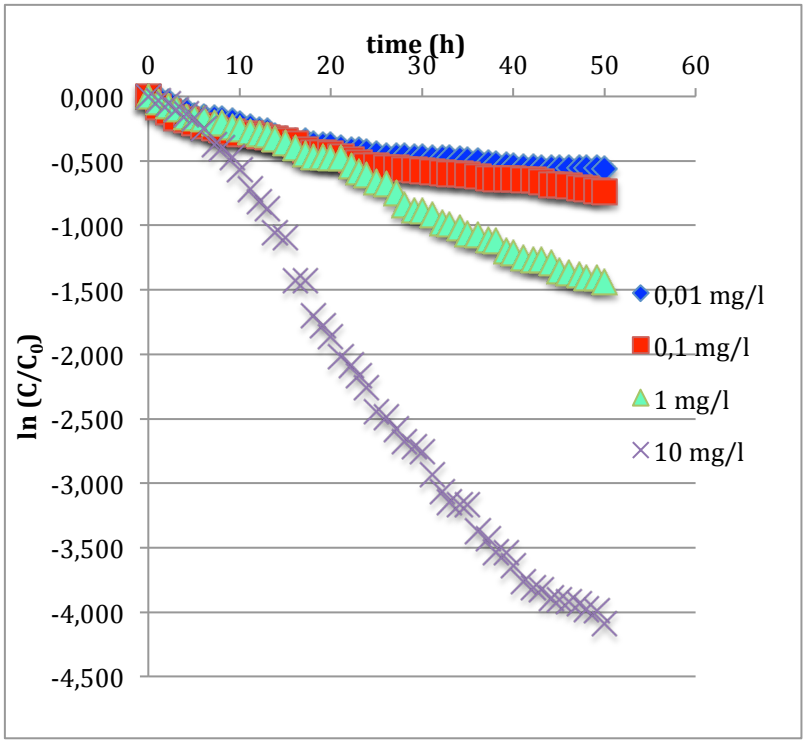

Figure 5.18 - Sedimentation profiles of n-TiO_2 P25 dispersed into ASW1 (synthetic seawater sample) at the tested concentrations.

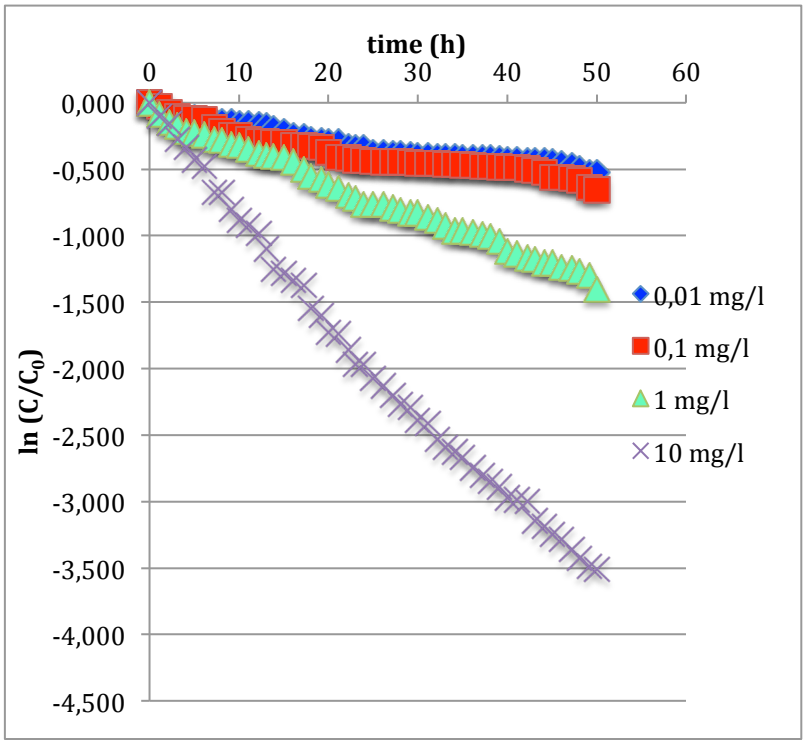

Figure 5.19 - Sedimentation profiles of n-TiO_2 P25 dispersed into SW (real seawater sample) at different tested concentrations.

Table 5.8 - First order fitting equation parameters for the all dispersions, calculated from the experimental sedimentation profiles (AFW: artificial freshwater; AEW: artificial estuarine water; ASW1: artificial seawater 1; ASW2: artificial seawater 2).

Sample	n-TiO_2 P25 concentration (mg/l)	k (s^{-1})	R^2
AFW	0.01	$3 \cdot 10^{-6}$	0.981
	0.1[a]	$1 \cdot 10^{-5}$	0.932
	1	$5 \cdot 10^{-6}$	0.935
	10[b]	$7 \cdot 10^{-6}$	0.904
AEW	0.01[b]	$9 \cdot 10^{-6}$	0.904
	0.1	$5 \cdot 10^{-6}$	0.750
	1	$8 \cdot 10^{-6}$	0.989
	10	$2 \cdot 10^{-5}$	0.931
ASW1	0.01	$4 \cdot 10^{-6}$	0.778
	0.1	$5 \cdot 10^{-6}$	0.773
	1	$8 \cdot 10^{-6}$	0.986
	10	$2 \cdot 10^{-5}$	0.979
ASW2	0.01[b]	$7 \cdot 10^{-6}$	0.909
	0.1	$4 \cdot 10^{-6}$	0.891
	1	$8 \cdot 10^{-6}$	0.965
	10	$2 \cdot 10^{-5}$	0.978
LW	0.01	$3 \cdot 10^{-6}$	0.860
	0.1	$4 \cdot 10^{-6}$	0.741
	1	$1 \cdot 10^{-5}$	0.810
	10	$2 \cdot 10^{-5}$	0.926
SW	0.01	$3 \cdot 10^{-6}$	0.864
	0.1	$4 \cdot 10^{-6}$	0.760
	1	$8 \cdot 10^{-6}$	0.981
	10	$2 \cdot 10^{-5}$	0.983

[a] k and R^2 were calculated 5 h from the beginning because of the non-linear behavior observed.

[b] k and R^2 were calculated 10 h from the beginning because of the non-linear behavior observed.

The overall P25 sedimentation results obeys the first-order kinetic regardless of the dispersion composition (i.e. artificial/real seawater or artificial freshwater) when the initial amount of P25 is >0.1 mg/l. The k values (Table 5.8) covered approximately one order of magnitude, ranging from $3 \cdot 10^{-6}$ to $2 \cdot 10^{-5}$ s^{-1}, increasing with the increasing of concentration.

From Figures 5.17-5.19 and Table 5.8, it follows that there were small differences among sedimentation rates of all dispersions at the lowest dispersion concentrations, i.e. 0.01 and 0.1 mg/l, taking into account approximations described above. The settled P25 observed after 50 h ranged from 33.5 to 52.2 % of the initial concentrations (Figures A2-1 and A2-2, Annex 2). With regard to the 1 mg/l dispersion concentration, an intermediate sedimentation profile was observed for both artificial and real seawater dispersions (Figures 4.18-4.19) and for the estuarine like artificial dispersion (Figure A2-3, Annex 2), while the artificial freshwater dispersion showed a sedimentation profile very similar to that of lower concentrations (Figure 5.17). The settled P25 at 1 mg/l after 50 h was in the range of 53–79 % initial concentration. Taking into account the highest initial concentration of 10 mg/l, P25 sedimentation behavior was basically the same for all the aqueous dispersions (Figure A2-4, Annex 2), and the settled P25 in all dispersions reached very similar values after 50 h, ranging from 94.5 to 98.3 % initial concentration. A similar behavior was already reported for n-TiO_2 in real environmental waters but only at much higher concentration (200 mg/l) over a quite shorter time (400 min), approximately 80 % being settled after 2 h (Keller et al., 2010).

As far as the AFW sedimentation profiles (Figure 5.17) are concerned, it can be observed that they were quite similar for all dispersion concentrations, except at 10 mg/l. At this concentration, three significantly different settling rates were recognized: one from 0 to approx. 7 h, one from approx. 7 to approx. 17 h and the last one from ca. 17 to the end of the experiment, which resulted in an overall sigma shaped curve. This would suggest the slow formation of agglomerates, which, upon achieving a critical size, settled more rapidly than agglomeration, i.e. the agglomeration is the limiting step for sedimentation. Considering the artificial sea sample ASW1 (Figure 5.18), the sedimentation profiles were very similar to those of the real seawater sample SW (Figure 5.19). This similarity suggests that the sedimentation rate recorded in this

investigation is not significantly affected by organic matter, because DOC was <0.1 mg/l in the ASW1 dispersion and 2.16 mg/l in the SW dispersion, respectively.

6. DISCUSSION

Primary characterization data of ENM, collected in collaboration with project partners and further integrated with particles size distribution calculated from TEM images and inorganic impurities of toxicological concern by ICP analysis, are shown in chapter 5. Since the investigation of ENM behavior in the environment was the main activity performed within this work, chapter 6 is mainly concerned to the discussion of secondary characterization of the tested ENM. Moreover, due to the lack of standardization in the testing conditions (Dusinska and NanoTEST-consortium, 2009; Macken et al., 2012; Magdolenova et al., 2012) to successfully test, use and investigate ENM effects (Adair et al., 2010; Hondow et al., 2012), the noteworthy relevance, in nanotoxicology, of the ENM standardized protocols shown in chapter 5, will be discussed here.

As far the study of ENP behavior in biological media, the whole DLS data in Table 5.3 highlighted that the agglomeration occurred for each ENP tested depending on the ENP type considered. The stability of some dispersions (i.e. NRCWE-003, NM-101, NM-110 and NM-111) might be explained with the adsorption of proteins on particles surface, influencing the particle hydrodynamic diameter (Dobrovolskaia et al., 2009; Jans et al., 2009). On the other hand, other dispersions (especially NRCWE-001, NRCWE-002 and 47MN-03) highlighted that FBS seems to be the limiting factor of the agglomeration, regardless the medium considered.

According to the results obtained with analytical centrifugation, simultaing 24 h of real sedimentation (Figures 4.4-4.12), ENP stability significantly differed among dispersions, being mostly affected by the presence of FBS, which acted as a stabilizer. The highest stability (96±51 nm) in all biological media, exhibited by the only sample in a dispersion state (NM-300), highlighted the key role of organic stabilizers in ENP dispersions. Thus, an inverse relationship between the amount of FBS in dispersion and the demixing over time, i.e. the sedimentation rate, is clearly underlined by dispersions composed by NRCWE-003, NRCWE-004, 47MN-03, NM-110 and NM 111 (Figures 4.6, 4.7, 4.10, 4.11 and 4.12, respectively). The highest instability values for

all tested ENP were recorded in RPMI medium, without any added stabilizer. To a minor extent, the stability over time in biological media was affected by ENP type. n-ZnO samples behaved very similar, with a % of demixing in the range of 15-20% and 8-15%, respectively, even if they had different physico-chemical properties, as shown in Table 5.2b. Furthermore, NRCWE-001, NRCWE-002 and P25 presented demixing values in a fairly narrow range (15-30% of demixing), instead of the highest instability values, measured for NRCWE-003, that was negatively charged with caprylamine, NRCWE-004, NM-101 and 47MN-03 (30-60% of demixing).

In conclusion it could be stated that both physico-chemical properties of the tested ENM and FBS added to dispersions have been confirmed to heavily affected the ENM stability in biological media over time, in terms of agglomeration and sedimentation.

With regard to the investigation of ENM biodistribution in mice brains (i.e. a secondary target organ, according to toxicological tests performed by ENPRA partners), based on analytical protocol developed, a preliminary study about ENM extraction efficiency, followed by ENM quantification after toxicological testing, were performed. In general, as it could be expected, the ENM amount in the secondary target organ investigated 24 h after administration was relatively significant only for: (i) samples treated with the n-TiO_2 powders, with the smallest diameter size range; (ii) samples administered with MWCNT, at the highest initial concentrations tested. The theory is that a small percentage of ENM with small particles size had most likely to pass the blood-alveolar barrier into the bloodstream to reach the brain, while the others underwent agglomeration, stopping in primary target organs (according to intratracheally instillation of ENM), such as e.g. in lungs, gut and liver. By comparing data on samples administered with n-TiO_2 in Table 5.6 and in Figure 5.15, one of the most important parameter that affected the ENM presence in mice brain appears to be the size: the smaller the particle size, the higher the concentration detected, especially comparing these data with primary characterization values of NRCWE-001 (crystallite size: 10; size distribution: 80-400 nm for 80% particles) and NRCWE-004 (crystallite size: 94; size distribution: 1-2000 nm). Moreover, also chemical composition might have played a role in their translocation from tracheal tract to brain, as highlighted by the only presence of Ti and Al after toxicological testing.

The investigation of P25 in synthetic and real waters highlighted that both agglomeration and sedimentation depended mostly on initial concentration tested and, to a minor extent, on salt content, IS and DOC. The overall DLS data summarized in Table 5.7 indicate that the agglomeration behavior of P25 is primarily affected by the initial concentration and, secondly, by the time duration of each experiment. While the average size of P25 agglomerates generally increased with time over the initial hours (up to 25 h), the average size of agglomerates of most samples was found at 50 h similar or lower than those at 25 h. This experimental finding could be related to the concurrent sedimentation of larger agglomerates, as confirmed by sedimentation profiles (Figures 5.17-5.19), with consequent decrease of the average size of agglomerates, due to reduced residual concentrations of particles in the aqueous solution. The occurrence of ENP agglomerates up to 1500 nm was already observed for river and lake water samples (Zhang et al., 2009). As far P25 sedimentation in both artificial and real aqueous matrices, the obtained profiles can be described by applying a first order kinetic equation, displaying a similar behavior, according to the initial concentration tested. The only difference observed stems from the lowest sedimentation rate shown by AFW at 1 mg/l and 10 mg/l, in comparison with the highest reached by salt water samples (i.e. LW at 1 mg/l and ASW at 10 mg/l, respectively).

Furthermore, the actual dispersed P25 concentrations at 1, 5, 10, 15, 25 and 50 h were calculated from sedimentation data and reported in Table A2-1, Annex 2. These data showed that the actual concentration of dispersed P25 is by far lower than the nominal concentration, especially at the highest dispersion concentrations, i.e. 1 and 10 mg/l. Moreover, the final average concentration(i.e. at 50 h) of all dispersions was 60% of the initial amount of P25 at 0.01 mg/l, 51% at 0.1 mg/l, 27% at 1 mg/l, reaching finally 4% at 10 mg/l. It follows that, for instance, the difference between the actual and final concentrations of the P25 sea water dispersions of 0.1 and 10 mg/l, respectively, was only a factor 6 instead of a factor 100. These results may have quite significant implications on the evaluation of n-TiO_2 toxicity if the actual exposure concentration is not estimated before testing.

As regards the comparison about the n-TiO_2 P25 behavior, both dispersed in biological and aqueous media, some differences were observed. In general the overall results demonstrated that agglomeration depended on the P25 initial concentration

and only on biological medium tested. Size distributions recorded were in a very wide range, starting from 161±8 up to 1137±48 (in water dispersions) and from 258±101 to a maximum of 667±298 (in biological media). The narrower size distribution of P25 dispersed in water solutions rather than in biological media could be explained by the higher amount of substances (i.e. inorganic salts, proteins, amino acids, etc.) in the latter media, that easily interact with P25. Even if this broad range of size distributions obtained, P25 stability both in water solutions and in biological media was shown to be relatively constant with respect to other ENP dispersions. The reason could be referred to its spherical shape, observed from primary characterization data (Tables 5.4a and b), which increased the tendency of interaction with other substances in dispersion, as already published (Deng et al., 2009), providing greater stability over time.

Finally, one of the main outcomes of this thesis is the development of standardized protocols, useful during, as well as after, toxicological testing. As emphasized by recent literature, due to the relatively new field of research and to the lack of a meaningful correlation between ENM properties and the relate toxicity, the set up of appropriate standardized protocols is demanded, in order to minimize biases by samples handling, providing reproducible toxicity results.

In general an extensive physico-chemical characterization before providing ENM standardized protocols is strongly required in order to understand which parameters may affect their implementation. ENP dispersion protocols underlined the need to handle each ENP separately, tailoring from time to time the experimental conditions. Initial ENP concentration, types of vials and media investigated, pH, type and time of sonication, potential artifacts, degree of ENP stability towards agglomeration and sedimentation, as well as the pre- and post-treatment storage conditions are the main parameters to be taken into account when developing a dispersion protocol for ENP. Thus, general suggestions from the proposed dispersion protocols are listed as follows: (i) decrease the ENP initial concentration at the minimum acceptable by the employed technique to decrease the likelyhood of agglomeration and sedimentation; (ii) use probe sonication, instead of bath or vortex, to obtain as homogeneous as possible dispersion; (iii) work with high power sonication (up to 100 W) and for a relatively long time (up to 30 min) to guarantee good dispersibility; (vi) use freshly prepared dispersion and store it at room T, to avoid

agglomeration and sedimentation. As regards the methodology provided for ENM identification and quantification in biological samples, as previously mentioned for ENP dispersion protocols, the results indicated that it requires the development of tailored analytical protocol for each ENM tested, setting the suitable acid mixture, time and temperature of digestion, as well as selecting proper tracers for ENM presence in tissues, according to primary characterization database.

7. Conclusions

The characterization approach applied to both inorganic and organic ENM through this work showed that the determination of the wide set of physico-chemical properties of pristine ENM, the study of ENM behavior in the environment, as well as the investigation of ENM biodistribution after toxicological testing, covered some of the key challenges in nanotoxicology. In addition, according to the lack of ENM standardized protocols, for both *in vitro* and *in vivo* toxicity testing, and recent requirements from International Organizations and the European Commission, dispersion protocols of the tested ENP in biological media for *in vitro* testing as well as analytical protocols for assessing ENM quantification in a secondary target organ after toxicological testing have been developed.

First, the obtained results stressed the need to develop and apply standardized protocols for ENM, before, during and after toxicological testing, in order to perform a meaningful comparison between toxicity data of ENM.

As far the the ENP stability in the environmental samples tested, the findings highlighted that the main parameters affecting ENP stability are the initial concentration of ENP and specific stabilizers, and, to a minor extent, media composition or ENP type. Furthermore, with regard to the advanced characterization performed on n-TiO_2 P25, sedimentation rates in both syntehtic and real waters, the settling rate constant, as well as exposure concentration to n-TiO_2 after a time frame usually used for toxicological testing were provided, in order to better elucidate the effective dose-response relationship for nanotoxicology. As far the investigation of ENM biodistribution, the ENM partitioning through target organs was observed to be mainly affected by chemical composition and particle size, rather than the other physico-chemical parameters measured.

The overall outcomes could be extremely useful under many perspectives, such as for obtaining reliable toxicity data by applying standardized methodologies and for better understanding the mode of action of the investigated ENM in several target organs. Further research could also be oriented to design other relevant experiments in order to gain a thorough understanding of the mechanisms behaind a certain

toxicological response, supporting the development of quantitative structure-activity relationships (i.e. QSAR modeling) of ENM as well as for modeling behavior and fate of ENM in the environment. The ultimate goal would be to provide an integrated approach between risk assessment and life cycle assessment of ENM.

References

Aaron JS, Greene AC, Kotula PG, Bachand GD, Timlin JA. Advanced Optical Imaging Reveals the Dependence of Particle Geometry on Interactions Between CdSe Quantum Dots and Immune Cells. Small 2011; 7: 334-341.

Adair JH, Parette MP, Altınoğlu Eİ, Kester M. Nanoparticulate Alternatives for Drug Delivery. Acs Nano 2010; 4: 4967-4970.

Adeli M, Kalantari M, Parsamanesh M, Sadeghi E, Mahmoudi M. Synthesis of new hybrid nanomaterials: promising systems for cancer therapy. Nanomedicine: Nanotechnology, Biology and Medicine 2011; 7: 806-817.

Ahmed N, Fessi H, Elaissari A. Theranostic applications of nanoparticles in cancer. Drug Discovery Today 2012; 17: 928-934.

Alivisatos AP. Perspectives on the Physical Chemistry of Semiconductor Nanocrystals. The Journal of Physical Chemistry 1996; 100: 13226-13239.

Allen HJ, Impellitteri CA, Macke DA, Heckman JL, Poynton HC, Lazorchak JM, et al. Effects from filtration, capping agents, and presence/absence of food on the toxicity of silver nanoparticles to Daphnia magna. Environmental Toxicology and Chemistry 2010; 29: 2742-2750.

Allouni ZE, Cimpan MR, Hol PJ, Skodvin T, Gjerdet NR. Agglomeration and sedimentation of TiO2 nanoparticles in cell culture medium. Colloids and Surfaces B-Biointerfaces 2009; 68: 83-87.

Amstad E, Textor M, Reimhult E. Stabilization and functionalization of iron oxide nanoparticles for biomedical applications. Nanoscale 2011; 3: 2819-2843.

Ashby MF, Ferreira PJ, Schodek DL. Chapter 8 - Nanomaterials: Synthesis and Characterization. Nanomaterials, Nanotechnologies and Design. Butterworth-Heinemann, Boston, 2009, pp. 257-290.

ASTM, E724-98. Standard guide for conducting static acute toxicity tests starting with Embryos of Four Species of Saltwater Bivalve Molluscs West Conshohocken, PA, 2004 (2012).

ASTM, E729-96. Standard guide for conducting acute toxicity tests on test materials with fishes, macroinvertebrates, and amphibians 11.05, West Conshohocken, PA, 2004 (2007).

Auffan M, Chaurand P, Botta C, Labille J, Masion A, Bottero J-Y, et al. Exposure and environmental impact during the life cycle of manufactured nanomaterials. Actualite Chimique 2012: 59-62.

Auffan M, Pedeutour M, Rose J, Masion A, Ziarelli F, Borschneck D, et al. Structural Degradation at the Surface of a TiO2-Based Nanomaterial Used in Cosmetics. Environmental Science & Technology 2010; 44: 2689-2694.

Bakry R, Vallant RM, Najam-ul-Haq M, Rainer M, Szabo Z, Huck CW, et al. Medicinal applications of fullerenes. International Journal of Nanomedicine 2007; 2: 639-649.

Barik TK, Sahu B, Swain V. Nanosilica—from medicine to pest control. Parasitology Research 2008; 103: 253-258.

Barrett EP, Joyner LG, Halenda PP. The Determination of Pore Volume and Area Distributions in Porous Substances. I. Computations from Nitrogen Isotherms. Journal of the American Chemical Society 1951; 73: 373-380.

Bauer C, Buchgeister J, Hischier R, Poganietz WR, Schebek L, Warsen J. Towards a framework for life cycle thinking in the assessment of nanotechnology. Journal of Cleaner Production 2008; 16: 910-926.

Becheri A, Dürr M, Lo Nostro P, Baglioni P. Synthesis and characterization of zinc oxide nanoparticles: application to textiles as UV-absorbers. Journal of Nanoparticle Research 2008; 10: 679-689.

Benn TM, Westerhoff P. Nanoparticle Silver Released into Water from Commercially Available Sock Fabrics. Environmental Science & Technology 2008; 42: 4133-4139.

Bertsch A, Jiguet S, Renaud P. Microfabrication of ceramic components by microstereolithography. Journal of Micromechanics and Microengineering 2004; 14: 197.

Betancourt-Galindo R, Miranda CC, Urbina BAP, Castaneda-Facio A, Sanchez-Valdés S, Padilla JM, et al. Encapsulation of Silver Nanoparticles in a Polystyrene Matrix by Miniemulsion Polymerization and Its Antimicrobial Activity. ISRN Nanotechnology 2012: 5.

Bhattacharya R, Mukherjee P. Biological properties of “naked” metal nanoparticles. Advanced Drug Delivery Reviews 2008; 60: 1289-1306.

Biswas P, Wu CY. 2005 Critical Review: Nanoparticles and the environment. Journal of the Air & Waste Management Association 2005; 55: 708-746.

Blaser SA, Scheringer M, MacLeod M, Hungerbühler K. Estimation of cumulative aquatic exposure and risk due to silver: Contribution of nano-functionalized plastics and textiles. Science of The Total Environment 2008; 390: 396-409.

Blinova I, Ivask A, Heinlaan M, Mortimer M, Kahru A. Ecotoxicity of nanoparticles of CuO and ZnO in natural water. Environmental Pollution 2010; 158: 41-47.

Boczkowski J, Lanone S. Respiratory toxicities of nanomaterials — A focus on carbon nanotubes. Advanced Drug Delivery Reviews 2012; 64: 1694-1699.

Borm P, Robbins D, Haubold S, Kuhlbusch T, Fissan H, Donaldson K, et al. The potential risks of nanomaterials: a review carried out for ECETOC. Particle and Fibre Toxicology 2006; 3: 11.

Brar SK, Verma M, Tyagi RD, Surampalli RY. Engineered nanoparticles in wastewater and wastewater sludge – Evidence and impacts. Waste Management 2010; 30: 504-520.

Brown S, Palazuelos M, Sharma P, Powers K, Roberts S, Grobmyer S, et al. Nanoparticle Characterization for Cancer Nanotechnology and Other Biological Applications. In: Grobmyer SR, Moudgil BM, editors. Cancer Nanotechnology. 624. Humana Press, 2010, pp. 39-65.

Brunelli A, Pojana G, Callegaro S, Marcomini A. Agglomeration and sedimentation of titanium dioxide nanoparticles (n-TiO2) in synthetic and real waters. Journal of Nanoparticle Research 2013; 15: 1-10.

BSI. Terminology for nanomaterials. Public Available Specification. British Standards Institution, London, 2007, pp. 16.

Buzea C, Pacheco I, Robbie K. Nanomaterials and nanoparticles: Sources and toxicity. Biointerphases 2007; 2: MR17-MR71.

Caitlin EB, Jordan A, William BW, Baohong Z. Effects of Aluminum Oxide Nanoparticles on the Growth, Development, and microRNA Expression of Tobacco (Nicotiana tabacum). PLoS One 2012; 7.

Chawla P, Chawla V, Maheshwari R, Saraf SA, Saraf SK. Fullerenes: From Carbon to Nanomedicine. Mini-Reviews in Medicinal Chemistry 2010; 10: 662-677.

Chen J, Dong X, Zhao J, Tang G. In vivo acute toxicity of titanium dioxide nanoparticles to mice after intraperitioneal injection. Journal of Applied Toxicology 2009; 29: 330-337.

Chen J, Patil S, Seal S, McGinnis JF. Rare earth nanoparticles prevent retinal degeneration induced by intracellular peroxides. Nat Nano 2006; 1: 142-150.

Chen X, Mao SS. Titanium Dioxide Nanomaterials: Synthesis, Properties, Modifications, and Applications. ChemInform 2007; 38: no-no.

Chen Z, Mao R, Liu Y. Fullerenes for Cancer Diagnosis and Therapy: Preparation, Biological and Clinical Perspectives. Current Drug Metabolism 2012; 13: 1035-1045.

Chithrani BD, Ghazani AA, Chan WCW. Determining the Size and Shape Dependence of Gold Nanoparticle Uptake into Mammalian Cells. Nano Letters 2006; 6: 662-668.

Clement L, Zenerino A, Hurel C, Amigoni S, Taffin de Givenchy E, Guittard F, et al. Toxicity assessment of silica nanoparticles, functionalised silica nanoparticles, and HASE-grafted silica nanoparticles. The Science of the total environment 2013; 450-451: 120-8.

Cobley CM, Chen J, Cho EC, Wang LV, Xia Y. Gold nanostructures: a class of multifunctional materials for biomedical applications. Chemical Society Reviews 2011; 40: 44-56.

COM(2012)527. Communication from the Commission to the Parliament, the Council and the European Economic and Social Committee: Second Regulatory Review on Nanomaterials. European Commission, Brussels, 2012, pp. 15.

Dailey LA, Jekel N, Fink L, Gessler T, Schmehl T, Wittmar M, et al. Investigation of the proinflammatory potential of biodegradable nanoparticle drug delivery systems in the lung. Toxicology and Applied Pharmacology 2006; 215: 100-108.

de Gennes P-G, Brochard-Wyart F, Quere D. Drops, Bubbles, Pearls, Waves: Springer, 2004.

De Stefano D, Carnuccio R, Maiuri MC. Nanomaterials Toxicity and Cell Death Modalities. Journal of Drug Delivery 2012; 2012: 14.

Deng ZJ, Mortimer G, Schiller T, Musumeci A, Martin D, Minchin RF. Differential plasma protein binding to metal oxide nanoparticles. Nanotechnology 2009; 20.

Dhawan A, Sharma V. Toxicity assessment of nanomaterials: methods and challenges. Analytical and Bioanalytical Chemistry 2010; 398: 589-605.

Dobrovolskaia MA, Patri AK, Zheng J, Clogston JD, Ayub N, Aggarwal P, et al. Interaction of colloidal gold nanoparticles with human blood: effects on particle size and analysis of plasma protein binding profiles. Nanomedicine: Nanotechnology, Biology and Medicine 2009; 5: 106-117.

Donaldson K, Aitken R, Tran L, Stone V, Duffin R, Forrest G, et al. Carbon Nanotubes: A Review of Their Properties in Relation to Pulmonary Toxicology and Workplace Safety. Toxicological Sciences 2006; 92: 5-22.

Donaldson K, Stone V, Tran C, Kreyling W, Borm P. Nanotoxicology. Occup Environ Med 2004; 61: 727 - 728.

Doumari HA, Mahmoudi M, Lascialfari A. Superparamagnetic colloidal nanocrystal clusters coated with polyethylene glycol fumarate : a possible novel theranostic agent. Nanoscale 2011; 3: 1022 - 1030.

Dowling AP. Development of nanotechnologies. Materials Today 2004; 7: 30-35.

Drescher D, Orts-Gil G, Laube G, Natte K, Veh R, Österle W, et al. Toxicity of amorphous silica nanoparticles on eukaryotic cell model is determined by particle agglomeration and serum protein adsorption effects. Analytical and Bioanalytical Chemistry 2011; 400: 1367-1373.

Dusinska M, NanoTEST-consortium. Testing strategies for the safety of nanoparticles used in medical applications. Nanomedicine 2009; 4: 605-607.

Dutta J, Hofmann H. Self-Organization of Colloidal Nanoparticles. In: Nalwa HS, editor. Encyclopedia of Nanoscience and Nanotechnology. X. American Scientific Publisher, 2004, pp. 1-23.

El-Sayed M. Small is different: shape-, size-, and composition-dependent properties of some colloidal semiconductor nanocrystals. Accounts Chem Res 2004; 37: 326 - 333.

Elsaesser A, Howard CV. Toxicology of nanoparticles. Advanced Drug Delivery Reviews 2012; 64: 129-137.

Espitia P, Soares Nd, Coimbra Jd, Andrade N, Cruz R, Medeiros E. Zinc Oxide Nanoparticles: Synthesis, Antimicrobial Activity and Food Packaging Applications. Food and Bioprocess Technology 2012; 5: 1447-1464.

EU. Nanosciences and nanotechnologies: an action plan for Europe 2005-2009, 2005-243.

EU. Reccomendation on the definition of a nanomaterial, 2011, October 18

Farkas J, Peter H, Christian P, Gallego Urrea JA, Hassellöv M, Tuoriniemi J, et al. Characterization of the effluent from a nanosilver producing washing machine. Environment International 2011; 37: 1057-1062.

Fede C, Selvestrel F, Compagnin C, Mognato M, Mancin F, Reddi E, et al. The toxicity outcome of silica nanoparticles (Ludox (R)) is influenced by testing techniques and treatment modalities. Analytical and Bioanalytical Chemistry 2012; 404: 1789-1802.

Feynman R. There's Plenty of Room at the Bottom, American Physical Society meeting, Caltech, CA, 1959.

French RA, Jacobson AR, Kim B, Isley SL, Penn RL, Baveye PC. Influence of Ionic Strength, pH, and Cation Valence on Aggregation Kinetics of Titanium Dioxide Nanoparticles. Environmental Science & Technology 2009; 43: 1354-1359.

Gangwai S, Brown J, Wang A, Houck K, Dix D, Kavlock R, et al. Informing selection of nanomaterial concentra- tions for ToxCast in vitro testing based on occupational exposure potential. Environ Health Perspect 2011; 119: 1539-1546.

Geiser M, Kreyling WG. Deposition and biokinetics of inhaled nanoparticles. Particle and Fibre Toxicology 2010; 7.

Ghosh P, Han G, De M, Kim CK, Rotello VM. Gold nanoparticles in delivery applications. Advanced Drug Delivery Reviews 2008; 60: 1307-1315.

Gomez J, Tigli O. Zinc oxide nanostructures: from growth to application. Journal of Materials Science 2013; 48: 612-624.

Gomez JL, Tigli O. Modeling and simulation of zinc oxide nanowire field effect transistor biosensor. Nanotechnology Materials and Devices Conference (NMDC), 2011 IEEE, 2011, pp. 412-415.

Gottschalk F, Nowack B. The release of engineered nanomaterials to the environment. Journal of Environmental Monitoring 2011; 13: 1145-1155.

Gottschalk F, Sonderer T, Scholz RW, Nowack B. Possibilities and limitations of modeling environmental exposure to engineered nanomaterials by probabilistic material flow analysis. Environmental Toxicology and Chemistry 2010; 29: 1036-1048.

Grieger KD, Fjordboge A, Hartmann NB, Eriksson E, Bjerg PL, Baun A. Environmental benefits and risks of zero-valent iron nanoparticles (nZVI) for in situ remediation: Risk mitigation or trade-off? Journal of Contaminant Hydrology 2010; 118: 165-183.

Griffitt RJ, Luo J, Gao J, Bonzongo JC, Barber DS. Effects of particle composition and species on toxicity of metallic nanomaterials in aquatic organisms. Environmental Toxicology and Chemistry 2008; 27: 1972-1978.

Guan X, Du J, Meng X, Sun Y, Sun B, Hu Q. Application of titanium dioxide in arsenic removal from water: A review. Journal of Hazardous Materials 2012; 215: 1-16.

Gupta AK, Gupta M. Synthesis and surface engineering of iron oxide nanoparticles for biomedical applications. Biomaterials 2005; 26: 3995-4021.

Hames Y, Alpaslan Z, Kösemen A, San SE, Yerli Y. Electrochemically grown ZnO nanorods for hybrid solar cell applications. Solar Energy 2010; 84: 426-431.

Hansen FS, Larsen BH, Olsen SI, Baun A. Categorization framework to aid hazard identification of nanomaterials. Nanotoxicology 2007; 1: 243-250.

Harper S, Usenko C, Hutchison JE, Maddux BLS, Tanguay RL. In Vivo Biodistribution and Toxicity Depends on Nanomaterial Composition, Size, Surface Functionalisation and Route of Exposure. J Exp Nanosci 2008; 3: 195-206.

Hassellöv M, Readman J, Ranville J, Tiede K. Nanoparticle analysis and characterization methodologies in environmental risk assessment of engineered nanoparticles. Ecotoxicology 2008; 17: 344-361.

Heinrich U, Fuhst R, Rittinghausen S, Creutzenberg O, Bellmann B, Koch W, et al. Chronic Inhalation Exposure of Wistar Rats and two Different Strains of Mice to Diesel Engine Exhaust, Carbon Black, and Titanium Dioxide. Inhalation Toxicology 1995; 7: 533-556.

Holgate ST. Exposure, Uptake, Distribution and Toxicity of Nanomaterials in Humans. Journal of Biomedical Nanotechnology 2010; 6: 1-19.

Hondow N, Brydson R, Wang P, Holton M, Brown MR, Rees P, et al. Quantitative characterization of nanoparticle agglomeration within biological media. Journal of Nanoparticle Research 2012; 14: 1-15.

Hsiao IL, Huang Y-J. Effects of various physicochemical characteristics on the toxicities of ZnO and TiO2 nanoparticles toward human lung epithelial cells. Science of The Total Environment 2011; 409: 1219-1228.

http://echa.europa.eu/web/guest/regulations/biocidal-products-regulation/nanomaterials. 2012.

Hua M, Zhang S, Pan B, Zhang W, Lv L, Zhang Q. Heavy metal removal from water/wastewater by nanosized metal oxides: A review. Journal of Hazardous Materials 2012; 211–212: 317-331.

Huang X, El-Sayed MA. Gold nanoparticles: Optical properties and implementations in cancer diagnosis and photothermal therapy. Journal of Advanced Research 2010; 1: 13-28.

Huber DL. Synthesis, properties, and applications of iron nanoparticles. Small 2005; 1: 482-501.

Iijima M, Yonemochi Y, Kimata M, Hasegawa M, Tsukada M, Kamiya H. Preparation of agglomeration-free hematite particles coated with silica and their reduction behavior in hydrogen. Journal of Colloid and Interface Science 2005; 287: 526-533.

Isoda K, Hasezaki T, Kondoh M, Tsutsumi Y, Yagi K. Effect of surface charge on nano-sized silica particles-induced liver injury. Die Pharmazie - An International Journal of Pharmaceutical Sciences 2011; 66: 278-281.

Jacobsen NR, Pojana G, White P, Moller P, Cohn CA, Korsholm KS, et al. Genotoxicity, cytotoxicity, and reactive oxygen species induced by single-walled carbon nanotubes and C-60 fullerenes in the FE1-Muta (TM) mouse lung epithelial cells. Environmental and Molecular Mutagenesis 2008; 49: 476-487.

Jacobsen NR, Saber AT, White P, Moller P, Pojana G, Vogel U, et al. Increased mutant frequency by carbon black, but not quartz, in the lacZ and cll transgenes of Muta (TM) Mouse lung epithelial cells. Environmental and Molecular Mutagenesis 2007; 48: 451-461.

Jans H, Liu X, Austin L, Maes G, Huo Q. Dynamic Light Scattering as a Powerful Tool for Gold Nanoparticle Bioconjugation and Biomolecular Binding Studies. Analytical Chemistry 2009; 81: 9425-9432.

Jaurand M-C, Renier A, Daubriac J. Mesothelioma: Do asbestos and carbon nanotubes pose the same health risk? Particle and Fibre Toxicology 2009; 6: 16.

Jiang J, Oberdoerster G, Elder A, Gelein R, Mercer P, Biswas P. Does nanoparticle activity depend upon size and crystal phase? Nanotoxicology 2008; 2: 33-42.

Jodin L, Dupuis A-C, Rouvière E, Reiss P. Influence of the Catalyst Type on the Growth of Carbon Nanotubes via Methane Chemical Vapor Deposition. The Journal of Physical Chemistry B 2006; 110: 7328-7333.

Jones N, Ray B, Ranjit KT, Manna AC. Antibacterial activity of ZnO nanoparticle suspensions on a broad spectrum of microorganisms. FEMS Microbiology Letters 2008; 279: 71-76.

Kaegi R, Sinnet B, Zuleeg S, Hagendorfer H, Mueller E, Vonbank R, et al. Release of silver nanoparticles from outdoor facades. Environmental Pollution 2010; 158: 2900-2905.

Kaegi R, Ulrich A, Sinnet B, Vonbank R, Wichser A, Zuleeg S, et al. Synthetic TiO(2) nanoparticle emission from exterior facades into the aquatic environment. Environmental Pollution 2008; 156: 233-239.

Kane AB, Hurt RH. Nanotoxicology: The asbestos analogy revisited. Nat Nano 2008; 3: 378-379.

Karlsson HL, Gustafsson J, Cronholm P, Möller L. Size-dependent toxicity of metal oxide particles—A comparison between nano- and micrometer size. Toxicology Letters 2009; 188: 112-118.

Kato H, Suzuki M, Fujita K, Horie M, Endoh S, Yoshida Y, et al. Reliable size determination of nanoparticles using dynamic light scattering method for in vitro toxicology assessment. Toxicology in Vitro 2009; 23: 927-934.

Keller AA, McFerran S, Lazareva A, Suh S. Global life cycle releases of engineered nanomaterials. Journal of Nanoparticle Research 2013; 15.

Keller AA, Wang H, Zhou D, Lenihan HS, Cherr G, Cardinale BJ, et al. Stability and Aggregation of Metal Oxide Nanoparticles in Natural Aqueous Matrices. Environmental Science & Technology 2010; 44: 1962-1967.

Kelly RJ. Occupational Medicine Implications of Engineered Nanoscale Particulate Matter, 2008.

Kermanizadeh A, Pojana G, Gaiser BK, Birkedal R, Bilanicova D, Wallin H, et al. In vitro assessment of engineered nanomaterials using a hepatocyte cell line: cytotoxicity, pro-inflammatory cytokines and functional markers. Nanotoxicology 2013; 7: 301-313.

Khaydarov RR, Khaydarov RA, Evgrafova S, Estrin Y. Using Silver Nanoparticles as an Antimicrobial Agent. In: Mikhalovsky S, Khajibaev A, editors. Biodefence. Springer Netherlands, 2011, pp. 169-177.

Kiser MA, Westerhoff P, Benn T, Wang Y, Perez-Rivera J, Hristovski K. Titanium Nanomaterial Removal and Release from Wastewater Treatment Plants. Environmental Science & Technology 2009; 43: 6757-6763.

Kobayashi N, Naya M, Endoh S, Maru J, Yamamoto K, Nakanishi J. Comparative pulmonary toxicity study of nano-TiO2 particles of different sizes and agglomerations in rats: Different short- and long-term post-instillation results. Toxicology 2009; 264: 110-118.

Kreilgaard M. Influence of microemulsions on cutaneous drug delivery. Advanced Drug Delivery Reviews 2002; 54, Supplement: S77-S98.

Kreyling WG, Semmler-Behnke M, Moller W. Ultrafine particle-lung interactions: Does size matter? Journal of Aerosol Medicine-Deposition Clearance and Effects in the Lung 2006; 19: 74-83.

Krishna V, Singh A, Sharma P, Iwakuma N, Wang Q, Zhang Q, et al. Polyhydroxy Fullerenes for Non-Invasive Cancer Imaging and Therapy. Small 2010; 6: 2236-2241.

Krug HF, Wick P. Nanotoxicology: An Interdisciplinary Challenge. Angewandte Chemie International Edition 2011; 50: 1260-1278.

Krystek P. A review on approaches to bio distribution studies about gold and silver engineered nanoparticles by inductively coupled plasma mass spectrometry. Microchemical Journal 2012; 105: 39-43.

Kwok KWH, Auffan M, Badireddy AR, Nelson CM, Wiesner MR, Chilkoti A, et al. Uptake of silver nanoparticles and toxicity to early life stages of Japanese medaka (Oryzias latipes): Effect of coating materials. Aquatic Toxicology 2012; 120–121: 59-66.

Labille J, Feng J, Botta C, Borschneck D, Sammut M, Cabie M, et al. Aging of TiO2 nanocomposites used in sunscreen. Dispersion and fate of the degradation products in aqueous environment. Environmental Pollution 2010; 158: 3482-3489.

Landi BJ, Ganter MJ, Cress CD, DiLeo RA, Raffaelle RP. Carbon nanotubes for lithium ion batteries. Energy & Environmental Science 2009; 2: 638-654.

Laurent S, Burtea C, Thirifays C, Haefeli UO, Mahmoudi M. Crucial Ignored Parameters on Nanotoxicology: The Importance of Toxicity Assay Modifications and "Cell Vision". PLoS One 2012; 7: 306-314.

Lawler DM, Townshend A. Spectrophotometry: Turbidimetry and nephelometry. Encyclopedia of Analytical Science. 8, 2005, pp. 343-351.

Lee I, Delbecq F, Morales R, Albiter MA, Zaera F. Tuning selectivity in catalysis by controlling particle shape. Nat Mater 2009; 8: 132-138.

Lerche D, Sobisch T. Consolidation of concentrated dispersions of nano- and microparticles determined by analytical centrifugation. Powder Technology 2007; 174: 46-49.

Limbach LK, Li Y, Grass RN, Brunner TJ, Hintermann MA, Muller M, et al. Oxide Nanoparticle Uptake in Human Lung Fibroblasts: Effects of Particle Size, Agglomeration, and Diffusion at Low Concentrations. Environmental Science & Technology 2005; 39: 9370-9376.

Lin Y-H, Mi F-L, Chen C-T, Chang W-C, Peng S-F, Liang H-F, et al. Preparation and Characterization of Nanoparticles Shelled with Chitosan for Oral Insulin Delivery. Biomacromolecules 2006; 8: 146-152.

Lin Y-S, Abadeer N, Haynes CL. Stability of small mesoporous silica nanoparticles in biological media. Chemical Communications 2011; 47: 532-534.

Lin Y-S, Haynes CL. Impacts of Mesoporous Silica Nanoparticle Size, Pore Ordering, and Pore Integrity on Hemolytic Activity. Journal of the American Chemical Society 2010; 132: 4834-4842.

Lorenz C, Von Goetz N, Scheringer M, Wormuth M, Hungerbühler K. Potential exposure of German consumers to engineered nanoparticles in cosmetics and personal care products. Nanotoxicology 2011; 5: 12-29.

Lövestam G, Rauscher H, Roebben G, Klüttgen BS, Gibson N, Putuad J-P, et al. Consideration on a Definition of a Nanomaterial for Regulatory Purposes, 2010.

Macken A, Byrne HJ, Thomas KV. Effects of salinity on the toxicity of ionic silver and Ag-PVP nanoparticles to Tisbe battagliai and Ceramium tenuicorne. Ecotoxicology and Environmental Safety 2012; 86: 101-110.

Maeyoshi Y, Saeki A, Suwa S, Omichi M, Marui H, Asano A, et al. Fullerene nanowires as a versatile platform for organic electronics. Sci. Rep. 2012; 2.

Magdolenova Z, Bilanicova D, Pojana G, Fjellsbo LM, Hudecova A, Hasplova K, et al. Impact of agglomeration and different dispersions of titanium dioxide nanoparticles on the human related in vitro cytotoxicity and genotoxicity. Journal of Environmental Monitoring 2012; 14: 455-464.

Mahmoudi M, Serpooshan V. Silver-Coated Engineered Magnetic Nanoparticles Are Promising for the Success in the Fight against Antibacterial Resistance Threat. Acs Nano 2012; 6: 2656-2664.

Malarkey EB, Parpura V. Applications of carbon nanotubes in neurobiology. Neurodegenerative Diseases 2007; 4: 292-299.

Mantyla AW. Standard Seawater Comparisons Updated. Journal of Physical Oceanography 1987; 17: 543-548.

Maquieira Á, Brun EM, Garcés-García M, Puchades R. Aluminum Oxide Nanoparticles as Carriers and Adjuvants for Eliciting Antibodies from Non-immunogenic Haptens. Analytical Chemistry 2012; 84: 9340-9348.

Messing M. Engineered Nanopartcles: Generation, Characterization and Applications. Department of Physics. Doctor of Philosophy. Lund University, Lund, Sweden, 2011.

Mitchell S, Perez-Ramirez J. Surface Science and Methods in Catalysis. In: Magee JS, Mitchell MM, editors. Fluid Catalytic Cracking: Science and Technology, 1993.

Moller P, Jacobsen NR, Folkmann JK, Danielsen PH, Mikkelsen L, Hemmingsen JG, et al. Role of oxidative damage in toxicity of particulates. Free Radical Research 2010; 44: 1-46.

Monteiro-Riviere NA, Wiench K, Landsiedel R, Schulte S, Inman AO, Riviere JE. Safety Evaluation of Sunscreen Formulations Containing Titanium Dioxide and Zinc Oxide Nanoparticles in UVB Sunburned Skin: An In Vitro and In Vivo Study. Toxicological Sciences 2011; 123: 264-280.

Muller J, Huaux Fo, Fonseca A, Nagy JB, Moreau N, Delos M, et al. Structural Defects Play a Major Role in the Acute Lung Toxicity of Multiwall Carbon Nanotubes: Toxicological Aspects. Chemical Research in Toxicology 2008; 21: 1698-1705.

Murdock RC, Braydich-Stolle L, Schrand AM, Schlager JJ, Hussain SM. Characterization of Nanomaterial Dispersion in Solution Prior to In Vitro Exposure Using Dynamic Light Scattering Technique. Toxicological Sciences 2008; 101: 239-253.

Musee N. Nanotechnology risk assessment from a waste management perspective: Are the current tools adequate? Human & Experimental Toxicology 2010.

Mwilu SK, El Badawy AM, Bradham K, Nelson C, Thomas D, Scheckel KG, et al. Changes in silver nanoparticles exposed to human synthetic stomach fluid: Effects of particle size and surface chemistry. Science of The Total Environment 2013; 447: 90-98.

Nabeshi H, Yoshikawa T, Matsuyama K, Nakazato Y, Arimori A, Isobe M, et al. Size-dependent cytotoxic effects of amorphous silica nanoparticles on Langerhans cells. Die Pharmazie - An International Journal of Pharmaceutical Sciences 2010; 65: 199-201.

Nagy A, Steinbruck A, Gao J, Doggett N, Hollingsworth JA, Iyer R. Comprehensive Analysis of the Effects of CdSe Quantum Dot Size, Surface Charge, and Functionalization on Primary Human Lung Cells. Acs Nano 2012; 6: 4748-4762.

Napierska D, Thomassen L, Lison D, Martens J, Hoet P. The nanosilica hazard: another variable entity. Particle and Fibre Toxicology 2010; 7: 1-32.

Nel A, Xia T, Mädler L, Li N. Toxic Potential of Materials at the Nanolevel. Science 2006; 311: 622-627.

Newman MD, Stotland M, Ellis JI. The safety of nanosized particles in titanium dioxide– and zinc oxide–based sunscreens. Journal of the American Academy of Dermatology 2009; 61: 685-692.

Nieuwenhuize J, Maas YEM, Middelburg JJ. Rapid analysis of organic carbon and nitrogen in particulate materials. Marine Chemistry 1994; 45: 217-224.

Nishanth RP, Jyotsna RG, Schlager JJ, Hussain SM, Reddanna P. Inflammatory responses of RAW 264.7 macrophages upon exposure to nanoparticles: Role of ROS-NF kappa B signaling pathway. Nanotoxicology 2011; 5: 502-516.

Nishimori H, Kondoh M, Isoda K, Tsunoda S-i, Tsutsumi Y, Yagi K. Silica nanoparticles as hepatotoxicants. European Journal of Pharmaceutics and Biopharmaceutics 2009; 72: 496-501.

Nowack B, Bucheli TD. Occurrence, behavior and effects of nanoparticles in the environment. Environmental Pollution 2007; 150: 5-22.

Oberdoerster G. Nanotoxicology: in vitro-in vivo dosimetry. Health Perspect 2012; 120: 13.

Oberdorster G, Finkelstein J, Johnston C, Gelein R, Cox C, Baggs R. Acute pulmonary effects of ultrafine particles in rats and mice. Res Rep Health Eff Inst 2000: 5 - 74.

Oberdorster G, Oberdorster E, Oberdorster J. Nanotoxicology: an emerging discipline evolving from studies of ultrafine particles. Environ Health Perspect 2005; 113: 823 - 839.

Oberdörster G, Stone V, Donaldson K. Toxicology of nanoparticles: A historical perspective. Nanotoxicology 2007; 1: 2-25.

OECD. List of manufactured nanomaterials and list of endpoints for phase one of the sponsorship programme for the testing of manufactured nanomaterials: Revision, Paris, 2010, pp. 16.

Ohara S, Adschiri T, Ida T, Yashima M, Mikayama T, Abe H, et al. Chapter 5 - Characterization methods for nanostructure of materials. In: Masuo H, Kiyoshi N, Mario N, ToyokazU YokoyamaA2 - Masuo Hosokawa KNMN, Toyokaz UY, editors. Nanoparticle Technology Handbook. Elsevier, Amsterdam, 2008, pp. 267-315.

Osaki F, Kanamori T, Sando S, Sera T, Aoyama Y. A quantum dot conjugated sugar ball and its cellular uptake. On the size effects of endocytosis in the subviral region. J Am Chem Soc 2004; 126: 6520-6521.

Pacheco S, Medina M, Valencia F, Tapia J. Removal of Inorganic Mercury from Polluted Water Using Structured Nanoparticles. Journal of Environmental Engineering 2006; 132: 342-349.

Panas A, Marquardt C, Nalcaci O, Bockhorn H, Baumann W, Paur HR, et al. Screening of different metal oxide nanoparticles reveals selective toxicity and inflammatory potential of silica nanoparticles in lung epithelial cells and macrophages. Nanotoxicology 2013; 7: 259-273.

Park KH, Chhowalla M, Iqbal Z, Sesti F. Single-walled Carbon Nanotubes Are a New Class of Ion Channel Blockers. THE JOURNAL OF BIOLOGICAL CHEMISTRY 2003; 278: 50212-50216.

Pelaez M, Nolan NT, Pillai SC, Seery MK, Falaras P, Kontos AG, et al. A review on the visible light active titanium dioxide photocatalysts for environmental applications. Applied Catalysis B-Environmental 2012; 125: 331-349.

Peng X, Palma S, Fisher NS, Wong SS. Effect of morphology of ZnO nanostructures on their toxicity to marine algae. Aquatic Toxicology 2011; 102: 186-196.

Petosa AR, Brennan SJ, Rajput F, Tufenkji N. Transport of two metal oxide nanoparticles in saturated granular porous media: Role of water chemistry and particle coating. Water Research 2012; 46: 1273-1285.

Piccinno F, Gottschalk F, Seeger S, Nowack B. Industrial production quantities and uses of ten engineered nanomaterials in Europe and the world. Journal of Nanoparticle Research 2012; 14: 1-11.

Poland CA, Duffin R, Kinloch I, Maynard A, Wallace WAH, Seaton A, et al. Carbon nanotubes introduced into the abdominal cavity of mice show asbestos-like pathogenicity in a pilot study. Nat Nano 2008; 3: 423-428.

Powers KW, Palazuelos M, Moudgil BM, Roberts SM. Characterization of the size, shape, and state of dispersion of nanoparticles for toxicological studies. Nanotoxicology 2007; 1: 42-51.

RA&RAE. Nanoscience and nanotechnologies: opportunities and uncertainties, Carlton House Terrace London SW1Y 5AG, 2004.

Radomski A, Jurasz P, Alonso-Escolano D, Drews M, Morandi M, Malinski T, et al. Nanoparticle-induced platelet aggregation and vascular thrombosis. British Journal of Pharmacology 2005; 146: 882-893.

Rancan F, Gao Q, Graf C, Troppens S, Hadam S, Hackbarth S, et al. Skin Penetration and Cellular Uptake of Amorphous Silica Nanoparticles with Variable Size, Surface Functionalization, and Colloidal Stability. Acs Nano 2012; 6: 6829-6842.

Recillas S, García A, González E, Casals E, Puntes V, Sánchez A, et al. Use of CeO2, TiO2 and Fe3O4 nanoparticles for the removal of lead from water: Toxicity of nanoparticles and derived compounds. Desalination 2011; 277: 213-220.

Regulation(EC)528/2012. REGULATION (EU) No 528/2012 OF THE EUROPEAN PARLIAMENT AND OF THE COUNCIL of 22 May 2012 concerning the making available on the market and use of biocidal products (Text with EEA relevance) [2012] OJ L167/1.

Regulation(EC)1169/2011. REGULATION (EU) No 1169/2011 OF THE EUROPEAN PARLIAMENT AND OF THE COUNCIL of 25 October 2011on the provision of food information to consumers, amending Regulations (EC) No 1924/2006 and (EC) No 1925/2006 of the European Parliament and of the Council, and repealing Commission Directive 87/250/EEC, Council Directive 90/496/EEC, Commission Directive 1999/10/EC, Directive 2000/13/EC of the European Parliament and of the Council, Commission Directives 2002/67/EC and 2008/5/EC and Commission Regulation (EC) No 608/2004 (Text with EEA relevance) [2011] OJ L 304/18.

Regulation(EC)1223/2009. REGULATION (EC) No 1223/2009 OF THE EUROPEAN PARLIAMENT AND OF THE COUNCIL of 30 November 2009 on cosmetic products (recast) (Text with EEA relevance) [2009] OJ L 342/59.

Robichaud CO, Uyar AE, Darby MR, Zucker LG, Wiesner MR. Estimates of Upper Bounds and Trends in Nano-TiO2 Production As a Basis for Exposure Assessment. Environmental Science & Technology 2009; 43: 4227-4233.

Roduner E. Size matters: why nanomaterials are different. Chemical Society Reviews 2006; 35: 583-592.

Rosi NL, Mirkin CA. Nanostructures in biodiagnostics. Chemical Reviews 2005; 105: 1547-1562.

Saeed K. Review on Properties, Dispersion and Toxicology of Carbon Nanotubes. Journal of the Chemical Society of Pakistan 2010; 32: 559-564.

Sahana DK, Mittal G, Bhardwaj V, Kumar M. PLGA nanoparticles for oral delivery of hydrophobic drugs: Influence of organic solvent on nanoparticle formation and release Behavior in vitro and in vivo using estradiol as a model drug. Journal of Pharmaceutical Sciences 2008; 97: 1530-1542.

Samanta B, Yan H, Fischer NO, Shi J, Jerry DJ, Rotello VM. Protein-passivated Fe3O4 nanoparticles: low toxicity and rapid heating for thermal therapy. Journal of Materials Chemistry 2008; 18: 1204-1208.

SCENIHR. Opinion on the scientific aspects of the existing and proposed definitions relating to products of nanoscience and nanotechnologies, Brussels, Belgium, 2007.

Schaefer H-E. Nanoscience - The Science of the Small in Physics, Engineering, Chemistry, Biology and Medicine. Vol XXIII, 2010.

Schiestel T, Brunner H, Tovar GE. Controlled Surface Functionalization of Silica Nanospheres by Covalent Conjugation Reactions and Preparation of High Density Streptavidin Nanoparticles. Journal of Nanoscience and Nanotechnology 2004; 4: 504-511.

Schmid G. Large clusters and colloids. Metals in the embryonic state. Chemical Reviews 1992; 92: 1709-1727.

Shah V, Shah S, Shah H, Rispoli FJ, McDonnell KT, Workeneh S, et al. Antibacterial activity of polymer coated cerium oxide nanoparticles. PLoS One 2012; 7: e47827-e47827.

Sharifi S, Behzadi S, Laurent S, Laird Forrest M, Stroeve P, Mahmoudi M. Toxicity of nanomaterials. Chemical Society Reviews 2012; 41: 2323-2343.

Shvedova AA, Kagan VE, Fadeel B. Close Encounters of the Small Kind: Adverse Effects of Man-Made Materials Interfacing with the Nano-Cosmos of Biological Systems. Annual Review of Pharmacology and Toxicology 2010; 50: 63-88.

Šiller L, Lemloh M-L, Piticharoenphun S, Mendis BG, Horrocks BR, Brümmer F, et al. Silver nanoparticle toxicity in sea urchin Paracentrotus lividus. Environmental Pollution 2013; 178: 498-502.

Singh LP, Karade SR, Bhattacharyya SK, Yousuf MM, Ahalawat S. Beneficial role of nanosilica in cement based materials – A review. Construction and Building Materials 2013; 47: 1069-1077.

Sohaebuddin SK, Thevenot PT, Baker D, Eaton JW, Tang L. Nanomaterial cytotoxicity is composition, size, and cell type dependent. Particle and Fibre Toxicology 2010; 7.

Som C, Berges M, Chaudhry Q, Dusinska M, Fernandes TF, Olsen SI, et al. The importance of life cycle concepts for the development of safe nanoproducts. Toxicology 2010; 269: 160-169.

Stone V, Nowack B, Baun A, van den Brink N, von der Kammer F, Dusinska M, et al. Nanomaterials for environmental studies: Classification, reference material issues, and strategies for physico-chemical characterisation. Science of The Total Environment 2010; 408: 1745-1754.

Sun Y-N, Wang C-D, Zhang X-M, Ren L, Tian X-H. Shape Dependence of Gold Nanoparticles on In Vivo Acute Toxicological Effects and Biodistribution. Journal of Nanoscience and Nanotechnology 2011; 11: 1210-1216.

Suresh AK, Pelletier DA, Doktycz MJ. Relating nanomaterial properties and microbial toxicity. Nanoscale 2013; 5: 463-474.

Suresh AK, Pelletier DA, Wang W, Morrell-Falvey JL, Gu B, Doktycz MJ. Cytotoxicity Induced by Engineered Silver Nanocrystallites Is Dependent on Surface Coatings and Cell Types. Langmuir 2012; 28: 2727-2735.

Sýkora D, Kašička V, Mikšík I, Řezanka P, Záruba K, Matějka P, et al. Application of gold nanoparticles in separation sciences. Journal of Separation Science 2010; 33: 372-387.

Tagmatarchis N, Shinohara H. Fullerenes in medicinal chemistry and their biological applications. Mini reviews in medicinal chemistry 2001; 1: 339-48.

Tan CW, Tan KH, Ong YT, Mohamed AR, Zein SHS, Tan SH. Energy and environmental applications of carbon nanotubes. Environmental Chemistry Letters 2012; 10: 265-273.

Tang F, Li L, Chen D. Mesoporous Silica Nanoparticles: Synthesis, Biocompatibility and Drug Delivery. Advanced Materials 2012; 24: 1504-1534.

Teja AS, Koh P-Y. Synthesis, properties, and applications of magnetic iron oxide nanoparticles. Progress in Crystal Growth and Characterization of Materials 2009; 55: 22-45.

Thurn KT, Arora H, Paunesku T, Wu A, Brown EM, Doty C, et al. Endocytosis of titanium dioxide nanoparticles in prostate cancer PC-3M cells. Nanomedicine : nanotechnology, biology, and medicine 2011; 7: 123-130.

Tiwari P, Vig K, Dennis V, Singh S. Functionalized Gold Nanoparticles and Their Biomedical Applications. Nanomaterials 2011; 1: 31-63.

Unfried K, Albrecht C, Klotz L-O, Von Mikecz A, Grether-Beck S, Schins RPF. Cellular responses to nanoparticles: Target structures and mechanisms. Nanotoxicology 2007; 1: 52-71.

USEPA. State of the Science Literature Review: Nano Titanium Dioxide Environmental Matters, Washington DC, 2010.

Wallin H, Saber AT, Koponen IK, Jensen KA, Vogel U. Nanomaterials in the life cycle. Mutagenesis 2012; 27: 795-796.

Wang S, Lu W, Tovmachenko O, Rai US, Yu H, Ray PC. Challenge in understanding size and shape dependent toxicity of gold nanomaterials in human skin keratinocytes. Chemical Physics Letters 2008; 463: 145-149.

Warheit DB, Sayes CM, Reed KL, Swain KA. Health effects related to nanoparticle exposures: Environmental, health and safety considerations for assessing hazards and risks. Pharmacology & Therapeutics 2008; 120: 35-42.

Weinberg H, Galyean A, Leopold M. Evaluating engineered nanoparticles in natural waters. TrAC Trends in Analytical Chemistry 2011; 30: 72-83.

Weir A, Westerhoff P, Fabricius L, Hristovski K, von Goetz N. Titanium Dioxide Nanoparticles in Food and Personal Care Products. Environmental Science & Technology 2012; 46: 2242-2250.

Werth JH, Linsenbühler M, Dammer SM, Farkas Z, Hinrichsen H, Wirth KE, et al. Agglomeration of charged nanopowders in suspensions. Powder Technology 2003; 133: 106-112.

Wick P, Manser P, Limbach LK, Dettlaff-Weglikowska U, Krumeich F, Roth S, et al. The degree and kind of agglomeration affect carbon nanotube cytotoxicity. Toxicology Letters 2007; 168: 121-131.

Wiesner MR, Lowry GV, Jones KL, Hochella JMF, Di Giulio RT, Casman E, et al. Decreasing Uncertainties in Assessing Environmental Exposure, Risk, and Ecological Implications of Nanomaterials†‡. Environmental Science & Technology 2009; 43: 6458-6462.

Wu W, Sun Z, Zhang Y, Xu J, Yu H, Liu X, et al. A multifunctional nanosensor based on silica nanoparticles and biological applications in living cells. Chemical Communications 2012; 48: 11017-11019.

Xu M, Fujita D, Kajiwara S, Minowa T, Li X, Takemura T, et al. Contribution of physicochemical characteristics of nano-oxides to cytotoxicity. Biomaterials 2010; 31: 8022-8031.

Yacobi NR, Phuleria HC, Demaio L, Liang CH, Peng C-A, Sioutas C, et al. Nanoparticle effects on rat alveolar epithelial cell monolayer barrier properties. Toxicology in Vitro 2007; 21: 1373-1381.

Yeh Y-C, Creran B, Rotello VM. Gold nanoparticles: preparation, properties, and applications in bionanotechnology. Nanoscale 2012; 4: 1871-1880.

Yokel R, MacPhail R. Engineered nanomaterials: exposures, hazards, and risk prevention. Journal of Occupational Medicine and Toxicology 2011; 6: 7.

Zhang Y, Bai Y, Yan B. Functionalized carbon nanotubes for potential medicinal applications. Drug Discovery Today 2010; 15: 428-435.

Zhang Y, Chen Y, Westerhoff P, Crittenden J. Impact of natural organic matter and divalent cations on the stability of aqueous nanoparticles. Water Research 2009; 43: 4249-4257.

Zhang YA, Xu D, Li WQ, Yu J, Chen Y. Effect of Size, Shape, and Surface Modification on Cytotoxicity of Gold Nanoparticles to Human HEp-2 and Canine MDCK Cells. Journal of Nanomaterials 2012.

Zuin S, Scanferla P, Brunelli A, Marcomini A, Wong JE, Wennekes W, et al. Layer-by-Layer Deposition of Titanium Dioxide Nanoparticles on Polymeric Membranes: A Life Cycle Assessment Study. Industrial & Engineering Chemistry Research 2013.

ANNEX 1

Primary characterization results

TiO_2 NRCWE-002

NM-Source: NRCWE, Copenhagen, Denmark
Producer/Vender: NanoAmor (modified by NRCWE, Copenhagen, Denmark)
Content: Titanium dioxide nanopowder
Coating: positively charge coating (tri-ethoxypropylaminosilane)
Appearance: White, ultrafine powder

Phase composition

Rutile was the only crystalline phase (62 w%) detected in NRCWE-002. The sample contains a higher fraction of amorphous material (38 w%) than the precursor NRCWE-001, consistent with surface modification (Fig. A1-1).

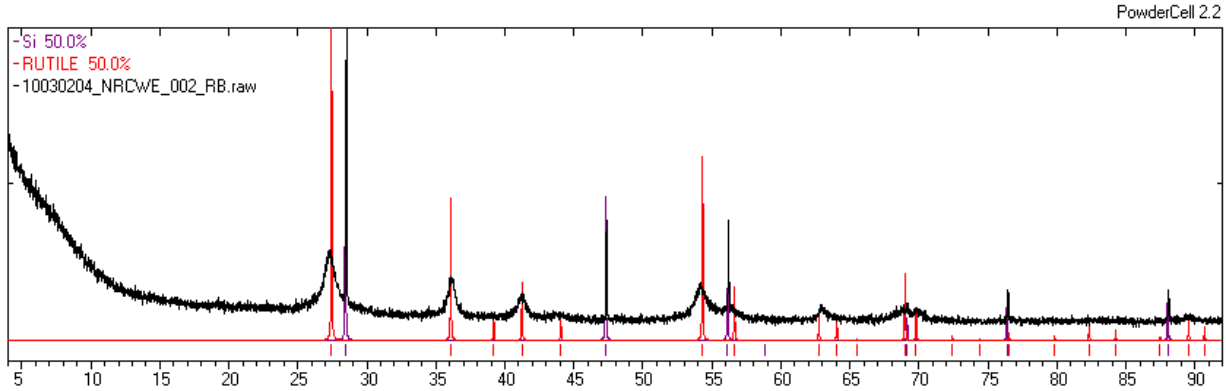

Fig. A1-1 – X-ray powder diffraction data showing the presence of rutile and the dopant silicon.

Particle Size and Morphology

According to NRCWE-001, XRD analyses highlight a crystallite size of 10±1 nm. SEM analysis showed presence of agglomerates with irregular shape from a 0.1 to approx. 100 µm, with a slight predominance of 8-15 µm size agglomerates (Figs A1-2a and b). By inspection of TEM images, an average size range for 80% particles from 80 to 400 nm was observed, with no appreciable predominant size, similar to NRCWE-001 (Figs. A1-2c and d).

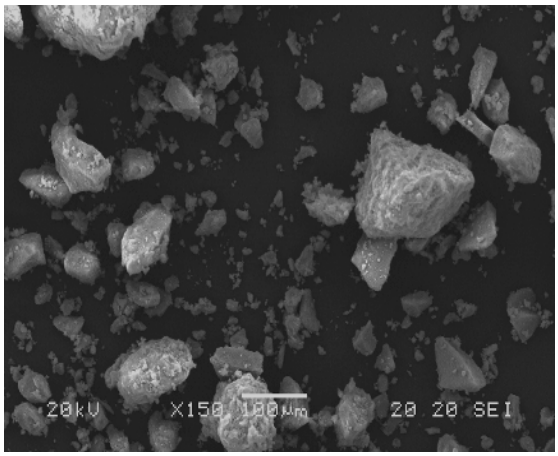

a)

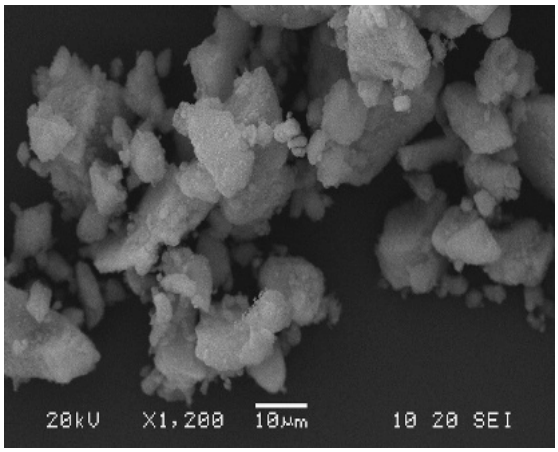

b)

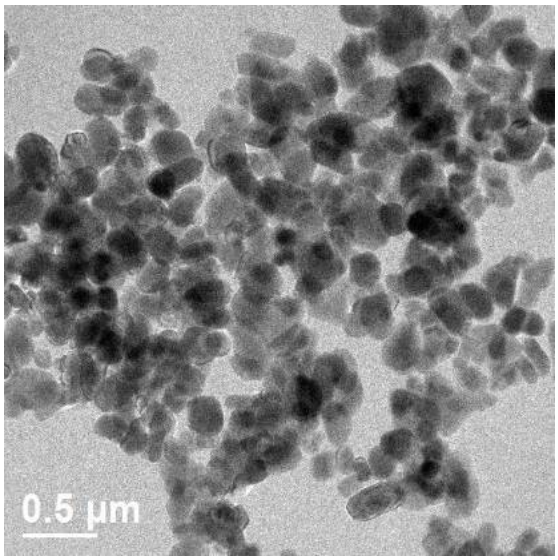

c)

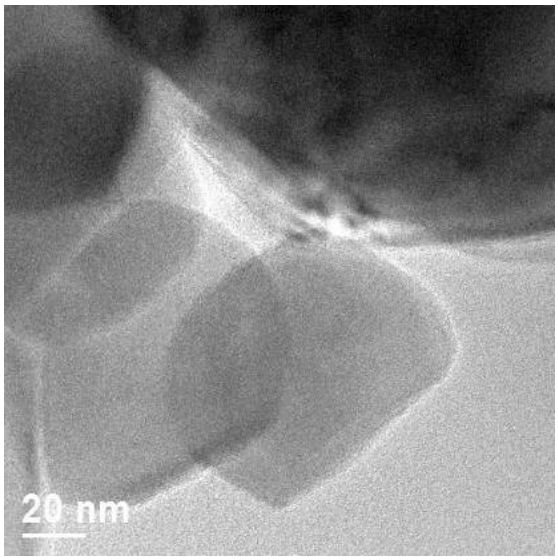

d)

Fig. A1-2 – EM images of NRCWE-002: a) Large polyhedral agglomerates; b) Close-up showing a wide agglomerate-aggregate size range; c) Typical agglomerates and aggregates of euhedral and subhedral rutile crystallites; d) High magnification showing small nm-size polyhedral particles.

BET Surface and area porosity

Specific surface area was 84.3±0.5 m^2/g

Elemental analysis

Inorganic impurities detected by ICP-OES are reported in Table A1-1. No individual impurity particles or crystal structures of the identified elements were identified by TEM-EDX.

Table A1-1 – Trace elements impurities detected in NRCWE 002.

Element	**µg/g**	**µg/g (LOD)**
Co	758±32	0.1
Fe	161±12	0.1
Cr	40±1.8	0.3
V	5.1±0.9	0.1
Zn	4.1±3.1	0.2
Mn	2.3±0.2	0.01

TiO_2 NRCWE-003

NM-Source: NRCWE, Copenhagen, Denmark
Vender: NanoAmor (modified by NRCWE, Copenhagen, Denmark)
Content: titanium dioxide nanopowder
Coating: negatively charge coating (capryl-amine)
Apperance: White, ultrafine powder

Phase composition

Rutile was the only crystalline phase (70 w%) detected in NRCWE-003. Similar to NRCWE-002, the sample contains a higher fraction of amorphous material (30 w%) than the precursor NRCWE-001, which is consistent with surface modification (Fig. A1-3).

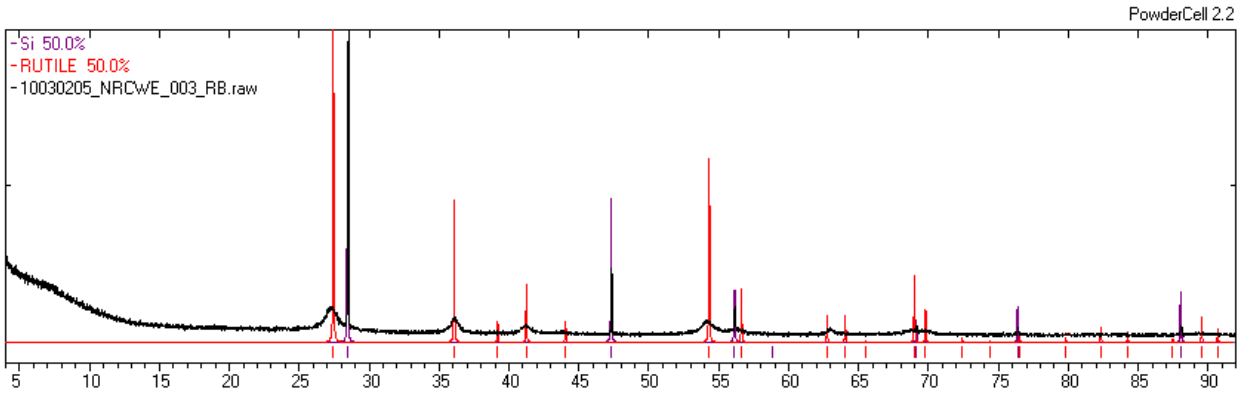

Fig. A1-3 – X-ray powder diffraction data showing the presence of rutile and the dopant silicon.

Particle size and morphology

According to the previous sample NRCWE-001, XRD analyses highlight a crystallite size of 10±1 nm. SEM analysis showed presence of mainly dense agglomerates with irregular shapes and sizes up to approx. 150 µm. There was no clear size predominance (Fig A1-4a). By observing TEM images, the sample is constituted of irregular polyhedral particles (Figs. A1-4b and c). EM images allowed detecting an average size range for 80% particles between 80 to 400 nm, with no appreciable predominant size, similar to NRCWE-001.

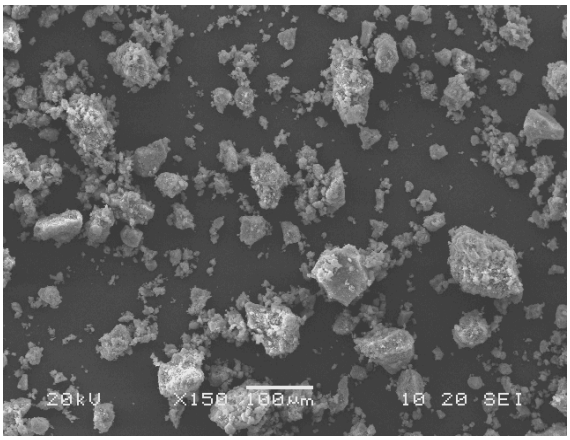

a)

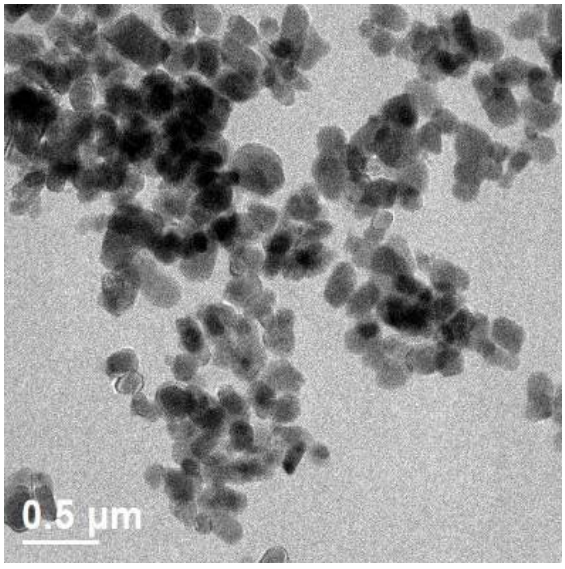

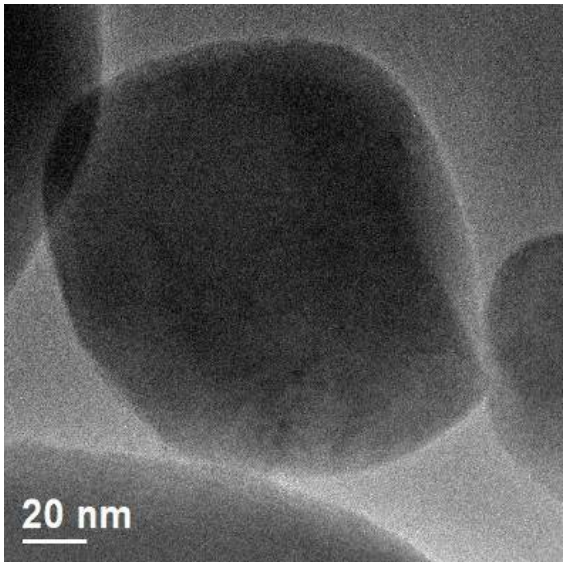

b) c)

Fig. A1-4 – a) SEM image showing large agglomerates, up to 150 µm; b) Typical TEM image of NRCWE-003 with some agglomerates; c) High magnification showing a typical polyhedral particle.

BET Surface area

Specific surface area was 84.2±0.5 m^2/g.

Elemental analysis

Some inorganic impurities were detected by ICP-OES (Table A1-2). No individual impurity particles or crystal structures of the identified elements were identified by TEM-EDX.

Table A1-2 – Trace elements impurities found in NRCWE-003.

Element	**µg/g**	**µg/g (LOD)**
Co	762±33	0.1
Fe	155±9	0.1
Cr	42±1.7	0.3
V	4.9±1	0.1
Zn	4.3±3.1	0.2
Mn	2±1.9	0.01

TiO_2 NRCWE-004

NM-Source: NRCWE, Copenhagen, Denmark
Vender: NaBond
Content: titanium dioxide nanopowder
Coating : none (from supplier)
Appearance: White, ultrafine powder

Phase composition

X-ray diffraction analysis shows that rutile is the only crystalline material (44 w%) in NRCWE-004 (Fig. A1-5). The concentration of amorphous material was relatively high (56 w%).

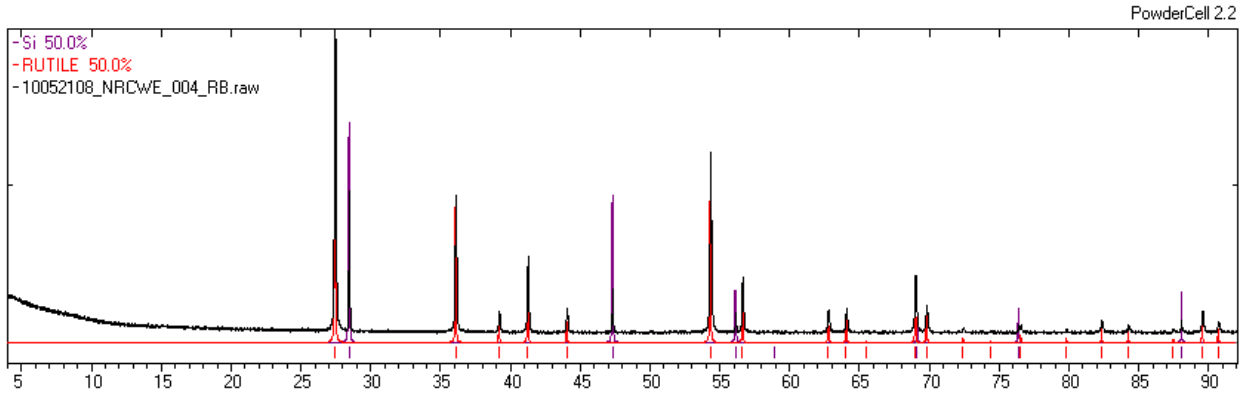

Fig. A1-5 – X-ray powder diffraction data showing the presence of rutile and the dopant silicon.

Particle Size and Morphology

XRD analyses highlight a crystallite size of 94±12 nm. SEM images showed that most powder particles consisted of large agglomerates with irregular shape from 0.5 µm up to approx. 300 µm, with a slight predominance of agglomerates between 15 and 30 µm size range (Figs. A1-5a and b). Approximately 90% of particles is in the 10-2000 nm range. Observing TEM images at different magnifications, different sizes (from a few nanometers to µm) and morphologies were identified (Figs. A1-6c to f).

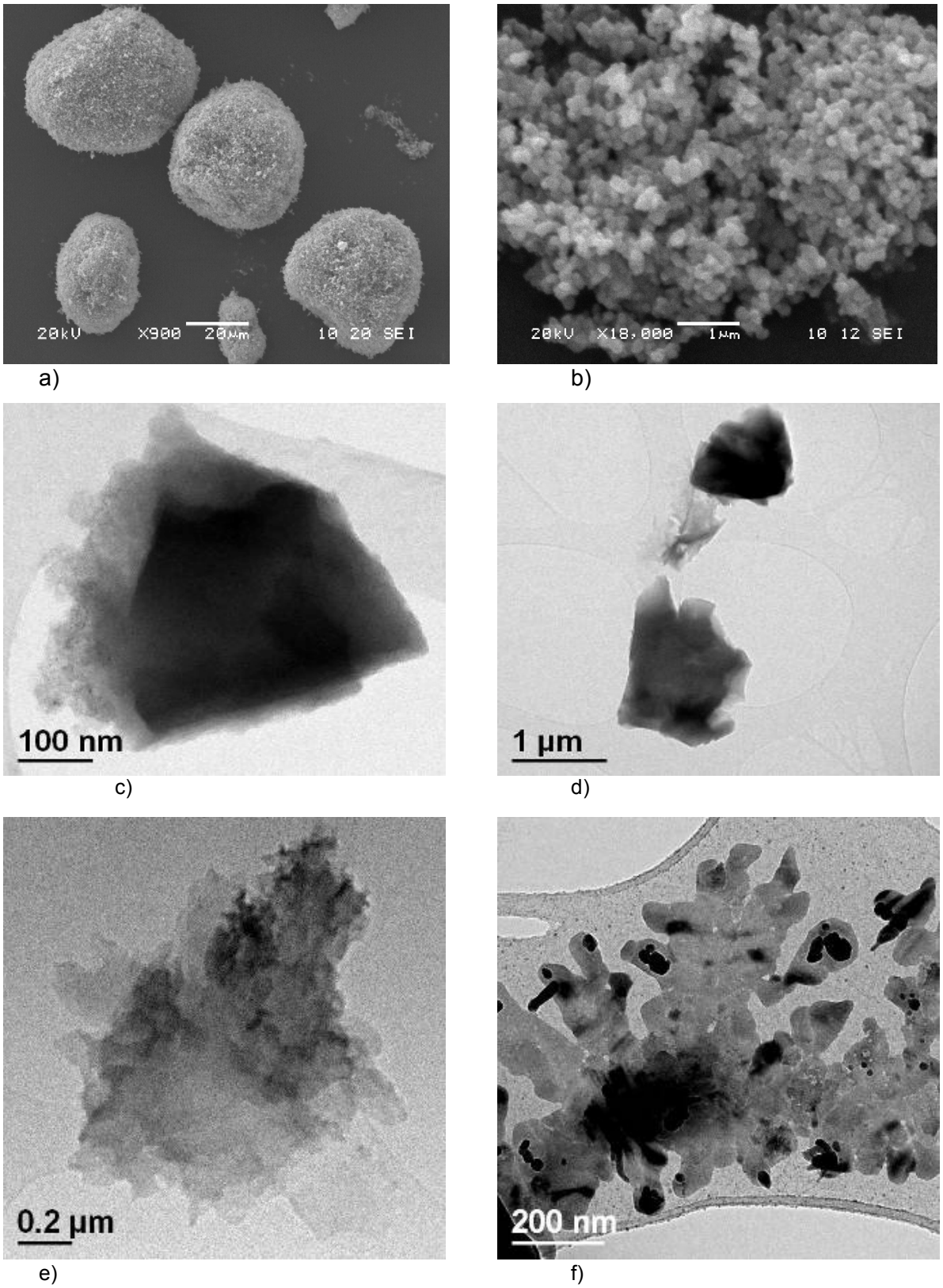

Fig. A1-6 – a) TEM-image showing a large-size angular TiO_2 particle; b) TEM image of fractal-like flake; c) TEM image of a small-size angular particle; d) TEM image showing a mixture of morphologies detected, including several sizes in the range between few nm to approx. 200 nm.

BET Surface area

Specific surface area was 5.1 m^2/g

Elemental analysis

Some inorganic impurities were detected by ICP-OES (Table A1-3). No individual impurity particles or crystal structures of the identified elements were identified by TEM-EDX.

Table A1-3 – Trace elements impurities detected in NRCWE 004.

Element	**µg/g**	**µg/g (LOD)**
Co	877±24	0.1
Cr	66±3	0.3
Mn	45±1.2	0.01
Pb	24±12	0.04
Zn	5±5	0.2

TiO_2 NM-101

NM-Source: Joint Research Centre, Ispra, Italy
Producer/Vender: Sachtleben Chemie, GmBH
Content: Titanium dioxide nanopowder
Coating : None (from supplier)
Appearance: White, ultrafine powder

Phase composition

X-ray diffraction analysis shows that NM-101 is composed of half anatase (48 w%) and of half (51 w%) amorphous. Rutile may be present as a minor fraction (1 w%) (Fig. A1-7).

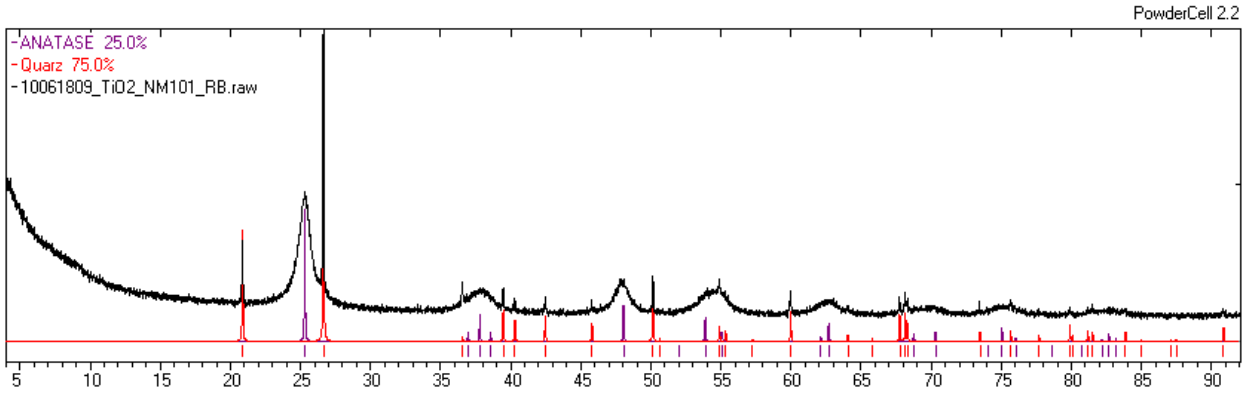

Fig. A1-7 – X-ray powder diffractograms of NM-101 showing anatase and the dopant quartz.

Particle Size and Morphology

XRD analyses highlight a crystallite size of 8±1 nm. SEM images showed that the powder consisted of agglomerates with irregular shape with sizes ranging from a few nm to approx. 5 µm (Figs. A1-8a and b). The average aggregate and/or agglomerate size was around 1 µm. Observing TEM images at different magnifications, aggregates were clearly identified, ranging from 50 to 1500 nm (Figs. A1-8c to e), with irregular shape and also minor amounts of fibers. The aggregates are highly porous and appear as sponge-like particles with ellipsoidal voids. This can be seen at high resolution (A1-8e). Minor free single crystals and small aggregates were also observed.

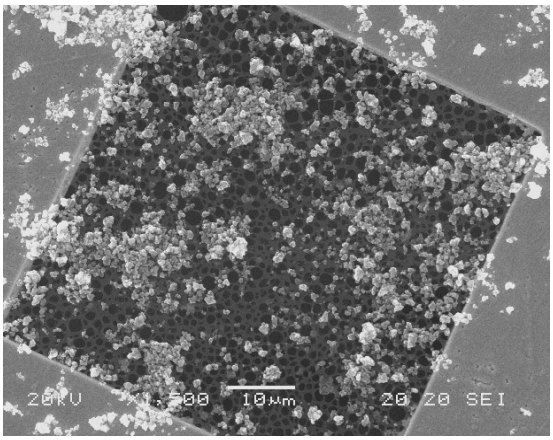

a)

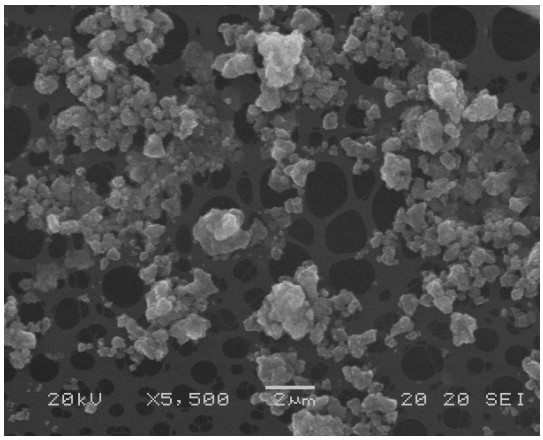

b)

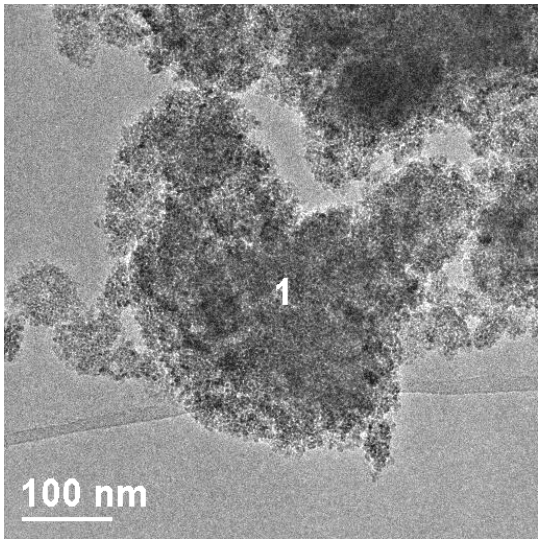

c)

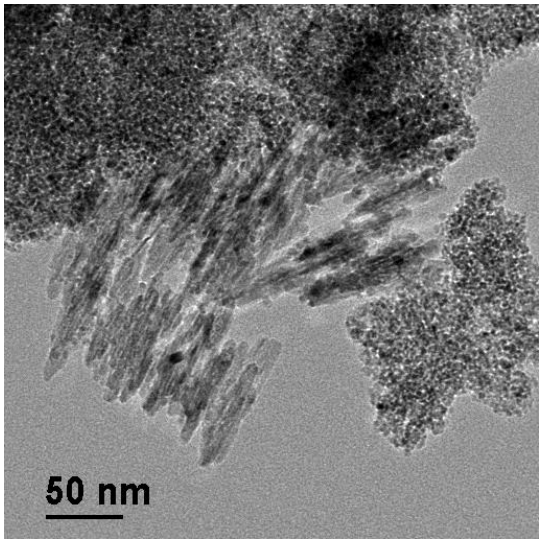

d)

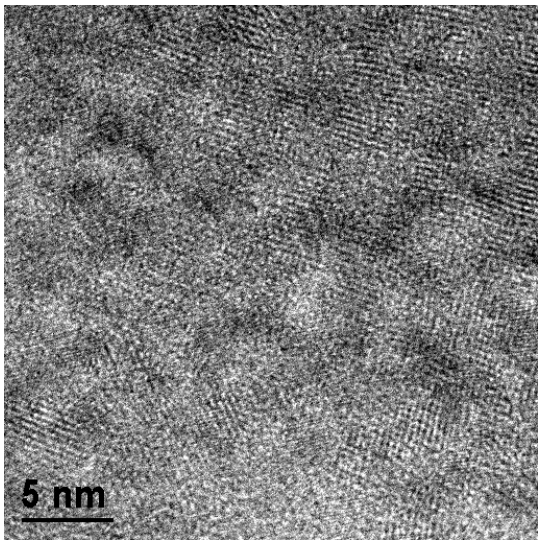

e)

Fig. A1-8 – a) SEM image showing large aggregates and agglomerates; b) close-up of TiO_2 sample highlighting aggregates and agglomerates up to approx. 2 µm; c) typical porous aggregates; d) typical fibrous TiO_2 particles; e) porous TiO_2 particles at higher magnification

BET Surface area

Specific surface area was 322±2 m^2/g.

Elemental analysis

Some inorganic impurities were detected by ICP-OES (Table A1-4). No individual impurity particles or crystal structures of the identified elements were identified by TEM-EDX.

Table A1-4 – Trace elements impurities detected in NM-101.

Element	**µg/g**	**µg/g (LOD)**
Co	921±37	0.1
Cr	53±9	0.3
Fe	36±11	0.1
V	6±2	0.1
Zn	5.2±1.7	0.2
Mn	1.5±0.6	0.01

TiO_2 P25

NM-Source: Joint Research Centre, Ispra, Italy
Producer/Vender: Evonik Degussa, GmBH
Content: Titanium dioxide nanopowder
Coating: None (from supplier)
Appearance: White, ultrafine powder

Phase composition

Fig. A1-9 shows the phase composition of P25. Anatase was the predominant phase (86.5 w%) detected in P25. The sample is also constituted by some rutile crystallites (13.5 w%). No amorphous material was detected.

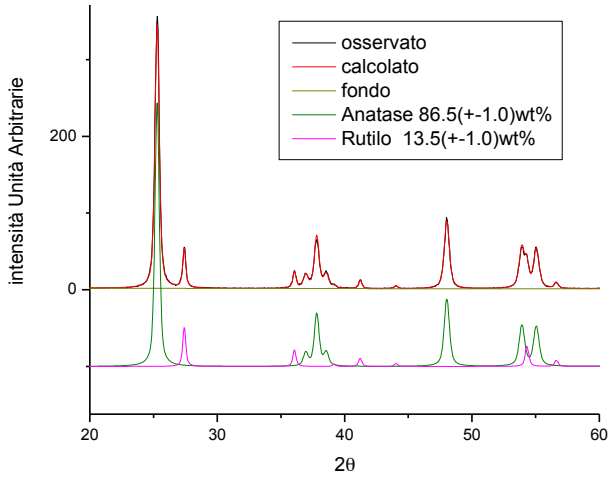

Fig. A1-9 – X-ray powder diffraction data showing the presence of anatase and rutile of P25.

Particle size and morphology

From 150 HR-TEM pictures, the average size of particles was 27 nm, with a size range between 15 and 47 nm for approx. 90 % of particles (Fig. A1-10).

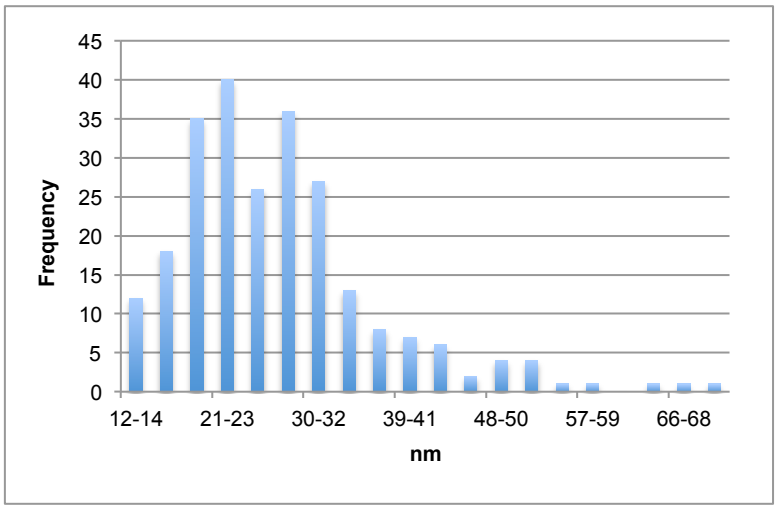

Fig. A1-10 – P25 size distribution measured by HR-TEM.

HR-TEM images showed presence of agglomerates with irregular shape up to approx. 100 nm. The individual crystallites were in a polyhedron shape (Fig. A1-11).

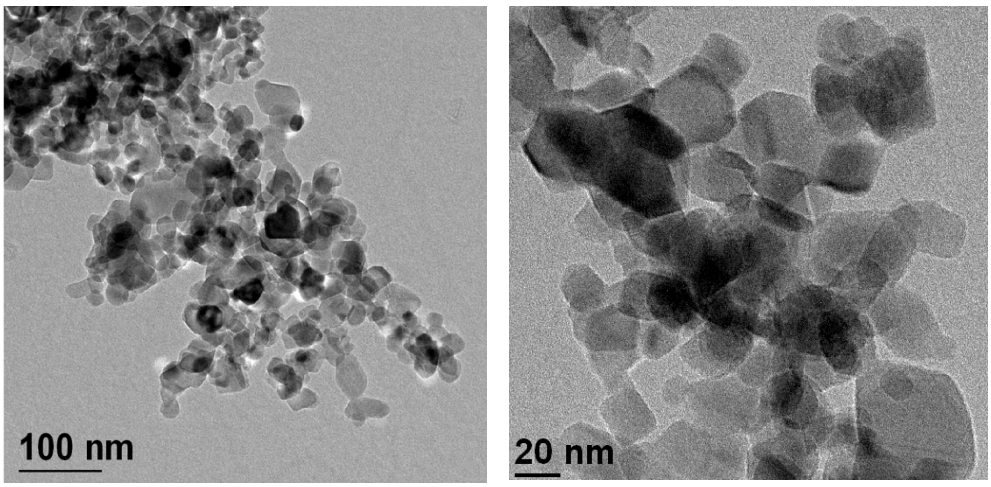

a) b)

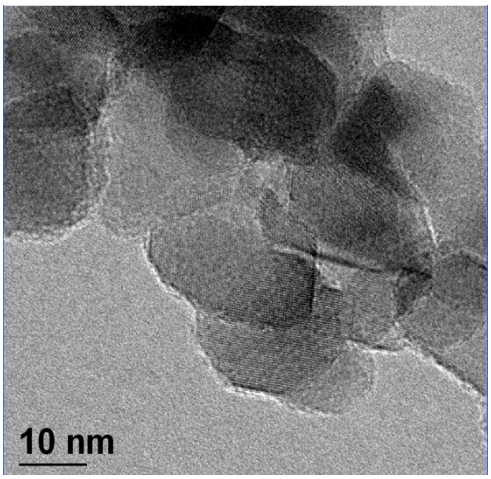

c)

Fig. A1-11 – Typical HR-TEM images of P25: a) Agglomerates up to approx. 100 nm; b) Close-up showing polyhedral structure; c) High magnification showing small nm-size particles.

BET Surface area

Specific surface area was 54±0.4 m^2/g.

Elemental analysis

Some inorganic impurities were detected by ICP-OES (Table A1-5). No individual impurity particles or crystal structures of the identified elements were identified by TEM-EDX.

Table A1-5 – Trace elements impurities detected in P25.

Element	µg/g	µg/g (LOD)
Mg	323±57	0.01
Na	24±6	0.2

ZnO NM-110

NM-Source: JRC, Ispra, Italy
Producer/Vender: BASF Z-Cote
Content: zinc oxide nanopowder
Coating : none (from supplier)
Appearance: White, ultrafine powder

Phase composition

X-ray diffraction analyses suggest that all crystalline material is made by zincite (52 w%) (Fig. A1-12). The amorphous fraction amounted to 48% of the sample.

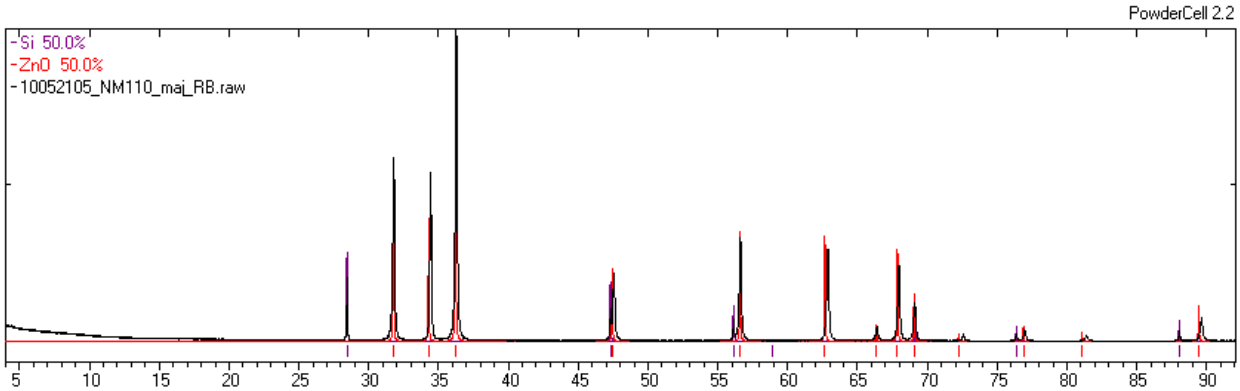

Fig. A1-12 – X-ray powder diffraction data showing the presence of zincite and dopant silicon.

Particle size and morphology

XRD analyses highlight a crystallite size of 71 nm. TEM images showed irregular compact to partially open agglomerates or aggregates from few µm up to 0.2 µm in size (Fig. A1-13a). The primary ZnO crystals are polyhedral with quite variable morphology (Figs. A1-13a to d). Two main clusters of particles could be distinguished: i) particles with aspect ratio close to 1 (typically 20 – 250 nm size and very few particles of approx. 400 nm size) and hexagonal morphology; ii) particles with aspect ratio 2 to 7.5 (50 – 350 nm) with cubic, tetragonal and orthorhombic morphologies.

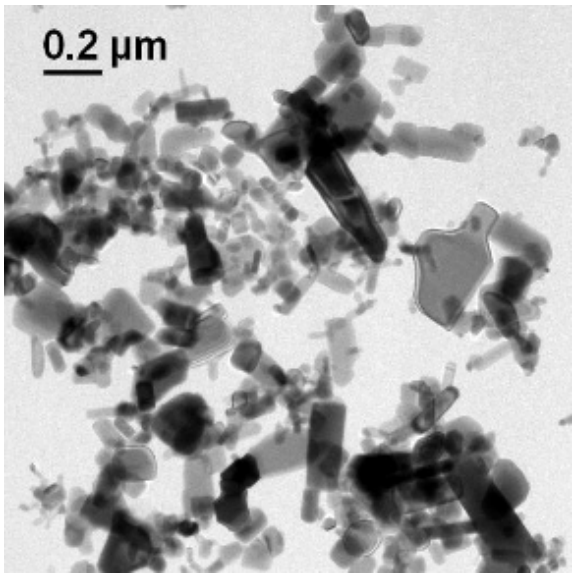

a)

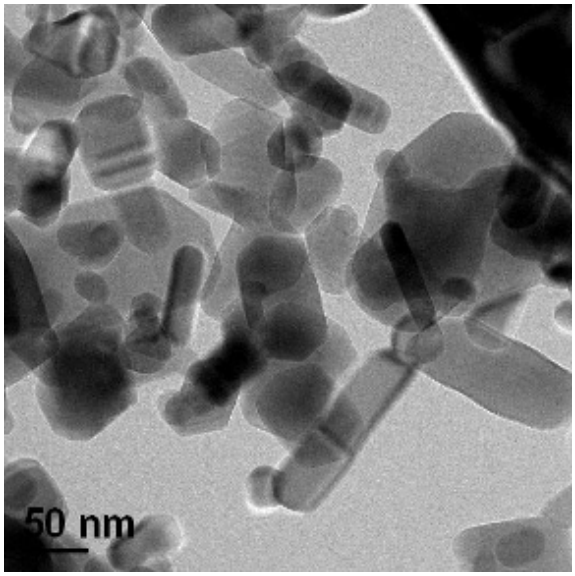

b)

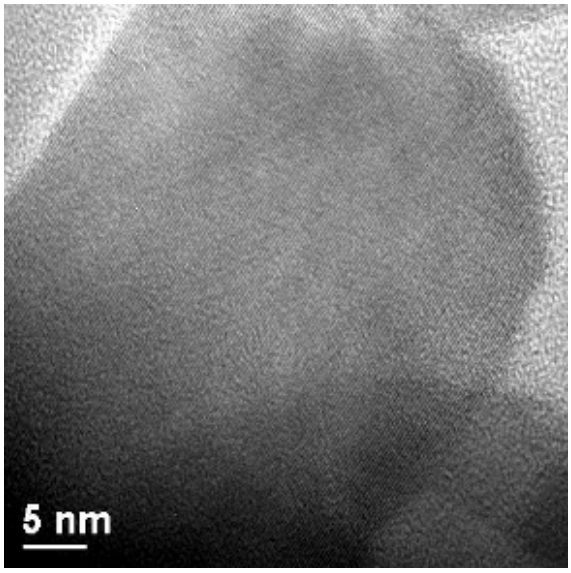

c)

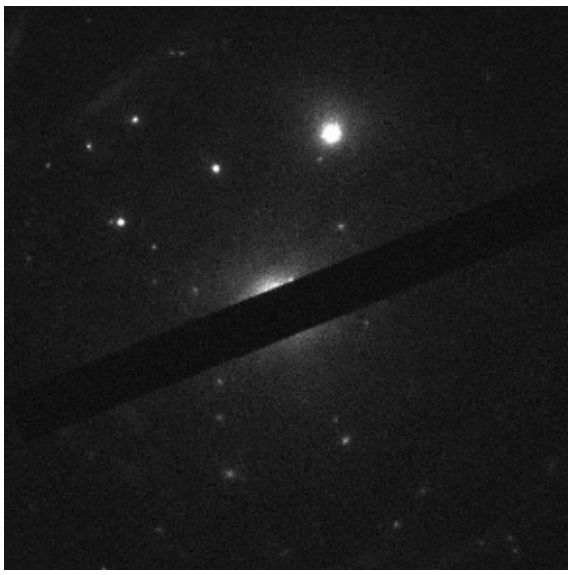

d)

Fig. A1-13 – a) TEM-image showing the coarse particle size variation and their agglomerated/aggregated structure. b) High-magnification TEM-image showing the size-range and morphological variation of small ZnO crystallites. c) High-resolution image showing the structure of zincite crystallites. e) Electron diffraction patters showing the presence of large (bright single spots) crystallites in the sample.

BET Surface area

Specific surface are was 14±0.1 m^2/g

Elemental analysis

Very low inorganic trace element impurities were detected by ICP-OES (Table A1-6). No individual impurity particles or crystal structures of the identified elements were identified by TEM-EDX.

Table A1-6 – Trace elements impurities detected in NM-110.

Element	**µg/g**	**µg/g (LOD)**
Ni	9±6	0.1
Pb	8±5	0.03
Co	3±2	0.1

ZnO NM-111

NM-Source: JRC, Ispra, Italy
Producer/Vender: BASF Z-Cote
Content: zinc oxide nanopowder
Coating : triethoxyca-prylylsilane 130 (from supplier)
Appearance: White, ultrafine powder

Phase composition

X-ray diffraction analysis suggest that almost all if not all crystalline material is zincite (34%) (Fig. A1-14). The X-ray amorphous fraction may comprise approximately 66% of the sample.

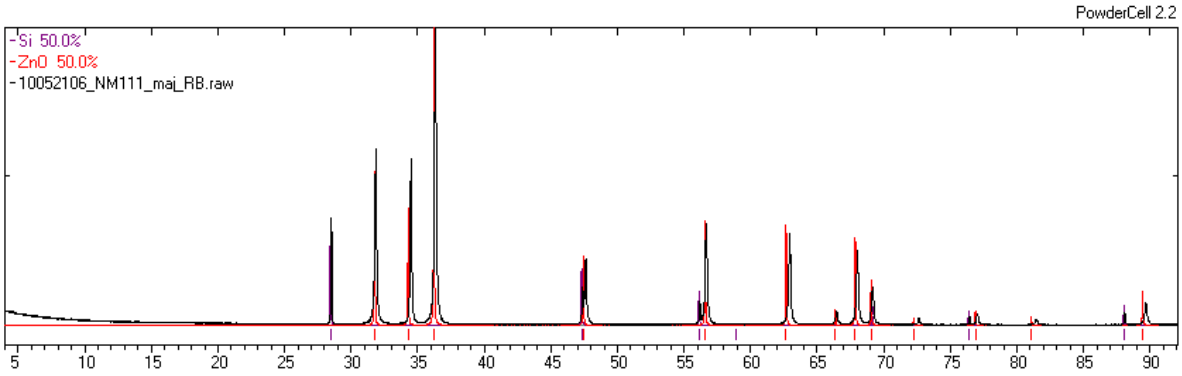

Fig. A1-14 - X-ray powder diffraction data showing the presence of zincite and the dopant silicon.

Particle size and morphology

XRD analyses highlight a crystallite size of 58 nm. By SEM, NM-111 consisted of massive to partially open agglomerates or aggregates from 0.1 µm up to a few µm in size. No predominant agglomerates sizes could be identified (Figs. A1-15a-b).

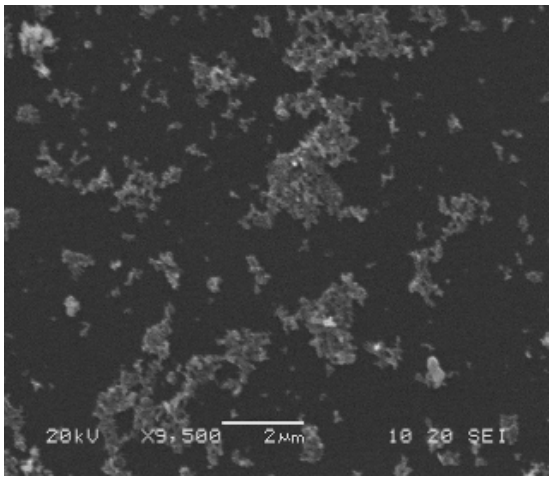

a)

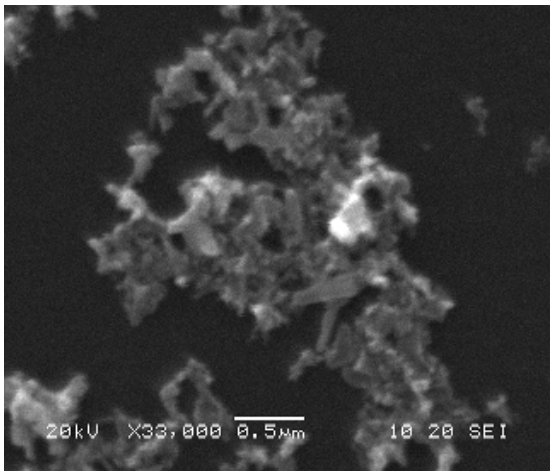

b)

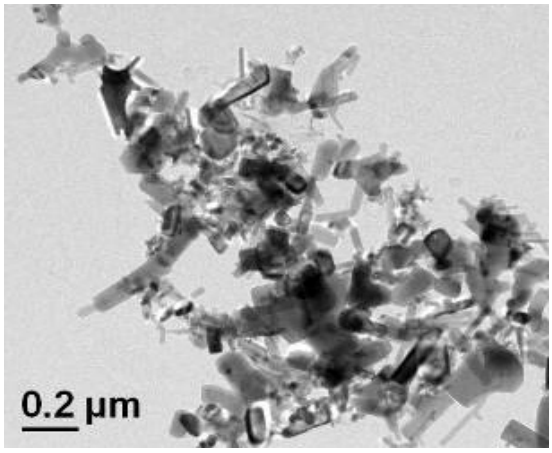

c)

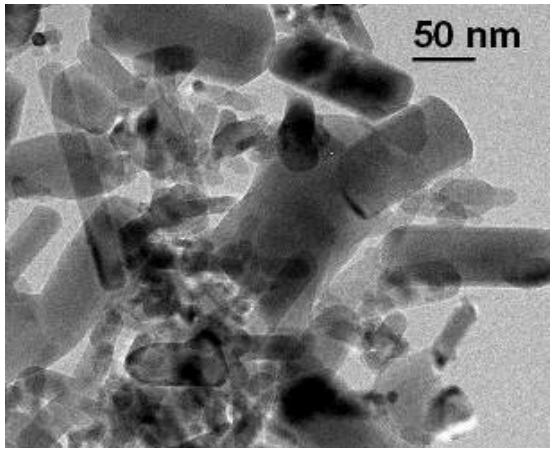

d)

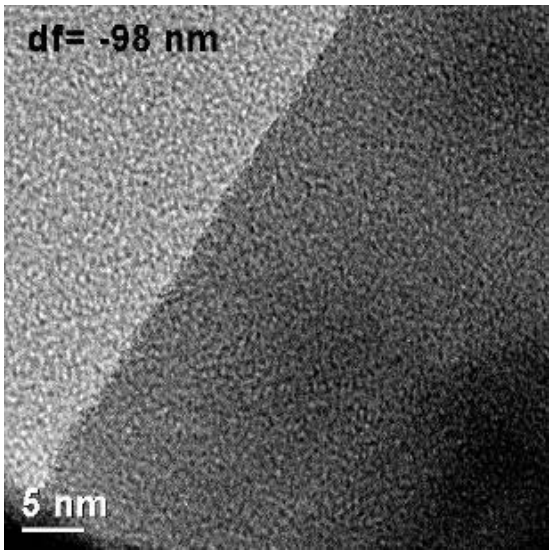

e)

Fig. A1-15 - Electron microscopy images of NM-111: a) SEM-images illustrating the wide size-distribution of the ZnO aggregates/agglomerates; b) SEM-image showing an example of the general aggregate/agglomerate structure and variable zincite morphology; c) TEM-image showing the

agglomerated aggregate structure of particles. d) High-magnification TEM-image showing the large size-range of ZnO crystallites. e) High-resolution image showing partially amorphous crystallite

By TEM, the primary particles appeared polyhedral and with variable morphology as observed in NM-110, but with different size distributions (Figs. A1-15c-e). Two main morphological types could be distinguished: (i) particles with aspect ratio close to 1 (~90% in the 20 – 200 nm range); (ii) particles with aspect ratio 2 to 8.5 (~90% in the 10 – 450 nm range).

BET surface area and porosity

Specific surface area was 18 (±0.1) m^2/g. The Specific pore volume was determined to be 0.1 ml/g.

Elemental analysis

Very low inorganic trace element impurities were detected by ICP-OES (Table A1-7). No individual impurity particles or crystal structures of the identified elements were identified by TEM-EDX.

Table A1-7 – Trace element impurities detected in NM-111.

Element	µg/g	µg/g (LOD)
Ni	9±4	0.1
Pb	8±2	0.03
Co	3±2	0.1

Ag NM-300

NM-Source: JRC, Ispra, Italy
Producer/Vender: RAS GmbH
Supplier code: NM-300
Content: Ag (10.16%, w:w) in aqueous dispersion, with stabilizers (4% polyethoxyethylene glycerol trioleate; 4% polyethoxylene (20) sorbitan mono-laurat - Tween 20)
Coating : No further information (from supplier)
Appearance: dark brown dispersion, usually with black/brown solid sediment in the vial. Both NM-300 and NM-300K has a problem with sedimentation.

Phase composition

X-ray diffraction analysis suggest that almost all if not all crystalline material is metallic silver (Fig. A1-16). However, the material may contain sediments causing some variation in the XRD spectra and size-analysis (Fig. A1-16).

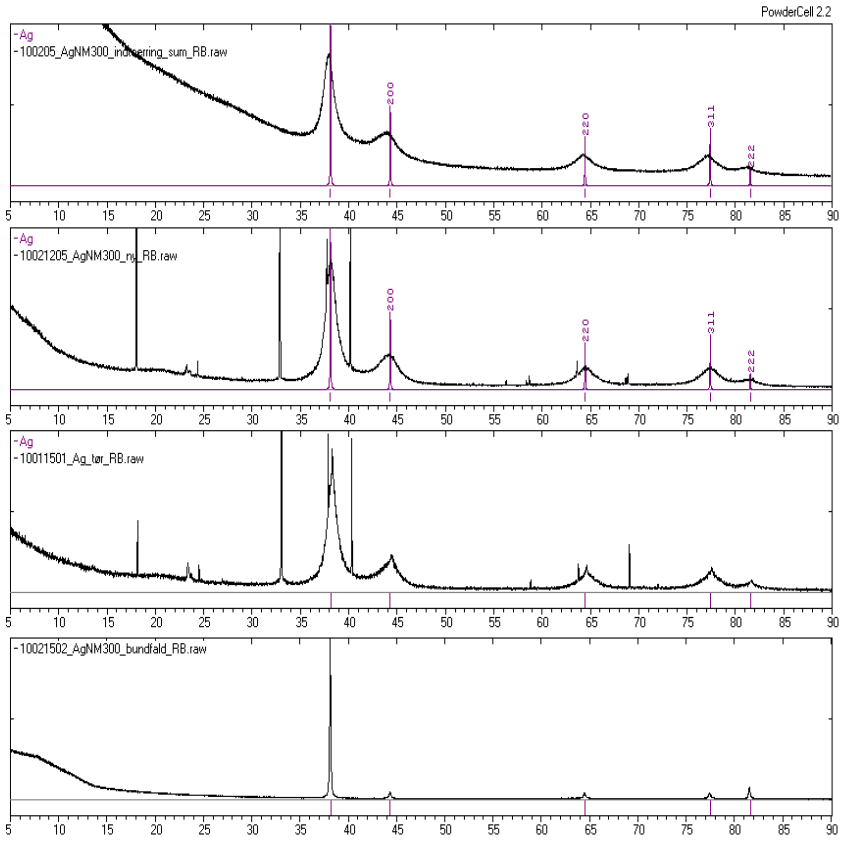

Fig. A1-16 - X-ray powder diffraction data of NM-300 have been measured 4 times. On the top a dataset measured on the liquid of a sample without sediment is shown. Number 2 is the same sample

dried on a glass plate. For these two the expected reflections from pure silver are shown. Below are a sample with sediment and a dataset of the sediment on the bottom.

Particle size and morphology

Data collected by XRD analysis showed quite different results, depending on whether the sample was with or without sediment. Crystallite size was 7±1 for sample without sediment, in liquid; 14±2 for sample without sediment, dried; <6 (89 w%), 15 (9 w%) and > 100 (2 w%) for sample with sediment, dried. The sediment was also measured alone, consisting of large silver crystals. Finally, samples without sediment, in liquid, were used to obtain the crystallite size.
By TEM, the individual particles appear as mainly individual (dispersed) idiomorphic crystallites (Figure A1-17). Some small aggregates do occur. The facets of the crystallites can be observed at high resolution (Figure A1-17d). Minor amounts of aggregates were observed (Figure A1-17b and c). The typical particle size in NM-300, based on the analysis of approx. 1000 particles, was in the 8-47 nm range, with an average value of 17.5 nm. Approx. 99% of particles were in <30 nm.

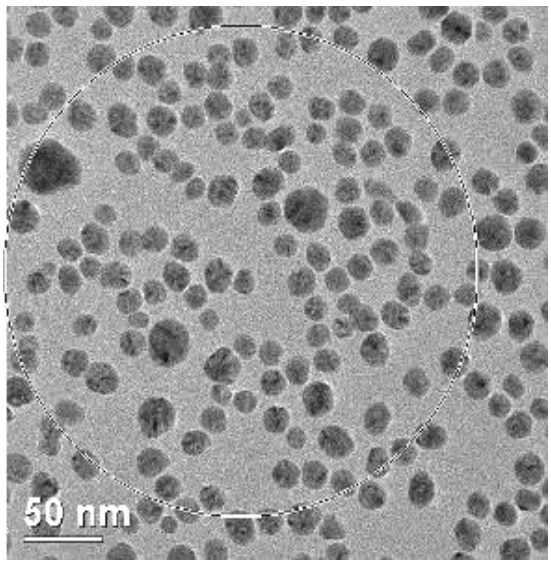

a)

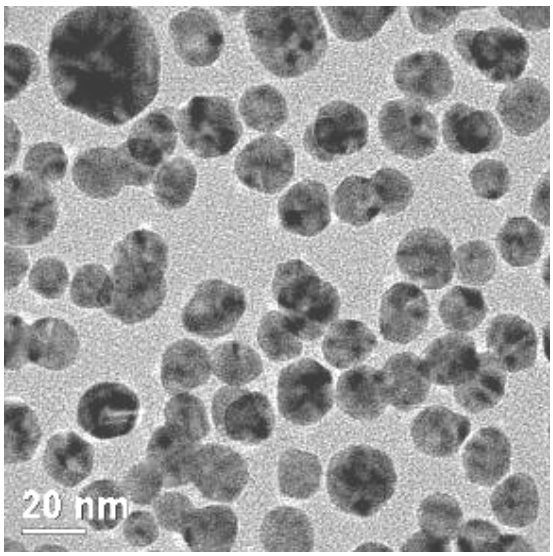

b)

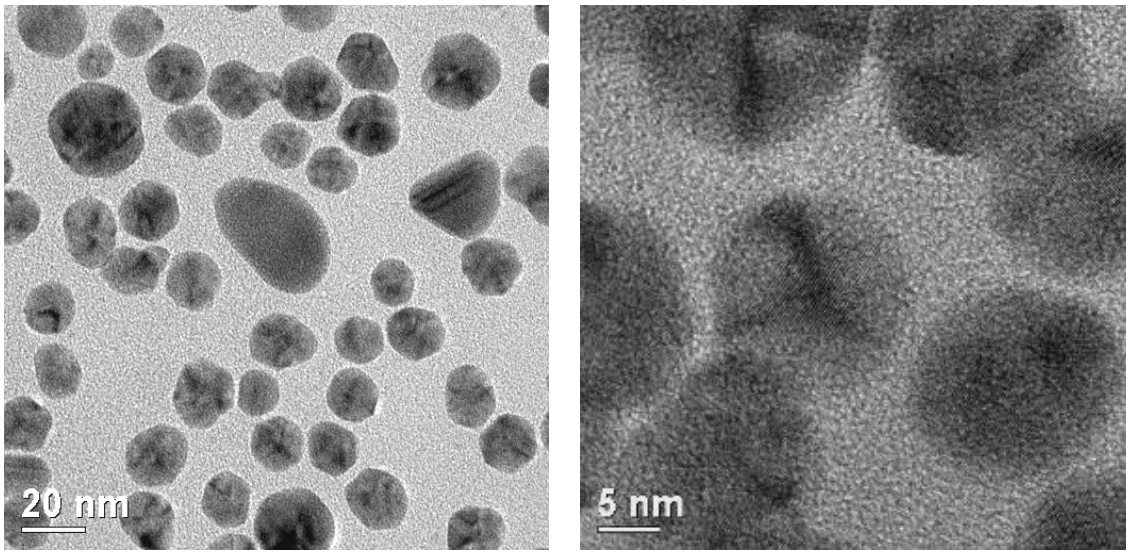

c) d)

Fig. A1-17 – Typical TEM pictures of NM-300 at different magnifications.

BET surface area

BET technique not applicable to liquid dispersions.

Elemental analysis

Very low inorganic trace element impurities were detected by ICP-OES (Table A1-8). No individual impurity particles or crystal structures of the identified elements were moreover identified by TEM-EDX.

Table A1-8 – Trace elements impurities of NM-300.

Element	µg/g	µg/g (LOD)
Fe	28.5±5	0.7
Ca	29±12	8
Zn	20±13	0.6
As	5±1	0.5
Cd	2±0.2	0.1

Ag 47MN-03

NM-Source: Purchased
Producer/Vender: Advanced Materials, Inframat
Content: Silver nanopowder
Coating: None (from supplier)
Appearance: Black, ultrafine powder

Phase composition
The amount of powder was not sufficient

Particle size and morphology

From 150 HR-TEM pictures it was observed that the average size of particle distribution was 61 nm, with a size range between 41 and 81 nm (Fig. A1-18), very similar as declared (i.e. 40-90 nm). For 64% of particles the range is between 35 and 65 nm. Irregular elongated polyhedrons and some spherical particles with rounded and smooth edges were observed (Fig. A1-19a-c).

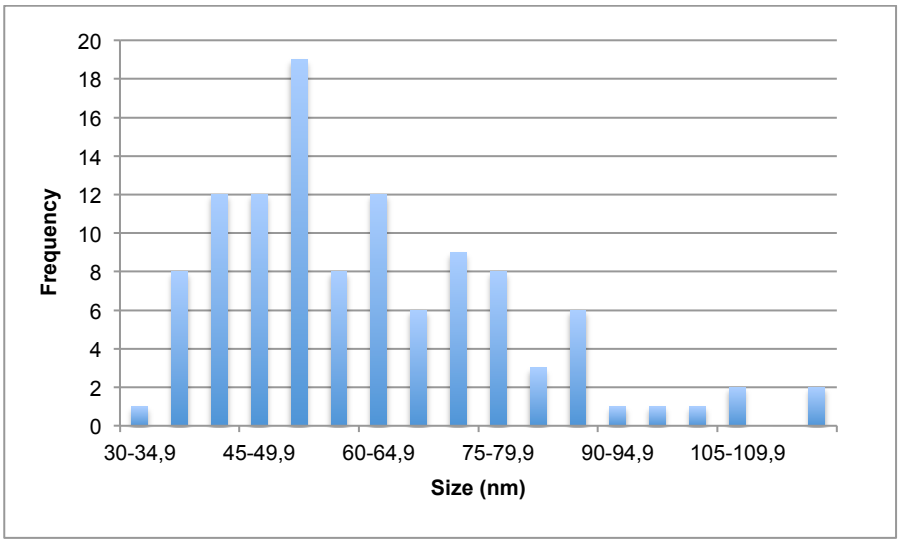

Fig. A1-18 – Ag 47MN-03 size distribution measured by HR-TEM.

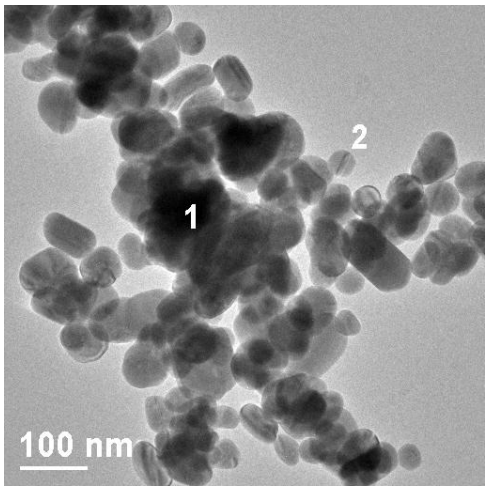

a)

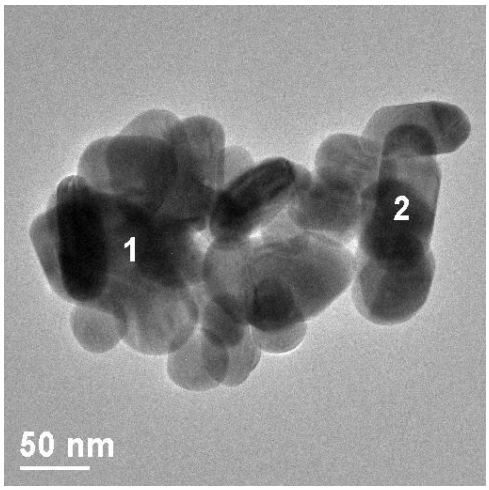

b)

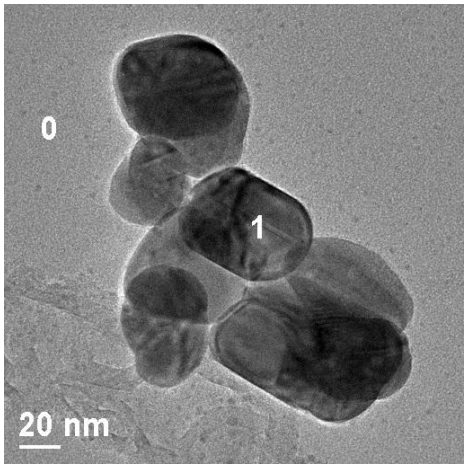

c)

Fig. A1-19 – Typical HR-TEM pictures at different magnifications of Ag 47MN-03.

BET surface area

Specific surface area was 3.8 (±0.1) m^2/g.

Elemental analysis

Very low inorganic trace element impurities were detected by ICP-OES (Table A1-9). No individual impurity particles or crystal structures of the identified elements were identified by TEM-EDX.

Table A1-9 – Trace elements impurities of Ag 47MN-03.

Element	µg/g	µg/g (LOD)
Fe	24±2	0.6
Ca	0.5±0.1	0.03

MWCNT NM-400

NM-Source: JRC, Ispra, Italy
Producer/Vender: NanoCyl
Content: Multiwalled carbon nanotubes (MWCNT)
Coating : CNTs are coated with pyrogenic carbon (data from supplier)
Appearance: Black, carbonaceous powder

Phase composition

No crystalline compounds were detected in the raw sample. However, a crystalline phase, tentatively identified as γ-alumina, was observed after combustion in TGA (Fig. A1-20). Other possibilities are theta alumina (θ-Al_2O_3) or a mixed oxide alumina, e.g. ($Mg_{0.866}Al_{1.8303}O_{3.661}$). Due to only a small volume of sample, the measurement is performed on a silicon sample holder, and preferred orientation is expected. The alumina phase is most likely used as support material for the catalyst used in the production. The sample holder for the TGA is also made of alumina, but they have been used several times and alumina has not been found in the other residual, so this is considered an unlikely source.

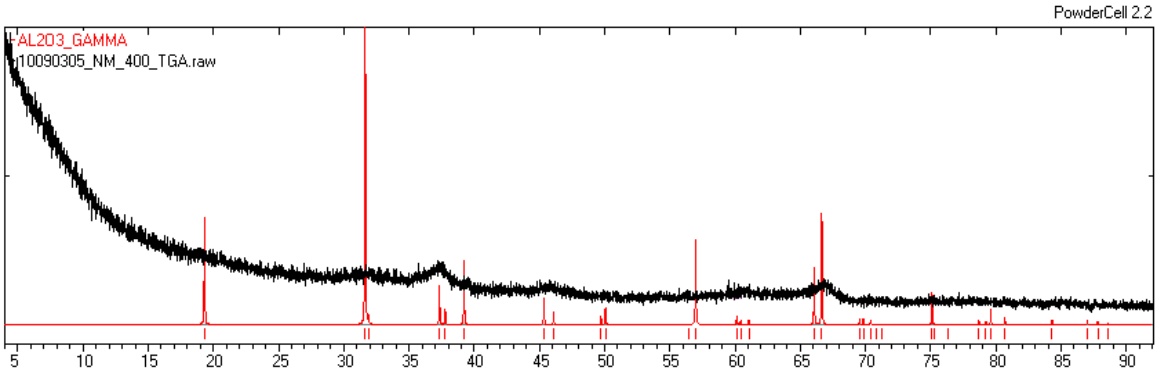

Fig. A1-20 – X-ray powder diffraction data on the residual after TGA on NM-400.

RAMAN spectroscopy shows a high intensity of the D-band (defect band) is relatively high as compared to the G-band (graphite band) (Fig. A1-21). This suggests that the MWCNT in NM-400 has a high concentration of defects. For high quality CNTs the D/G ratio is only a few percent.

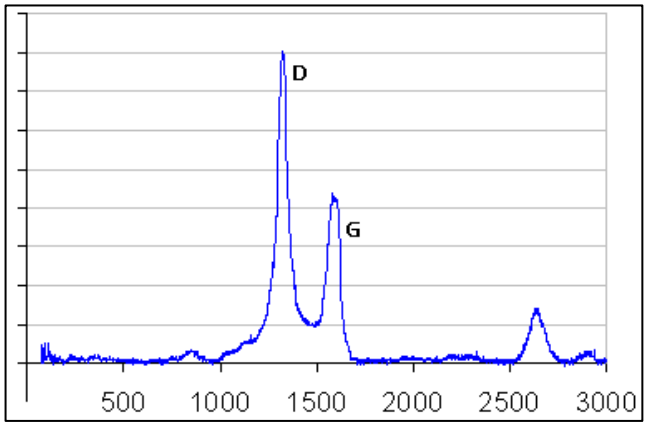

Figure A1-21 - Raman spectroscopy measurement on NM-400.

Particle size and morphology

No information from XRD was available from ENPRA project partners. SEM investigation showed open agglomerates of entangled CNT. The individual CNT were often kinked and bend. Some individual CNT were also detected. Approx 80% of CNT were 0.7 to 3 μm in length (Figs. A1-22a-b). By TEM, the individual CNT were observed as inhomogeneous, kinked and mostly bent multiwalled (10-20 walls) (Figs. A1-22c-f). Some cone-stacked MWCNT were also observed. Defects were typically found ay bends and kinks. Some tubes were closed at the end and some even had multiple caps due to overgrowth. Some Fe/Co (by TEM-EDX) NP (6-9 nm, average 7.5 nm) were found inside the tubes. The typical diameter was 5-35 nm (~80%: 10-15 nm) and the between 0.7 and 3 μm (80%).

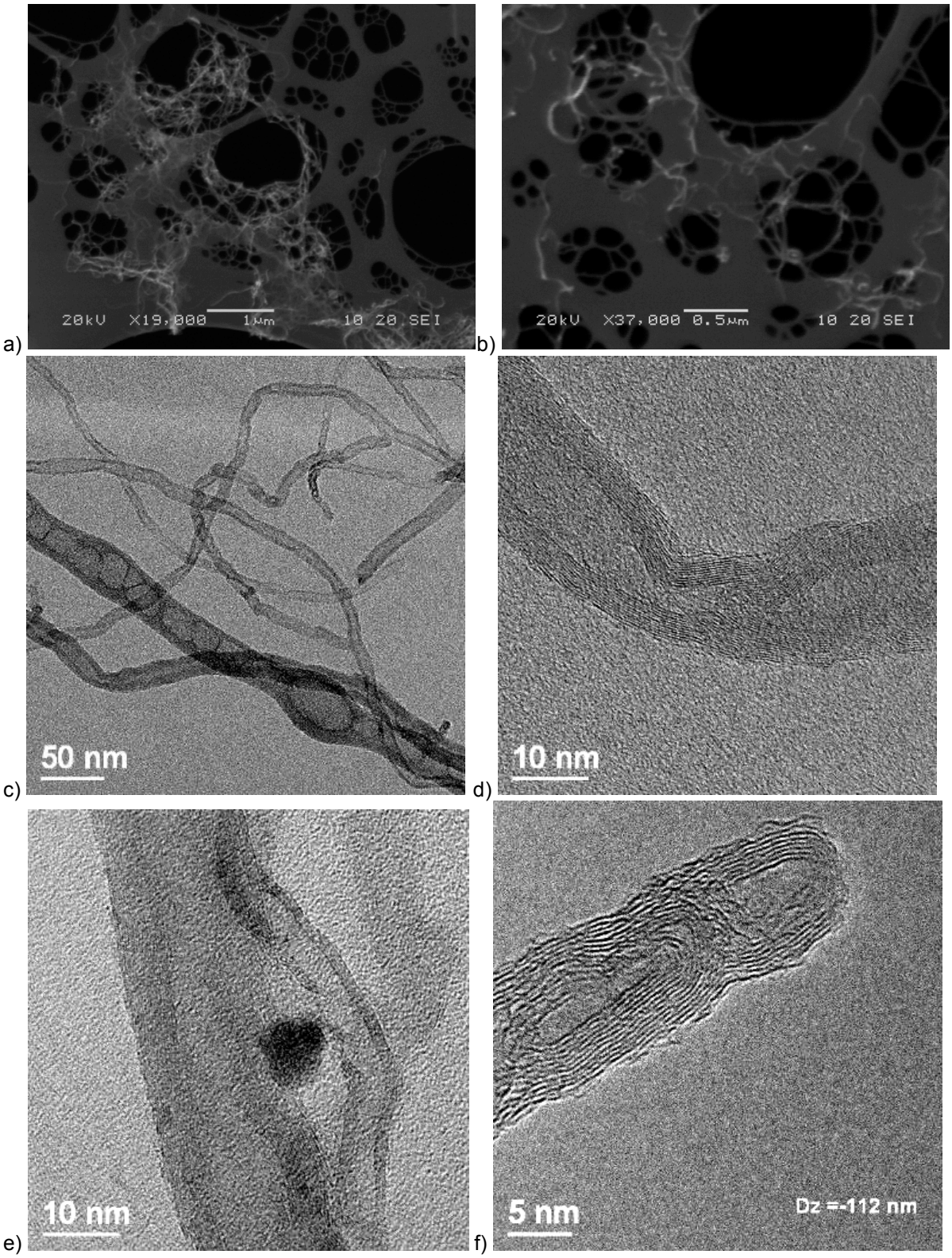

Fig. A1-22 - Electron microscopy images of NM-400. a) SEM-image showing an entangled CNT in an open agglomerate. b) SEM-image showing another entangled MWCNT agglomerate and single free tubes. c) TEM-image showing an overview of the bend and inhomogeneous structure of the individual CNT. d) High-resolution image showing kinked CNT with intergrowth (cone-like structure). e) TEM-

image showing a thin and thicker MWCNT associated with catalyst material (dark spherical particle). f) TEM-image showing overgrowth structures at the end of a closed-end tube.

BET surface area and pore volume

Specific surface area was 298 (±1) m^2/g and specific pore volume was 1.4 ml/g.

Elemental analysis

By TEM-EDX it was identified presence of Fe and Co as constituents of nano-sized catalysts. Very high concentrations of residual metal catalysts were detected both by ICP-OES and ICP-MS (Table A1-10).

Table A1-10 – Trace elements impurities detected in NM-400.

Element	µg/g (ICP-OES)	µg/g (ICP-MS)	µg/g (LOD ICP-OES)	µg/g (LOD ICP-MS)
Al	49363±653	42477±700	0.9	0.05
Fe	3568±126	1852±87	0.6	0.02
Co	2084±58	2178±101	0.1	0.01
Na	-	410±26	-	0.03

MWCNT NM-402

NM-Source: JRC, Ispra, Italy
Producer/Vender: Arkema
Content: Multiwalled carbon nanotubes (MWCNT)
Coating : none (from supplier)
Appearance: Black, carbonaceous powder

Phase composition

NM-402 did not exhibit any crystalline structures in XRD analysis of the raw sample. The residual after TGA measurement was measured by XRD (Fig. A1-23). The material is mainly Hematite, Fe_2O_3. There are indications of an extra phase, but this is only present in a small amount and the crystals are small (equal wide reflections) and the phase has therefore not been identified.

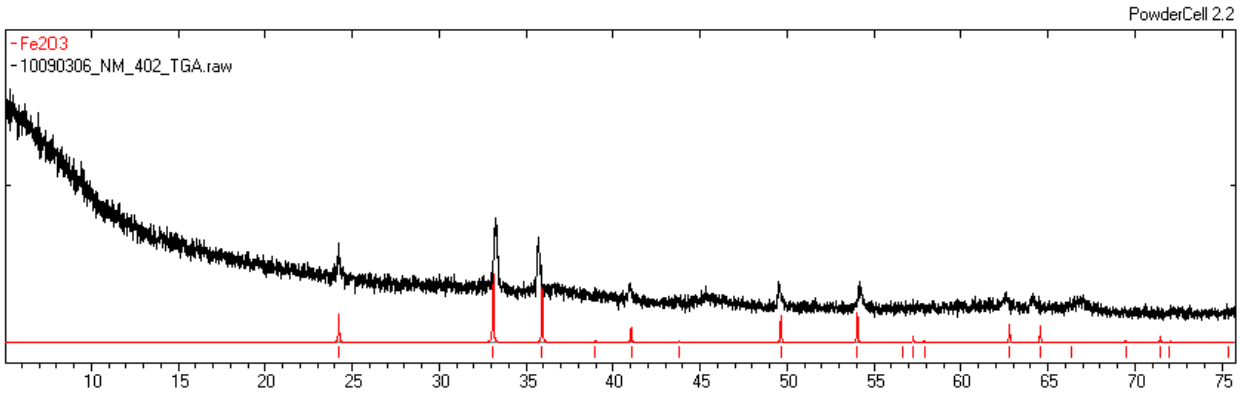

Fig. A1-23 - X-ray powder diffraction data on the residual after TGA on NM-402.

RAMAN spectroscopy showed a high intensity of the D-band (defect band), relatively high as compared to the G-band (graphite band) (Fig. A1-24). This suggests that NM-402 has a high concentration of defects. For high quality CNT the D/G ratio is only a few percent. The small peaks around 250 nm (marked as RMB) might indicate presence of SWCNT as well, but as the current data are not of sufficient quality to make certain identification.

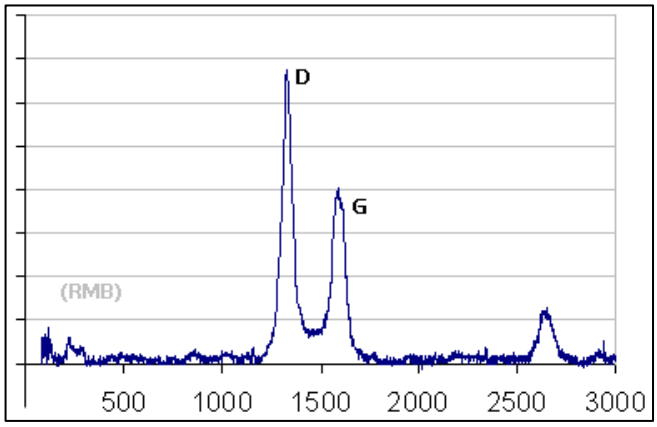

Fig. A1-24 - Raman spectroscopy measurement on NM-402.

Particle size and morphology

No information from XRD was available from ENPRA project partners. SEM investigation showed presence of agglomerates of bend and strongly entangled carbon nanotubes. Some individual tubes were also detected. For approx. 80% of CNT the length was in the range of 0.7-4.5 µm (Fig. A1-25).

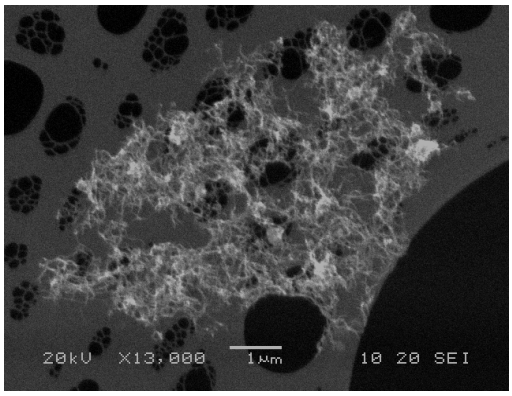

a)

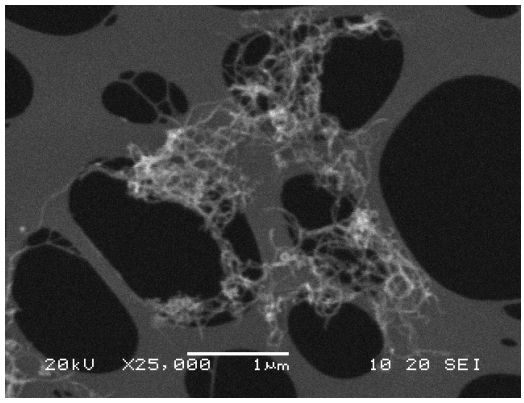

b)

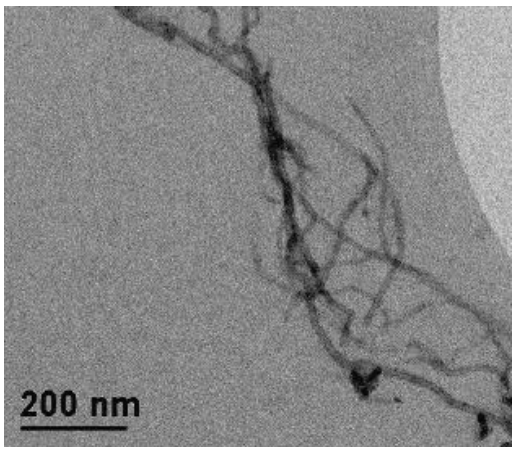

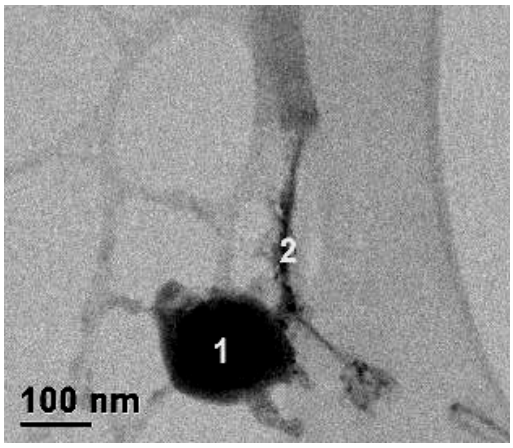

c) d)

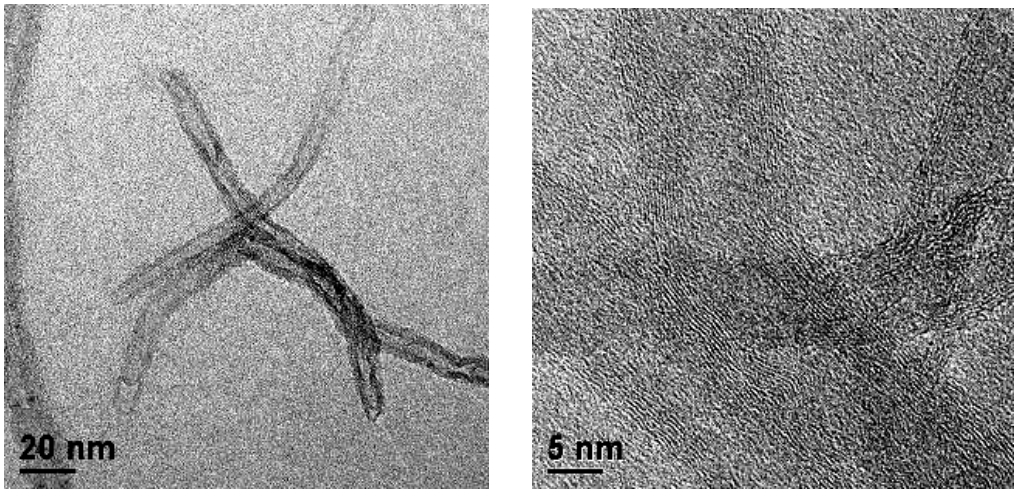

e) f)

Fig. A1-25 - Typical EM images of NM-402. a) SEM-image showing a large open agglomerate of relatively long entangled MWCNT. b) SEM-image showing a smaller open agglomerates of entangled MWCNT c). TEM-image showing entangled MWCNT and presence of minor catalyst material (dark spots). d) TEM-image of a large (1) and small (2) Fe-rich catalyst particles. e). TEM-image showing short MWCNT. f). High-resolution TEM-image illustrating MWCNTS with irregular defect rich CNT-walls.

By TEM, CNT appear irregular, mostly bent and partially entangled (Figs. A1-25c-f). The number of CNT walls is on the order of 6-14. In agreement with RAMAN data, CNT contained many defects, and often where bending takes place (Figs. A1-25e-f). Some tubes were capped by unknown material. Some nano-onions (5-10 nm) and amorphous carbon structures, mixed with Fe (5-20 nm) catalyst nanoparticles were also observed. However, individual catalyst particles were up to at least 150 nm in size (particle 1 in Fig. A1-25d). The typical CNT diameters are 5-21 nm and the length distribution is 0.7-4.5 μm (80% of CNT).

BET surface area and porosity

Specific surface area was 225 (±1) m^2/g and specific pore volume was 1.2 ml/g.

Elemental analysis

TEM-EDX identified presence of Fe and Co as constituents in nano-sized catalysts. Very high concentrations of residual metal catalysts were detected both by ICP-OES and ICP-MS (Table A1-11).

Table A1-11 – Trace elements impurities detected in NM-402.

Element	µg/g (ICP-OES)	µg/g (ICP-MS)	µg/g (LOD ICP-OES)	µg/g (LOD ICP-MS)
Al	32190±7135	24555±321	0.9	0.05
Fe	17136±1111	8346±102	0.6	0.02
Co	17.6±0.8	2.4±0.1	0.1	0.01
Na	-	580±51	-	0.03

ANNEX 2

Sedimentation profiles and actual exposure concentrations of the n-TiO_2 P25 in aqueous dispersions

The sedimentation profiles of the n-TiO_2 tested aqueous dispersions under environmentally realistic n-TiO_2 initial concentrations (0.01, 0.1, 1 and 10 mg/l) are displayed below.

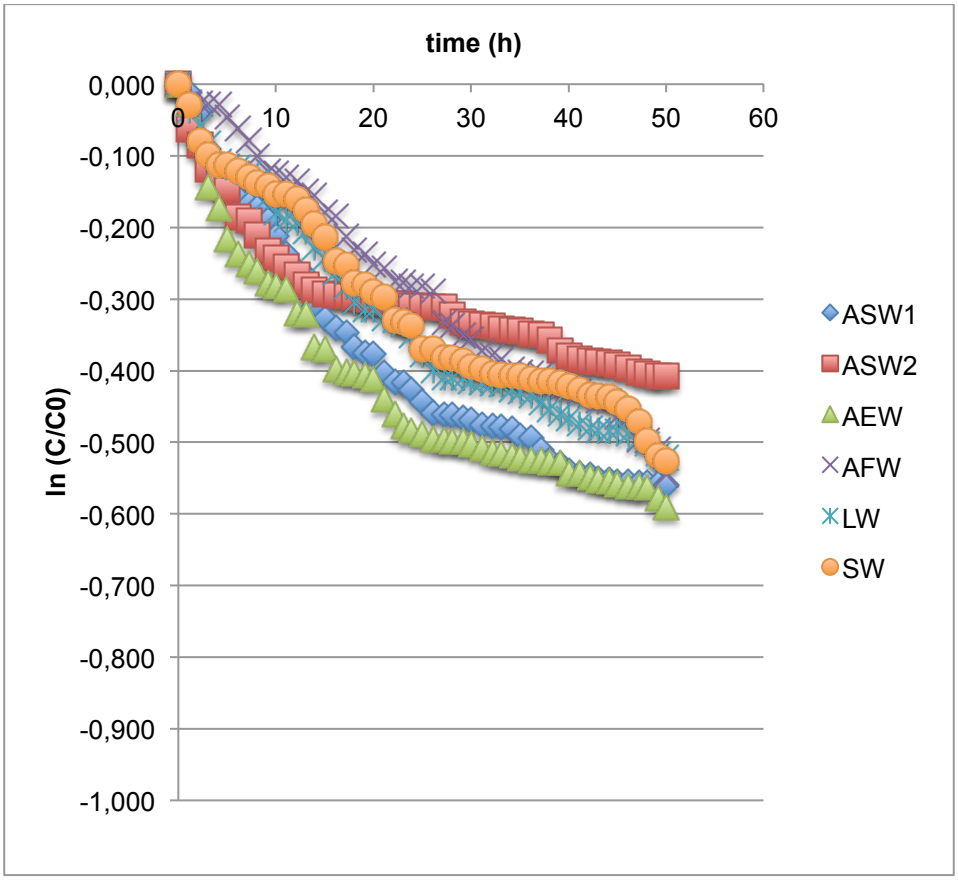

Fig. A2-1 - Sedimentation profiles of 0.01 mg/l n-TiO_2 P25 dispersions.

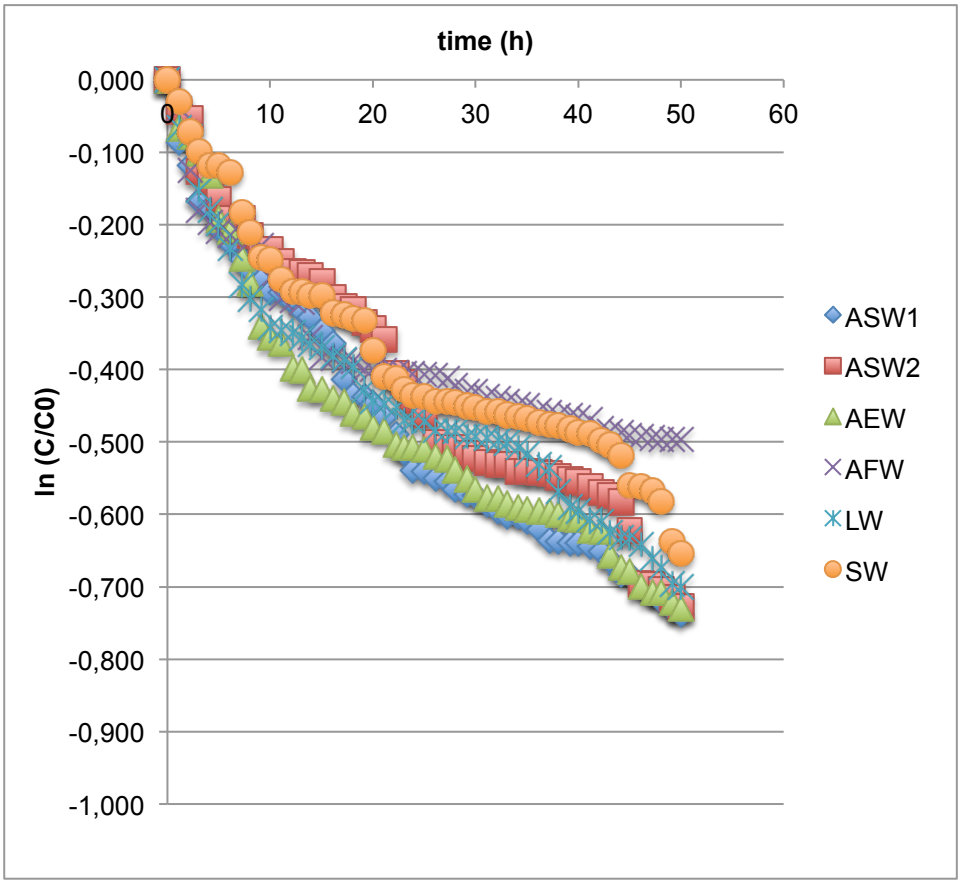

Fig. A2-2 - Sedimentation profiles of 0.1 mg/L n-TiO_2 P25 dispersions.

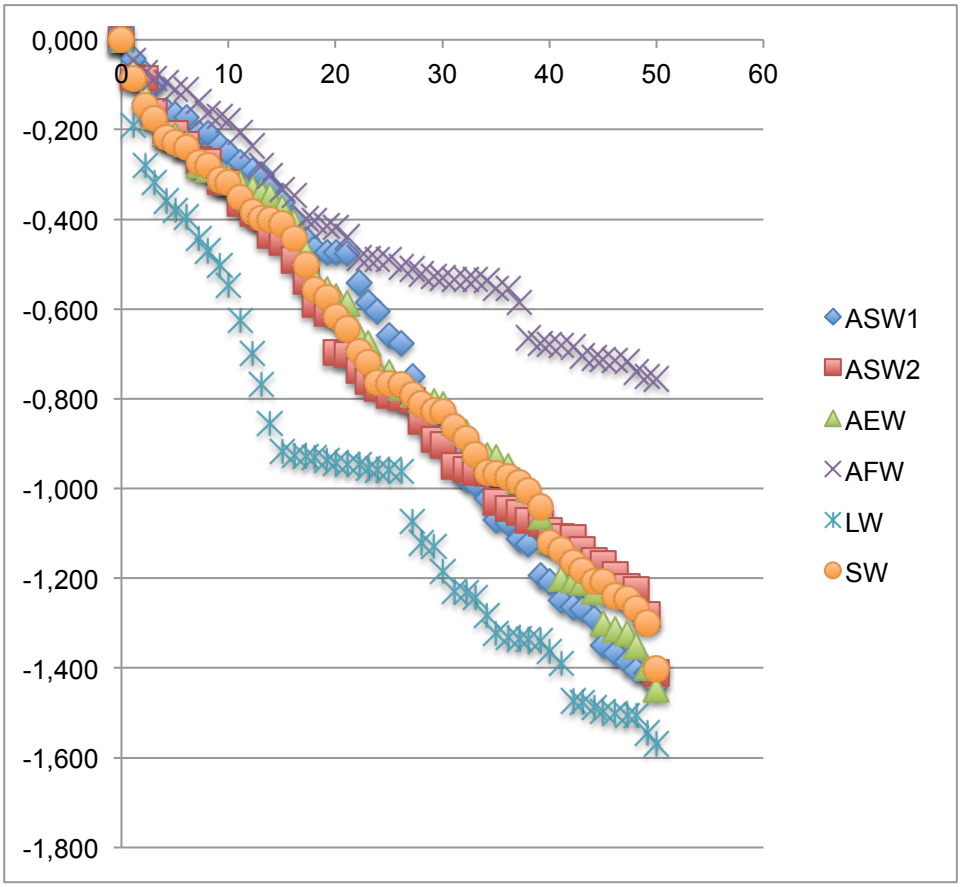

Fig. A2-3 - Sedimentation profiles of 1 mg/L n-TiO_2 dispersions.

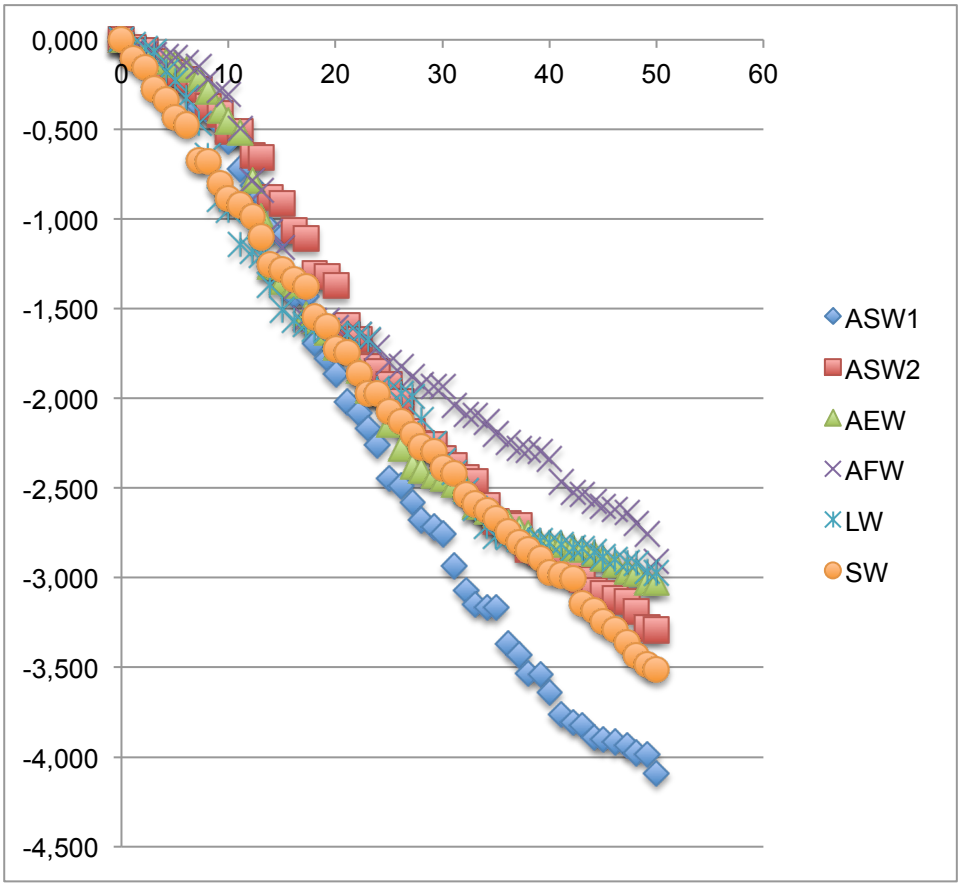

Fig. A2-4 - Sedimentation profiles of 10 mg/L n-TiO_2 dispersions.

Table A2-1 - Actual dispersed n-TiO_2 P25 concentrations (mg/l) at 1, 5, 10, 15, 25 and 50 h from the start of the experiments (AFW: artificial freshwater; AEW: artificial estuarine water; ASW1: artificial seawater 1; ASW2: artificial seawater 2).

	n-TiO_2 P25 - 0.01 mg/l					
	1 h	**5 h**	**10 h**	**15 h**	**25 h**	**50 h**
AFW	$9.7 \cdot 10^{-3}$	$9.5 \cdot 10^{-3}$	$8.8 \cdot 10^{-3}$	$8.4 \cdot 10^{-3}$	$7.5 \cdot 10^{-3}$	$5.8 \cdot 10^{-3}$
AEW	$9.7 \cdot 10^{-3}$	$8.1 \cdot 10^{-3}$	$7.5 \cdot 10^{-3}$	$6.9 \cdot 10^{-3}$	$6.1 \cdot 10^{-3}$	$5.5 \cdot 10^{-3}$
ASW1	$9.9 \cdot 10^{-3}$	$8.6 \cdot 10^{-3}$	$8.1 \cdot 10^{-3}$	$7.2 \cdot 10^{-3}$	$6.4 \cdot 10^{-3}$	$5.7 \cdot 10^{-3}$
ASW2	$9.4 \cdot 10^{-3}$	$8.6 \cdot 10^{-3}$	$7.8 \cdot 10^{-3}$	$7.5 \cdot 10^{-3}$	$7.3 \cdot 10^{-3}$	$6.6 \cdot 10^{-3}$
LW	$9.6 \cdot 10^{-3}$	$8.9 \cdot 10^{-3}$	$8.3 \cdot 10^{-3}$	$7.8 \cdot 10^{-3}$	$6.8 \cdot 10^{-3}$	$5.9 \cdot 10^{-3}$
SW	$9.7 \cdot 10^{-3}$	$8.9 \cdot 10^{-3}$	$8.6 \cdot 10^{-3}$	$8.1 \cdot 10^{-3}$	$6.9 \cdot 10^{-3}$	$5.9 \cdot 10^{-3}$
	n-TiO_2 P25 - 0.1 mg/l					
	1 h	**5 h**	**10 h**	**15 h**	**25 h**	**50 h**
AFW	$9.6 \cdot 10^{-2}$	$8.1 \cdot 10^{-2}$	$7.6 \cdot 10^{-2}$	$6.8 \cdot 10^{-2}$	$6.7 \cdot 10^{-2}$	$6.1 \cdot 10^{-2}$
AEW	$9.4 \cdot 10^{-2}$	$8.3 \cdot 10^{-2}$	$7 \cdot 10^{-2}$	$6.5 \cdot 10^{-2}$	$6 \cdot 10^{-2}$	$4.8 \cdot 10^{-2}$
ASW1	$9.2 \cdot 10^{-2}$	$8.1 \cdot 10^{-2}$	$7.5 \cdot 10^{-2}$	$7.1 \cdot 10^{-2}$	$5.8 \cdot 10^{-2}$	$4.8 \cdot 10^{-2}$
ASW2	$9.6 \cdot 10^{-2}$	$8.5 \cdot 10^{-2}$	$7.9 \cdot 10^{-2}$	$7.6 \cdot 10^{-2}$	$6.3 \cdot 10^{-2}$	$4.8 \cdot 10^{-2}$
LW	$9.4 \cdot 10^{-2}$	$8.2 \cdot 10^{-2}$	$7.1 \cdot 10^{-2}$	$6.9 \cdot 10^{-2}$	$6.2 \cdot 10^{-2}$	$5 \cdot 10^{-2}$
SW	$9.7 \cdot 10^{-2}$	$8.9 \cdot 10^{-2}$	$7.8 \cdot 10^{-2}$	$7.4 \cdot 10^{-2}$	$6.5 \cdot 10^{-2}$	$5.2 \cdot 10^{-2}$
	n-TiO_2 P25 - 1 mg/l					
	1 h	**5 h**	**10 h**	**15 h**	**25 h**	**50 h**
AFW	$9.5 \cdot 10^{-1}$	$8.9 \cdot 10^{-1}$	$8.4 \cdot 10^{-1}$	$7.2 \cdot 10^{-1}$	$6.1 \cdot 10^{-1}$	$4.7 \cdot 10^{-1}$
AEW	$9.4 \cdot 10^{-1}$	$8.1 \cdot 10^{-1}$	$7.4 \cdot 10^{-1}$	$6.9 \cdot 10^{-1}$	$4.8 \cdot 10^{-1}$	$2.3 \cdot 10^{-1}$
ASW1	$9.6 \cdot 10^{-1}$	$8.5 \cdot 10^{-1}$	$7.8 \cdot 10^{-1}$	$7 \cdot 10^{-1}$	$5.2 \cdot 10^{-1}$	$2.4 \cdot 10^{-1}$
ASW2	$9.2 \cdot 10^{-1}$	$8.1 \cdot 10^{-1}$	$7.3 \cdot 10^{-1}$	$6.4 \cdot 10^{-1}$	$4.5 \cdot 10^{-1}$	$2.4 \cdot 10^{-1}$
LW	$8.3 \cdot 10^{-1}$	$6.8 \cdot 10^{-1}$	$5.8 \cdot 10^{-1}$	$4 \cdot 10^{-1}$	$3.8 \cdot 10^{-1}$	$2.1 \cdot 10^{-1}$
SW	$9.2 \cdot 10^{-1}$	$7.9 \cdot 10^{-1}$	$7.3 \cdot 10^{-1}$	$6.6 \cdot 10^{-1}$	$4.6 \cdot 10^{-1}$	$2.5 \cdot 10^{-1}$
	n-TiO_2 P25 - 10 mg/l					
	1 h	**5 h**	**10 h**	**15 h**	**25 h**	**50 h**
AFW	9.4	9.1	7.4	3.1	1.7	0.5
AEW	9.6	8.7	6.4	2.6	1.2	0.5
ASW1	9.7	8.4	5.7	3.3	0.9	0.2
ASW2	9.6	8.3	6	4	1.5	0.4
LW	9.7	7.9	3.9	2.2	1.4	0.5
SW	9	6.5	4.1	2.8	1.3	0.3